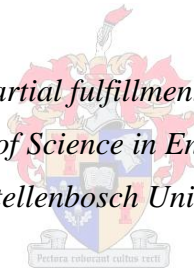


Experimental and numerical evaluation of anisotropic fill performance characteristics in cross- and counterflow

By

Pieter Jacobus Grobbelaar

*Thesis presented in partial fulfillment of the requirements for
the degree of Master of Science in Engineering (Mechanical)
at Stellenbosch University*



Department of Mechanical and Mechatronic Engineering,
Stellenbosch University,
Private Bag X1, Matieland 7602, South Africa.

Supervisor: Prof. Hanno C. R. Reuter

March 2012

DECLARATION

By submitting this thesis/dissertation electronically, I declare that the entirety of the work contained therein is my own, original work, and that I have not previously in its entirety or in part submitted it for obtaining any qualification.

.....

Signature of candidate

.....day of

Copyright © 2012 Stellenbosch University

All rights reserved

ABSTRACT

The confidence level of modeling cooling towers, where oblique air flow within anisotropic fills takes place, is higher when the change in fill's performance characteristics, dependent on the way that air flows through the fill, is better understood.

A trickle fill's performance characteristics in crossflow are compared to its performance characteristics in counterflow by doing crossflow fill tests that are performance comparable to counterflow tests with the same fill. In order to do these tests, an existing crossflow fill test facility is critically evaluated and improved.

The difference between crossflow and counterflow trickle fill performance characteristics is found to depend on air mass velocity (G_a) and water mass velocity (G_w) and to be between 0 and 35% for the Merkel number (Me) and up to almost 200% for the loss coefficient.

Additionally, the validity of a recently developed 2-dimensional evaporative cooling model is investigated by comparing its predictions to experimental results. The following conclusions are made:

- For trickle fill and rain zone tests, the model, with the present assumptions, predicts the average temperature of the outlet air to within approximately 0.4 °C.
- Currently, temperature profiles that are experimentally measured at the air and water outlets are subject to significant edge effects, which prevent a fair comparison to model predictions.
- The model predictions can be improved if local variations in Me and the redistribution of water by the fill are taken into account.

Keywords: Crossflow, counterflow, performance characteristics, anisotropic, fill, wet-cooling tower

OPSOMMING

Die betroubaarheid van die modellering van koeltorings, waar lug skuins deur anisotropiese pakking (of “fill” in Engels) vloei, is hoër indien die verandering in die pakking se verrigtingseienskappe, wat afhang van die manier waarop die lug deur die pakking vloei, beter verstaan word.

’n Drup pakking (of “trickle fill” in Engels) se verrigtingseienskappe in kruisvloei word vergelyk met dié in teenvloei deur kruisvloei pakking toetse, wat direk vergelykbaar is met teenvloei toetse vir dieselfde pakking, te doen. Ten einde hierdie toetse te doen, word ’n bestaande kruisvloei toets fasiliteit krities ondersoek en verbeter.

Dit word bevind dat die verskil tussen die drup pakking se kruisvloei en teenvloei verrigtingseienskappe afhang van lug massa snelheid (G_a) en water massa snelheid (G_w) en 0 tot 35% is vir die Merkel getal (Me) en so groot as 200% is vir die verlies koëffisiënt.

Verder word die geldigheid van ’n 2-dimensionele nat-verkoelingsmodel wat onlangs ontwikkel is ondersoek deur die model se voorspellings te vergelyk met eksperimentele resultate. Die volgende gevolgtrekkings word gemaak:

- Die model, met huidige aannames, voorspel die gemiddelde uitlaat lug temperatuur met ’n afwyking van ongeveer 0.4°C .
- Die temperatuur profiele wat eksperimenteel gemeet word by die lug en water uitlate is onderworpe aan noemenswaardige rand effekte, wat ’n behoorlike vergelyk met model voorspellings verhoed.
- Die model se voorspelling van die profiele kan verbeter word indien die lokale variasies in Me en die herverdeling van die water deur die pakking in ag geneem kan word.

Trefwoorde: Kruisvloei, teenvloei, anisotropies, pakking, nat-koel toring, verrigtingseienskappe

Met baie liefde en diep waardering
opgedra aan my ouers, Deon en Ina

ACKNOWLEDGEMENTS

Prof Hanno Reuter, thank you for your excellent and dedicated guidance and for treating me with so much more kindness and patience than I deserved. You have helped me to become a better engineer and to grow as a person.

IWC, GEA and Eskom for their financial and material support of this project.

Pa en Ma, ek is so geseënd om julle te hê. Baie dankie ook vir al die kere wat Pa my help dink het oor hierdie projek.

Yngvi Guðmundsson, takk fyrir að deila þekkingu þinni með mér og fyrir öll skiptin sem þú hjálpaðir mér. Það var mér meira virði en þú kannski gerir þér grein fyrir. Takk fyrir allan stuðninginn og öll skiptin sem við gátum hlegið saman.

Stiaan Gerber, baie dankie vir al die hulp met die Python en FORTRAN.

Thank you to all the technical staff in the Departement of Mechanical Engineering: Juliun, vir jou bystand en ondersteuning met die eksperimentele werk, om saam met jou te werk was een van die hoogtepunte van hierdie 3 jaar. Ferdi and Calvin, dankie vir julle hulp om my eksperimentele toerusting te ontwerp en te maak. Maurisha en Shiyaam, dankie vir julle hulpvaardigheid in die stoor en dat julle my altyd laat glimlag het. Oom Cobus, Nathi and Lonwabo for the times when you helped me with this project.

Dankie ook aan my kollegas en vriende Bosman en Hermanus vir julle hulp met die eksperimentele werk en dat julle die kantoor 'n lekker plek gemaak het om te wees.

Ek dank my hemelse Vader vir hoe goed Hy is en vir sy eindelose genade en dat Hy stukkende mense red en nuut maak.

TABLE OF CONTENTS

LIST OF TABLES	x
LIST OF FIGURES	xii
NOMENCLATURE	xvii
1. INTRODUCTION	1
1.1. Overview of wet-cooling tower technology	1
1.1.1. Wet-cooling towers in thermal power cycles	1
1.1.2. Operation principle	2
1.1.3. The fill zone, fill performance characteristics and different fill types	3
1.1.4. Forms of relative flow in cooling towers	4
1.1.5. Anisotropic fill performance characteristics	5
1.2. Performance prediction of cooling towers	5
1.2.1. Simplified methods of modeling cooling towers	6
1.2.2. The use of CFD to model cooling towers	6
1.3. Experimental work preceding this project	7
1.4. Objectives	7
1.5. Motivation	8
1.6. Thesis outline	9
2. METHODS USED TO MODEL WET-COOLING	12
2.1. Fill models currently used in industry and their shortcomings	12
2.2. The Reuter 2-dimensional evaporative cooling model	12
2.2.1. Assumptions made in the Reuter model	13
2.2.2. Governing differential equations	13
2.2.3. Discretization of the governing differential equations	14
2.2.4. The second order upwind differencing scheme	16
2.2.5. Iterative solution of a cell	17
2.2.6. Iterative solution of the computational domain	18
2.2.7. Methods to increase the solution speed of the model in a computer program	21
2.2.8. Example case and output of the present fill simulation program	21
2.2.9. Grid dependence and other dependencies	23
2.2.10. Verification of present fill simulation program results	25
2.3. Model of a single drop free falling through an oblique air stream	26
2.3.1. Governing equations for drop motion	27
2.3.2. Drag and lift coefficients for a drop	28
2.3.3. Mass change of the drop	29
2.3.4. Calculation of the temperature change of the drop	30
2.3.5. Implementation of model into a single drop simulation program	31

2.3.6.	Drop Merkel number	31
2.3.7.	Validation of single drop simulation program results	32
2.4.	Comparison between model predictions made by the Reuter model and the single drop model.....	32
3.	EXPERIMENTAL APPARATUS AND METHODOLOGY	34
3.1.	Overview of test facilities and experimental procedures.....	34
3.1.1.	Crossflow test facility.....	34
3.1.2.	Counterflow test facility	37
3.2.	Measurement techniques and instrumentation	37
3.2.1.	General temperature measurement.....	37
3.2.2.	Dry- and wetbulb temperature measurement with aspirated psychrometers.....	37
3.2.3.	Temperature profile measurement with rakes	38
3.2.4.	Mass flow rate measurement.....	40
3.2.5.	Pressure measurement	41
3.3.	Drop size distribution in the crossflow test facility	41
3.4.	Data acquisition	42
3.4.1.	Data acquisition system.....	42
3.4.2.	Measurement correction during data acquisition	43
3.4.3.	Recording and saving of data	43
3.5.	Data processing.....	44
3.5.1.	Statistical analysis of the raw data	44
3.5.2.	Processing of recorded data.....	47
3.6.	Critical evaluation of crossflow test facility	49
3.6.1.	Miscellaneous improvements	49
3.6.2.	Accuracy of relative temperature measurements	50
3.6.3.	Uniformity of water distribution	51
3.6.4.	Mass flow rate measurements	53
3.6.5.	Uncertainty in the calculated Me/L_{fi} , K_{fdm}/L_{fi} and EB	54
3.7.	Experimental tests done.....	56
4.	COMPARISON OF CROSSFLOW AND COUNTERFLOW FILL PERFORMANCE	57
4.1.	Definition of tested fill configurations	57
4.2.	Scope of experimental data.....	57
4.3.	Determined fill characteristics.....	59
4.4.	Discussion of results.....	64
5.	COMPARISON BETWEEN EXPERIMENTAL RESULTS AND THE MODEL PREDICTIONS	66
5.1.	Discussion of differences between model and experimental results for rain zone tests.....	67

5.2. Using the Reuter model with a non-uniform Me/L_{fi}	68
5.3. Discussion of differences between model and experimental results for trickle fill tests.....	69
5.4. A first approximation of the water mass velocity distribution within the fill in the crossflow test facility	71
5.5. Summary.....	73
6. CONCLUSIONS AND RECOMMENDATIONS	75
6.1. Project outcomes.....	75
6.2. Conclusion about the difference between crossflow and counterflow fill performance characteristics of a trickle fill	77
6.3. Conclusion about validity of the Reuter model	78
6.4. Other contributions made during this project	78
6.5. Recommendations for ongoing research	79
6.5.1. Investigate the linearity of fill performance characteristics of anisotropic fill as a function of the relative angle between the air and the water	79
6.5.2. Refine the implementation of the Reuter model	80
6.5.3. More fill tests.....	80
6.5.4. Investigate the testing of splash fill in the counterflow test section.....	80
6.5.5. Further improvement of crossflow test facility	81
6.5.6. Investigate the water redistribution by a trickle fill in the crossflow test section.....	81
6.5.7. Measure splashing drop sizes during a crossflow rain zone test	81
7. REFERENCES.....	82
APPENDIX A: Sample calculations.....	85
A.1. Notes	85
A.2. Movement, mass- and heat transfer from a single drop falling through an oblique air stream	85
A.3. Calculation of m_{avo} from nozzle flow meters	91
A.4. Calculation of EB , K_{fdm}/L_{fi} and Me/L_{fi} from crossflow test data.....	93
APPENDIX B: Crossflow test results in table form.....	99
B.1. Notes.....	99
B.2. Important note regarding test results	100
B.3. Trickle fill in straight crossflow configuration.....	101
B.4. Trickle fill in crossflow (counterflow config).....	104
B.5. Rain zone tests	108
B.6. Trickle fill in crossflow, $L_{fi,x} = 1.5$ m (Figure B.2)	110

APPENDIX C: Detailed information about thermocouples in the crossflow test facility	112
C.1. Thermocouple locations	112
C.1.1. Aspirated psychrometers at air inlet	112
C.1.2. Aspirated psychrometers downwind of the air mixing vanes	112
C.1.3. Rake of aspirated psychrometers immediately downwind of test section	113
C.1.4. Various thermocouples that measure water temperature at the outlet	113
C.1.5. Other sensors	114
C.2. Thermocouple channel numbers and correction factors	114
APPENDIX D: Report on improvements made to the crossflow test facility	116
D.1. Improved equipment to measure the temperature of the water at the outlet	116
D.2. Work done to improve the uniformity of water distribution	117
D.3. Installation of 4 additional psychrometers into rake at air outlet	118
D.4. Installation of 8 additional thermocouples downwind of mixing vanes	119
D.5. Installation of a higher capacity drain pump	120
D.6. Other work and improvements	120
APPENDIX E: Content of DVD submitted with thesis	121
E.1. Code and demos of how to use it	121
E.2. Additional test data and graphical displays	122

LIST OF TABLES

Table 2.1: Four ways in which the present fill simulation program may be run	20
Table 2.2: Setting used for example case in the present fill simulation program	22
Table 2.3: Comparison between grid dependence for crossflow using the forward or backward sequence	24
Table 2.4: Comparison between results from present fill simulation program and Gudmundsson's (2012) program	25
Table 2.5: Comparison between results from the present fill simulation program and from Reuter (2010)	26
Table 2.6: Comparison of single drop model results to results from Reuter (2010)	32
Table 3.1: Sample raw data set: measurements from the four thermocouples that T_{ai} during a crossflow test	44

Table 3.2: Deviation data for example case	45
Table 3.3: Summary of statistical analysis on sample raw data set, Part 1	46
Table 3.4: Summary of statistical analysis on sample raw data set, Part 2	46
Table 3.5: Condensed statistical results for the example T_{ai} sensor set.....	46
Table 3.6: Amounts of sensors used to measured various properties during a crossflow test	48
Table 3.7: Summarized results from final water distribution tests.....	53
Table 3.8: Estimated measurement uncertainty in crossflow test facility and sensitivity gradients of derived Me/L_{fi} , K_{fdm}/L_{fi} and EB	55
Table 3.9: Pessimistic estimated accuracy of Me/L_{fi} , K_{fdm}/L_{fi} and EB that are determined from crossflow test data.....	56
Table 4.1: Experimental data recorded during a test series in the crossflow test facility	58
Table 4.2: Determined fill characteristic equations for Merkel number for different cross- and counterflow fill configurations.....	59
Table 4.3: Determined fill characteristic equations for loss coefficient different cross- and counterflow fill configurations.....	59
Table B.1: Trickle fill crossflow test results, Part 1	101
Table B.2: Test results for trickle fill in (straight) crossflow, Part 2	102
Table B.3: Dry test results for trickle fill in (straight) crossflow	103
Table B.4: Test results for trickle fill in crossflow (counterflow config.), Part 1	104
Table B.5: Test results for trickle fill in crossflow (counterflow config.), Part 2	106
Table B.6: Dry test results for trickle fill in crossflow (counterflow config.).....	107
Table B.7: Test results for crossflow rain zone, Part 1	108
Table B.8: Test results for crossflow rain zone, Part 2	109
Table B.9: Test results for trickle fill in straight crossflow ($L_{fi,x} = 1.5$ m), Part 1	110
Table B.10: Test results for trickle fill in straight crossflow ($L_{fi,x} = 1.5$ m), Part 2	111
Table B.11: Dry test results for trickle fill in straight crossflow ($L_{fi,x} = 1.5$ m).....	111
Table C.1: Thermocouple channel numbers and correction factors, Part 1	114
Table C.2: Thermocouple channel numbers and correction factors, Part 2	115

LIST OF FIGURES

Figure 1.1: Cooling towers	1
Figure 1.2: Diagram of a cooling tower in a steam power cycle	2
Figure 1.4: Three fill types	4
Figure 1.5: Different forms of relative flow in a cooling tower	5
Figure 1.6: Segmentation of global electricity production	9
Figure 2.1: An elementary control volume in the fill zone of a rectangular cooling tower	13
Figure 2.2: An internal cell and its neighboring cells in a second order upwind differencing scheme	15
Figure 2.3: Procedure to iteratively solve T_w of an internal cell in the present fill simulation program	18
Figure 2.4: Two iteration sequences that can be used during a Gauss-Seidel solution of the computational domain	19
Figure 2.5: Illustration of the two purposes for which the fill simulation program is used	19
Figure 2.6: Flow diagram of the different ways in which the present fill simulation program solves the Reuter model	20
Figure 2.7: Summary of present fill simulation program output for the example case	22
Figure 2.8: Graphical output of the simulation of the example case using the present fill simulation program, showing air and water properties throughout the computational domain	23
Figure 2.9: Absolute (Abs.) Me/L_{fi} as a function of cell size, shown with its relative difference (Rel.) to a reference Me/L_{fi} for the backward and forward iteration sequences.....	24
Figure 2.10: Me/L_{fi} (absolute) as a function of cell size, shown with its relative difference ⁽¹⁾ to a reference Me/L_{fi} for different types of relative flow	25
Figure 2.11: Comparison between outlet profiles predicted by the present fill simulation program (GRO) and by Gudmundsson (GUD) for crossflow	26
Figure 2.13: Comparison between two methods of predicting drop terminal velocity and experimental data	29

Figure 2.14: Present single drop simulation program results for an example case.....	31
Figure 3.1: Diagram of the fill test facility the Stellenbosch University	34
Figure 3.2: Diagram (side view and top view) of the crossflow test facility.....	35
Figure 3.3: Photo of the empty fill zone in the crossflow test facility.....	36
Figure 3.4: Configuration of an aspirated psychrometer station	38
Figure 3.5: Sensor rake at air outlet.....	38
Figure 3.6: Sensor rake at water outlet	39
Figure 3.7: Locations where water outlet temperatures are measured	39
Figure 3.8: Photo of electromagnetic flow meter installed in water supply line	40
Figure 3.9: Photos of orifice plate installed in water supply line and the pressure transducers to which it is connected.....	40
Figure 3.10: Nozzles for measuring air mass flow rate, seen from the upwind side and the downwind side respectively.....	41
Figure 3.11: One of the pressure taps (U on Figure 3.10 b) that is connected to the pressure transducer that measures the pressure drop over the nozzles.....	41
Figure 3.12: The crossflow test facility control room	42
Figure 3.13: Screenshot of LabView monitor program.....	43
Figure 3.14: Maximum time variance in $T_{ai,1}$ from the sample raw data set	44
Figure 3.15: Deviation in the example case.....	45
Figure 3.16: Example of summarized results from the statistical analysis of a test series	47
Figure 3.17: Set-up to evaluate accuracy of relative temperature measurements.....	50
Figure 3.18: Difference between T measured by some of the thermocouples and T_{true} before and after correction factors were determined and applied.....	50
Figure 3.20: Water distribution tests in progress	52
(Contours show deviation from average measured G_w , $100\% \times (G_w(x,y) - G_{w,avg})/ G_{w,avg}$, in 10% intervals).....	52

Figure 3.21: Comparison between water distribution at $G_w \approx 1.6 \text{ kg m}^{-2} \text{ s}^{-1}$ measured before and after flow reducers were installed in spray frame.	52
Figure 3.22: Final water distribution measured	53
Figure 3.23: Deviations in Me/L_{fi} , K_{fdm}/L_{fi} and EB as a function of deviations in various measurements, as calculated for a specific test case	54
Figure 3.24: Sensitivities of derived quantities to measurement inaccuracies	56
Figure 4.1: Illustration of the three tested fill configurations	57
Figure 4.2: Sample comparison between experimental data from the crossflow test and presented fill characteristic equations for Me/L_{fi} and K_{fdm}/L_{fi}	60
Figure 4.3: Me/L_{fi} predicted by fill characteristic equations, as a function of G_a , for different cross- and counterflow fill configurations and values for G_w	60
Figure 4.4: Me/L_{fi} predicted by fill characteristic equations, as a function of (G_w/G_a) for different cross- and counterflow fill configurations and values for G_w	61
Figure 4.5: Me/L_{fi} predicted by fill characteristic equations, multiplied by G_w , i.e. effectively $h_d A_{fi} / L_{fi}$, as a function of G_a for different cross- and counterflow fill configurations and values for G_w	61
Figure 4.6: K_{fdm}/L_{fi} predicted by fill characteristic equations, as a function of G_a for different cross- and counterflow fill configurations and values for G_w	62
Figure 4.7: Me/L_{fi} for different crossflow fill configurations divided by Me/L_{fi} for fill in counterflow configuration, predicted by the fill characteristic equations, as a function of G_a for different values for G_w	62
Figure 4.8: K_{fdm}/L_{fi} for different crossflow fill configurations divided by K_{fdm}/L_{fi} of fill for fill in counterflow configuration, predicted by the fill characteristic equations, as a function of G_a for different values for G_w	63
Figure 4.9: Relative fill performance predicted by fill characteristic equations, as a function of G_a for different cross- and counterflow fill configurations and values for G_w	63
Figure 4.10: Relative fill performance predicted by fill characteristic equations, as a function of (G_w/G_a) , for different cross- and counterflow fill configurations and values for G_w	64

Figure 5.1: Comparison between the temperature profiles at the air- and water outlets of a rain zone that were predicted (Mod) the by the Reuter model and that were measured (Exp) during experimental tests	66
Figure 5.2: Comparison between the temperature profiles at the air- and water outlet of a trickle fill that were predicted (Mod) by the Reuter model and that were measured (Exp) during experimental tests	66
Figure 5.3: Notable differences between experimental and model results for a rain zone	67
Figure 5.4: Variation in Me/L_{fi} (per zone) in a rain zone for a specific test case.....	68
Figure 5.5: Comparison between experimental results and results from a combination of the Reuter and single drop models	69
Figure 5.6: Most notable differences between experimental and model results for a trickle fill.....	69
Figure 5.7: Comparison between arrangement of fill blocks in the crossflow test section for trickle fill test configurations	70
Figure 5.8: Water mass velocity distribution under 1.5 m trickle fill with $G_w = 4.423 \text{ kg/m}^2\text{s}$	71
Figure 5.9: Water outlet mass velocity profiles caused by drag deflection and redistribution through an infinitely wide fill for various lengths of spray frames with $G_{w, in} = 3 \text{ kg m}^{-2} \text{ s}^{-1}$	72
Figure 5.10: Water outlet mass velocity profiles in crossflow test section calculated for various drag deflection angles (θ) and redistribution half-angles (ψ)	73
Figure A.1: Parameters of single drop case that is used in the sample calculation	85
Figure B.1: Two configurations in which the trickle fill was tested.....	99
Figure B.2: Trickle fill in crossflow, $L_{fi,x} = 1.5 \text{ m}$ configuration.....	99
Figure C.1: Location of thermocouples inside aspirated thermocouples at the air inlet	112
Figure C.2: Location of the thermocouples inside the aspirated psychrometers downwind of the air mixing vanes	112
Figure D.1: The difference between the previous and the improved equipment to measure the temperature at the water outlet	116

Figure D.2: Comparison between the previous and the improved equipment to measure the temperature at the water outlet	117
Figure D.3: Design view of equipment to measure the temperature of the water at the outlet in Inventor©	117
Figure D.4: Equipment that was designed and manufactured to measure the uniformity of the water distribution in the crossflow test facility	118
Figure D.6: The aspirated psychrometers downwind of the drift eliminators before and after improvement	119
Figure D.7: Aspirated psychrometers that were installed to measure the temperature of the mixed air downwind of the mixing vanes	119
Figure E.1: Comparison of temperature profiles at the outlet predicted by the model and experimentally measured (included on DVD for every crossflow test)	122
Figure E.2: Graphical results from fill simulation program that are included on the DVD for every crossflow test	123

NOMENCLATURE

<p>A Area, m^2</p> <p>a Acceleration, $m\ s^{-2}$</p> <p>a_{fi} Interfacial surface area between air and water per unit volume of fill zone, m^{-1}</p> <p>c_p Specific heat capacity (constant pressure), $J\ kg^{-1}\ K^{-1}$</p> <p>c_{pma} Heat capacity (constant pressure) per kg of dry air, $J\ kg^{-1}\ K^{-1}$</p> <p>c_v Specific heat capacity (constant volume), $J\ kg^{-1}\ K^{-1}$</p> <p>D Diffusion coefficient, $m^2\ s^{-1}$</p> <p>d Diameter, m</p> <p>E Aspect ratio</p> <p>e effectiveness</p> <p>\mathbf{e} Unit vector</p> <p>F Force, N</p> <p>G Mass velocity, $kg\ m^{-2}\ s^{-1}$</p> <p>h Convection heat transfer coefficient, $W\ m^{-2}\ K^{-1}$</p> <p>h_d Mass transfer coefficient (mass base), $m\ s^{-1}$</p> <p>h_D Mass transfer coefficient (mole base), $kg\ m^{-2}\ s^{-1}$</p> <p>i Specific enthalpy, $J\ kg^{-1}$</p> <p>i_{av} Enthalpy of air-vapor mix per kg of air-vapor mixture, $J\ kg^{-1}$</p> <p>i_{fg} Latent heat, $J\ kg^{-1}$</p> <p>i_{ma} Enthalpy of air-vapor mix per kg of dry air, $J\ kg^{-1}$</p> <p>K_{fdm}/L_{fi} Loss coefficient per meter of fill in the direction of air flow, m^{-1}</p>	<p>k Conduction coefficient, $W\ m^{-1}\ K^{-1}$</p> <p>L Length, m</p> <p>M Mass, kg or Molecular weight, $kg\ mol^{-1}$</p> <p>m Mass flow rate, $kg\ s^{-1}$</p> <p>Me/L_{fi} Merkel number per meter of fill in the vertical direction, m^{-1}</p> <p>N Unit number, units</p> <p>NTU Number of transfer units</p> <p>n Total amount of</p> <p>p Pressure, Pa</p> <p>Q Heat transfer rate, W</p> <p>r Radius, m</p> <p>S Source term</p> <p>T Temperature, $^{\circ}C$ or K</p> <p>t Time, s</p> <p>u Specific internal energy, $J\ kg^{-1}$</p> <p>V Volume, m^3</p> <p>v Velocity, m/s or</p> <p>W Work rate, W</p> <p>x Spatial coordinate, m</p> <p>z Elevation, m</p> <p>Greek symbols</p> <p>α Angle of air flow relative to horizontal, $^{\circ}$</p> <p>Δ Differential</p>
---	--

θ	Angle of drop motion, degrees or drag deflection angle, degrees
μ	Dynamic viscosity, kg m ⁻¹ s ⁻¹
ρ	Density, kg/m ³
ρ_{av}	Mass of 1 m ³ of air-vapor mixture, kg/ m ³
σ	Surface tension, N/m
$\Sigma\Delta$	Constant
ψ	Angle of relative velocity between drop and air motion, degrees
ω	Humidity ratio, kg/kg

Subscripts

a	Air
a/d	Relative between drop and air
av	Air-vapor mixture
avg	Average
B	Buoyancy
D	Drag
d	Drop
db	Drybulb
f	Film
fi	Fill
fr	Frontal
i	Inlet
L	Lift
o	Outlet
R	Resultant
s	Saturated
S	Sphere

T	Terminal
t	Total
v	Vapor
W	Weight
w	Water
wb	wetbulb

Dimensionless Groups

$$C_D = \frac{2 F_D}{\rho v^2 A_{fi}} \quad \text{Drag Coefficient}$$

$$C_L = \frac{2 F_L}{\rho v^2 A_{fi}} \quad \text{Lift Coefficient}$$

$$Le_f = \frac{h}{h_d c_{pma}} \quad \text{Lewis factor}$$

$$Me = \frac{h_d a}{m_w} \quad \text{Merkel number}$$

$$Nu = \frac{h L}{k} \quad \text{Nusselt number}$$

$$Re = \frac{\rho v d}{\mu} \quad \text{Reynolds number}$$

$$Pr = \frac{c_p \mu}{k} \quad \text{Prandtl number}$$

$$Sc = \frac{\mu}{\rho D} \quad \text{Schmidt number}$$

$$Sh = \frac{h_D L}{D} \quad \text{Sherwood number}$$

1. INTRODUCTION

1.1. Overview of wet-cooling tower technology

1.1.1. Wet-cooling towers in thermal power cycles

Wet-cooling towers, or simply cooling towers, are used to reject waste heat from processes into the atmosphere. Worldwide, they are mainly used in thermal power plants, usually as part of a steam power cycle. Figure 1.1 shows a photo of three cooling towers.



Figure 1.1: Cooling towers
(Source: carbon-power [Sat])

A diagram of a cooling tower as part of a steam power cycle is shown in Figure 1.2.

In a basic steam power cycle, water is pumped to high pressure and then heated in a boiler until it is a superheated steam. The high pressure superheated steam is then expanded in a turbine, which converts some of the steam's high thermal and mechanical flow energy into mechanical power. A generator, connected by a shaft to the turbine, converts the mechanical power into electrical power. The steam exiting the turbine has a lower pressure and is usually at (or close to) saturation temperature. To complete the cycle, the low pressure steam must be condensed to liquid before it is pumped back to the boiler. For more detail on steam power cycles, see Eastop and McConkey (1993).

When a cooling tower is used in a steam power cycle, the condensation takes place in a surface condenser that is essentially a closed shell-and-tube heat exchanger in which heat is transferred from the working fluid (i.e. the water) in the steam cycle to the cooling water that is circulated through the tubes. The cooling water exiting the condenser is then pumped to the cooling tower.

In the cooling tower, the cooling water is brought into direct contact with air and therefore *evaporative cooling* of the water takes place. Evaporative cooling is an example of simultaneous heat and mass transfer, on which Kröger (2004: 223) provides more detail.

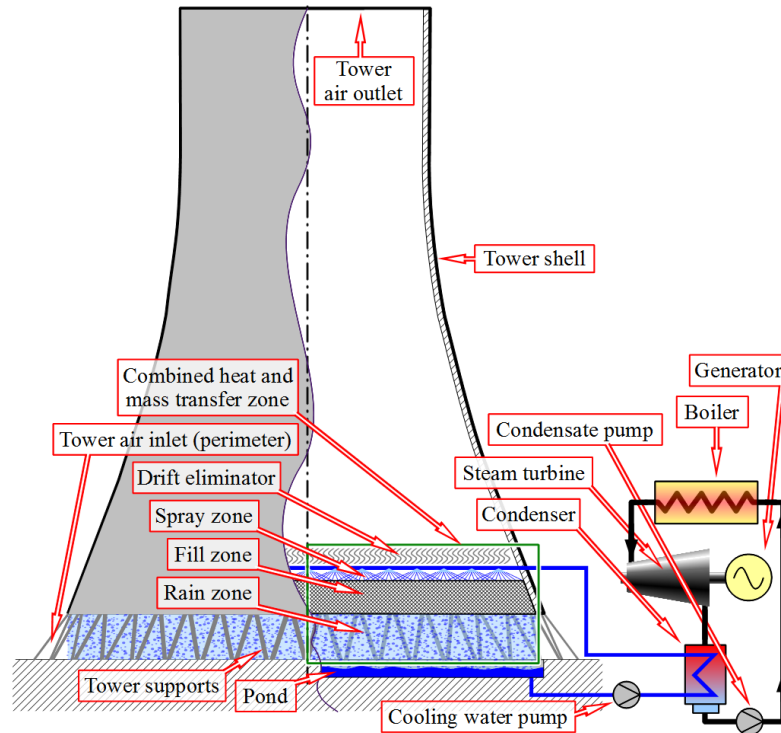


Figure 1.2: Diagram of a cooling tower in a steam power cycle

During evaporative cooling, a small percentage of the water is lost to evaporation (1- 3% according to Kröger 2004: 3). The latent heat of vaporization is drawn from the water's internal energy and causes a significant temperature drop in the water. The heat transferred through evaporation is usually significantly more than the heat transferred through convection.

1.1.2. Operation principle

As is illustrated in Figure 1.2, the cooling water in a cooling tower is circulated through the condenser (in the steam power cycle) and the cooling tower.

The water exiting the heat exchanger is pumped up to the cooling tower water distribution system, which is at the top of the *spray zone*. The water is sprayed into the spray zone through a grid of spray nozzles in order to obtain a near-uniform distribution of water into the *fill zone* beneath it. The water, under the influence of gravity, then passes through the fill zone, which is where most of the cooling takes place. The fill zone is discussed in more detail in Section 1.1.3.

The bottom of the fill zone is usually level with the top of the tower's air inlet, which is all along its perimeter, at the bottom of the tower (see Figure 1.2). Once the water reaches the bottom of the fill zone, it free-falls through the *rain zone* and

is collected in a pond. The collected water is pumped back to the condenser to complete the cooling water cycle.

Air is drawn into the cooling tower through the air inlet. The air then passes through the rain zone before progressing upwards into the cooling tower. Air flow through the cooling tower is achieved by a natural draft, which may be assisted by fans. A natural draft exploits the higher buoyancy of the heated air in order to achieve air flow through the tower. For more detail on natural drafts and fans in cooling towers, see Kröger (2004: 6).

Drift eliminators are installed above the spray zone to reduce *drift losses* (discussed in Section 1.1.3).

1.1.3. The fill zone, fill performance characteristics and different fill types

The fill zone in a cooling tower is packed with *fill*. Fill is designed to increase cooling by increasing the interfacial surface area between the water and the air and/or by retarding the water and thereby keeping it in contact with the air for a longer time.

Fill performance characteristics are traditionally expressed in terms of the Merkel number Me and the loss coefficient K_{fdm} . These are introduced below.

To evaluate and compare thermal performance of fills, Merkel (1925) derived a non-dimensional coefficient of performance or transfer characteristic, now known as the Merkel number Me . In this study, the Merkel number is always divided by the fill height in the vertical direction $L_{fi,z}$ and expressed as Me/L_{fi} , for which the definition is given in Equation (1.1).

$$\frac{Me}{L_{fi,z}} = \frac{h_d a_{fi} A_{fi}}{m_w} = \frac{h_d a_{fi}}{G_w} = \frac{1}{L_{fi}} \int_{T_{wo}}^{T_{wi}} \frac{c_{pw}}{(i_{masw} - i_{ma})} dT_w \quad (1.1)$$

The degree to which a fill resists air flow through it is expressed as the mean fill loss coefficient per meter fill (K_{fdm}/L_{fi}). Kröger (2004: 274) derives Eq. (1.2) by using a combination of energy and momentum conservation equations.

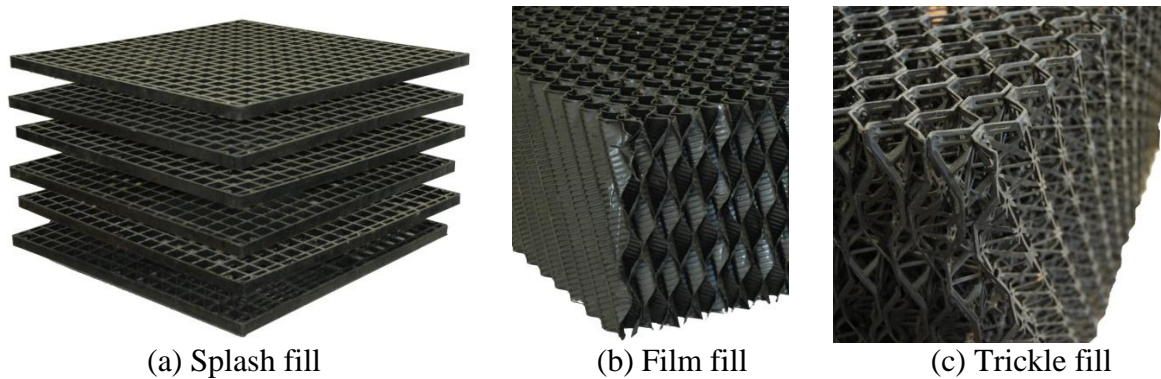
$$\frac{K_{fdm}}{L_{fi,a}} = \frac{2\rho_{av,avg} A_{fr}^2 \left[\Delta p_{fi} - (\rho_{avo} v_{avo}^2 - \rho_{avi} v_{avi}^2) + (\rho_{avi} - \rho_{av,avg}) g L_{fi,z} \right]}{m_{av,avg}^2 L_{fi,a}} \quad (1.2)$$

(Note that $L_{fi,a}$ in the Eq. (1.2) refers to the fill length in the direction of the air flow, while $L_{fi,z}$ will always refer to the vertical fill height. The term $(\rho_{avi} - \rho_{avm}) g L_{fi,z}$ is concerned with buoyancy effects, and this should be remembered when the loss coefficient is calculated for non-vertical air flow cases, such as crossflow cases)

An ideal fill has a high Me/L_{fi} and a low K_{fdm}/L_{fi} . Both these performance characteristics (Me/L_{fi} and K_{fdm}/L_{fi}) have been observed to vary for different air- and water mass velocities, and for this reason fill performance characteristics are often

given as functions of air- and water mass velocity. Me/L_{fi} is also sometimes expressed as a function of inlet water temperature.

There are three basic types of fill, shown in Figure 1.4.



(a) Splash fill

(b) Film fill

(c) Trickle fill

Figure 1.4: Three fill types

Splash fill breaks water up into smaller drops, thereby increasing the interfacial surface area between the water and the air. Smaller drops also fall slower and therefore stay in contact with the air for a longer time. However, the smaller drops may be entrained by the air and lost into the atmosphere. This additional loss of water is called *drift loss*.

Film fills address the problem of drift loss by spreading the water out in a thin layer over a large surface area, rather than breaking it up into drops. Film fills tend to allow for better cooling performance, but at the cost of higher flow losses.

Trickle fill is essentially a hybrid between film fill and splash fill with characteristics in-between the two.

1.1.4. Forms of relative flow in cooling towers

In cooling towers, three forms of relative flow between the water and the air occur: crossflow, counterflow and cross-counterflow. These are illustrated in Figure 1.5, which is a magnification of the combined heat and mass transfer zone indicated in Figure 1.2.

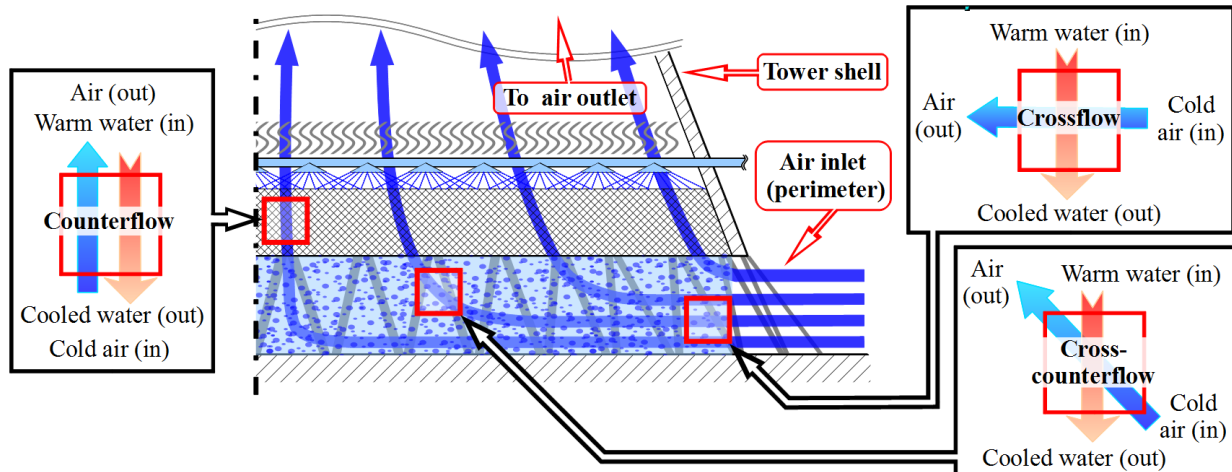


Figure 1.5: Different forms of relative flow in a cooling tower

The variation in the form of relative flow within the combined heat and mass transfer zone complicates the modeling of cooling towers.

1.1.5. Anisotropic fill performance characteristics

Splash fills and trickle fills are porous in all directions and air can flow through them at any angle, thereby allowing for crossflow, counterflow or cross-counterflow. It is shown in this study that the fill performance characteristics for a trickle fill can be dependent on the form of relative flow through it. A porous medium of this type is called *anisotropic* (as opposed to an *isotropic* medium, which behaves the same way in all directions).

Film fill, on the other hand, is usually *orthotropic*, which means that it is porous in a single direction and air can only pass through it in that direction. For this reason, film fill is effectively always in counterflow and is therefore simpler to model.

In order to accurately model a cooling tower packed with splash- or trickle fill, the flow mode-dependent (i.e. anisotropic) performance characteristics of the fill need to be taken into account.

Very few literature sources could be found concerning anisotropic fill behavior. De Villiers (1998) discusses the anisotropic characteristics of cooling tower rain zones, while Reuter (2010) investigates the modeling of anisotropic fills in CFD.

1.2. Performance prediction of cooling towers

In cooling tower spray-, fill- and rain zones, the local air flow, water flow, heat transfer and mass transfer are complex and interdependent. They are also highly dependent on the often complex geometry of the cooling tower. These complexities and interdependencies make the modeling and performance prediction of cooling towers difficult.

In the past, these complexities were handled by using simplified numerical models and/or methods of scaling. There are briefly discussed in Section 1.2.1. More re-

cently, advances in the field of computational fluid dynamics (CFD) and the dramatic increase in the computational speed of computers has led to the application of CFD in cooling tower performance prediction and this has opened up new doors for cooling tower design improvement. These newer methods are briefly discussed in Section 1.2.2.

1.2.1. Simplified methods of modeling cooling towers

Kröger (2004b: 51) lists six different 2-dimensional numerical models that have been developed to determine the performance characteristics of cooling towers, but stresses that even the most sophisticated among them make use of simplifying assumptions and empirical and experimental data. Kröger also states that the results from these models are not necessarily better than those from one dimensional models.

According to Reuter (2010: 1.3), the models used by the main suppliers of cooling tower technologies rely on basic models to predict the fluid mechanics in the towers and on performance characteristics that are determined by applying simplified methods of analysis on experimental test data. These models are overviewed in Section 2.1. Reuter argues that these models are better described as performance adjustment tools and that they are essentially used to scale old designs to meet new requirements. Since scaling requires dimensional similitude, the basic design has remained constrained and there has been no essential improvement in cooling tower design for decades.

1.2.2. The use of CFD to model cooling towers

Al-Waked (2006, 2007, 2010), Williamson (2008a, 2008b, 2008c), Klimanek (2008, 2009, 2010) and Reuter (2010) have investigated methods to model cooling towers using CFD. Reuter states that the work by the other aforementioned researchers is only applicable on cooling towers fitted with fill that only allows for air flow in one direction, and has a relatively high loss coefficient.

However, many cooling towers are fitted with fill that allows air flow in all directions (such as trickle and splash fills). Reuter (2010) therefore investigates the use of CFD to model such cooling towers and he presents a method to model 2-dimensional air flow through the fill, and the associated heat and mass transfer, in CFD. His method involves integrating a set of evaporative cooling equations that he derives from first principles, into the CFD simulation through the use of user defined functions (UDFs). This set of equations, referred to as the Reuter 2-dimensional evaporative cooling model, or simply as the Reuter model, essentially calculates the heat and mass transfer between the water and the air as a function of T_w , T_a , ω , G_w , G_a , Me/L_{fi} and Le_f . The Reuter model can also be implemented into a computer program, which can be used to determine or to evaluate fill performance characteristics without using commercial CFD software.

In order to accurately model anisotropic fills, such as trickle- or splash fills, in CFD, the fact that their performance characteristics differ depending on the direction of air and water flow through them must be taken into account. Their performance characteristics in cross-counterflow are expected to be in-between their

crossflow and counterflow performance characteristics. However, the available fill test facilities are limited to determine either crossflow or counterflow fill performance characteristics. In order to model fill in cross-counterflow, Reuter proposes using a linear interpolation between the crossflow and counterflow fill performance characteristics, based on air flow angle. Reuter's equation, used to determine the Me/L_{fi} of a fill in cross-counterflow, is given as

$$\left(\frac{Me}{L_{fi,z}}\right)_{\text{cross-counter}} = \left\{ \left(\frac{Me}{L_{fi,z}}\right)_{\text{counter}} + \left[\left(\frac{Me}{L_{fi,z}}\right)_{\text{cross}} - \left(\frac{Me}{L_{fi,z}}\right)_{\text{counter}} \right] \left(\frac{90^\circ - \varphi}{90^\circ} \right) \right\} \quad (1.3)$$

where φ is the angle of air flow relative to the horizontal.

If the difference between fill performance characteristics in crossflow and counterflow is relatively small, then the interpolation error should also be reasonably small.

However, even if an interpolation method is to be used, crossflow and counterflow performance characteristics for a fill are still required to model 2-dimensional air flow through cooling towers in CFD using Reuter's model. These performance characteristics need to be determined through performance comparable tests in separate crossflow and counterflow fill test facilities.

1.3. Experimental work preceding this project

Banda (2008), Terblanche (2008), Duss (2009) and Bertrand (2011) have all made significant contributions to a continued process to improve the once basic fill test facilities at the Stellenbosch University. These facilities were first constructed in the 1980s and consist of both a crossflow and a counterflow test facility. Both of these test facilities were critically evaluated and used for various fill tests during the aforementioned studies, but performance comparable crossflow and counterflow tests were never attempted.

The most recent work by Bertrand on the counterflow test facility is quite comprehensive and his work may be referenced for a critical evaluation of that test facility. Bertrand shows that the counterflow facility is not, at this point, suitable for measuring the performance of splash fills due to excessive migration of water to the tower walls during splash fill tests. However, Bertrand performed a series of counterflow fill tests using the trickle fill that is shown in Figure 1.4 (c) and it is possible to do performance comparable tests with this fill in the crossflow facility in order to determine its anisotropic performance characteristics.

1.4. Objectives

The primary goal of this project is to investigate the difference between the crossflow and the counterflow fill performance characteristics of a trickle fill. If it can be shown that the relative difference is small, then worst-case interpolation error that one would make when using Reuter's proposed linear interpolation (discussed in Section 1.2.2) can be expected to be accordingly small.

In that case, Reuters proposed linear interpolation can be used with relative confidence.

As a secondary goal, the validity of the Reuter model is investigated by comparing its predictions of temperature profiles at the air- and water outlets to those experimentally measured.

The following objectives are set in order to reach these two goals:

1. Critically evaluate the crossflow fill test facility at Stellenbosch University and make improvements where necessary.
2. Design, manufacture and install sensor rakes in the crossflow test facility so that the temperature profiles at the air and water outlets can be measured and compared to model predictions.
3. Perform crossflow tests in the upgraded test facilities with a trickle fill in two different configurations. Ensure that these tests are performance comparable to the trickle fill tests that Bertrand (2011) did. Additionally, perform rain zone tests. Measure and record the temperature profiles at the air and water outlets during all tests.
4. Investigate the differences between the performance characteristics of a trickle fill in crossflow and in counterflow by comparing the recorded test data to Bertrand's data and discuss the differences.
5. Implement the Reuter 2-dimensional evaporative cooling model and the single drop model (introduced in Chapter 2) into a computer program and verify that they are correctly implemented by comparing their outputs to published results from Reuter (2010) and Gudmundsson (2012). Report any valuable lessons that are learned during the process.
6. Compare the temperature profiles at the air and water outlets that are predicted using the Reuter model and the single drop model to those that are measured experimentally. Investigate and discuss the reasons for any differences between the experimental results and model predictions. Make a conclusion about the performance of the Reuter model.
7. Make recommendations for future research about further improving the crossflow test facility at Stellenbosch, about performing crossflow tests and about the implementation of the Reuter model and single drop model into computer programs.

1.5. Motivation

Reaching the project goals will contribute to the advancement of cooling tower design using CFD and the consequent potential improvement of cooling tower performance.

Reuter (2010) shows that, if a cooling tower could be improved so that the steam turbine exhaust / condenser temperature of a typical coal-fired plant can be lowered by 3 °C, the gross efficiency of the plant may increase by 1%. One percent may not look like much at first glance, but the sheer scale of power plants would translate a one percent improvement to a significant increase in plant profitability.

Cooling towers are very prevalent in the thermal power generation industry, which, according to [Energies-renouvelables.org](http://energies-renouvelables.org), currently produce approximately 81% the world's electricity, as is illustrated in Figure 1.6 (fossil fuel, nuclear and geothermal are all thermal power).

Figure 1.6 also reveals that the world economies currently depend on fossil fuels for two thirds of all power generated. Experts in the fossil fuel industry agree that fossil fuel reserves will not last much longer than another century. Shafiee and Topal (2008) predict the depletion dates for oil, coal and gas as the years 2040, 2112 and 2042 respectively.

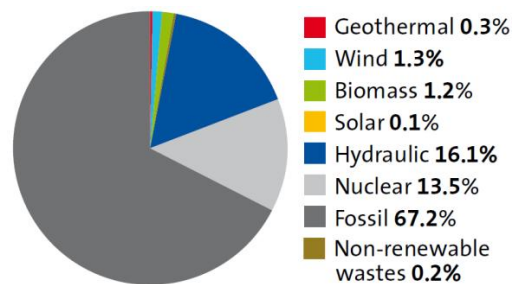


Figure 1.6: Segmentation of global electricity production

(source: www.energies-renouvelables.org)

Yet, even as the fossil fuel reserves run out, the world population is increasing at an unprecedented rate and economies are growing, demanding more electricity than ever before. It is therefore clear that the world is heading for an energy crisis unless alternative sources of electricity can be tapped into before the fossil fuel reserves are depleted.

On top of this, there are grave environmental concerns associated with the expanding power generation industry. CO₂ emissions and other forms of pollution are rife and the consequences are being felt worldwide: in soil degradation, ground water poisoning, desertification and loss of natural heritage, to name but a few. Climate change and associated natural disasters such as drought and flooding are also widely attributed to CO₂ emissions caused by human activity.

Improved cooling tower technology could increase the fuel-efficiency of both new and old (by upgrading) thermal power plants. This would have the following benefits:

1. In effect, the lifetime of the fossil fuel reserves would be extended. This would give the world economy more time to break from its dependency on fossil fuels and would hopefully contribute to avoiding a global energy crisis.
2. Thermal power plants would become more profitable. This may be vital for the fossil fuel plants, since fuel costs are expected to rise significantly as reserves diminish.
3. Increasing thermal power plant fuel-efficiency would reduce pollution and waste production by such plants and therefore benefit the environment.

1.6. Thesis outline

Chapter 1: INTRODUCTION

An overview of wet cooling tower technology is provided, with a focus on the aspects that are relevant to this project. The challenges in present day cooling tower design improvement are discussed. The contribution that is to be made through

this project, within the context of a greater research effort at Stellenbosch University to develop an improved model for the performance prediction of cooling towers, is explained. Finally, the project objectives and motivation are stated and this thesis outline is provided.

Chapter 2: METHODS USED TO MODEL WET-COOLING

Evaporative cooling models that are currently the most commonly used in industry are briefly discussed and then the Reuter 2-dimensional evaporative cooling model and the single drop model are introduced. The governing partial differential equations and discrete forms of the governing equations solved in these models are presented. Solution methods and the implementation of the models into computer programs are explained with a level of detail that is sufficient to reproduce the computer programs with improved solution methods that were developed during the course of this study. Results from the computer programs are validated against results published by Reuter (2010) and Gudmundsson (2012).

Chapter 3: EXPERIMENTAL APPARATUS AND METHODOLOGY

The crossflow fill test facility at Stellenbosch University and the measurement techniques used within it are described. The data processing process is also described and a critical analysis of the facility is presented. The uncertainties in all of the measurements are also determined and their combined effect on the measured Me/L_{fi} , K_{fdm}/L_{fi} and EB is investigated.

A brief report of all the work that was done to improve the crossflow test facility as part of this project is provided in Appendix D.

Chapter 4: COMPARISON OF CROSSFLOW AND COUNTERFLOW FILL PERFORMANCE

The difference between the performance characteristics of a trickle fill in crossflow- and in counterflow is investigated. This is done by comparing characteristic equations that are fitted to experimental data measured in the crossflow facility as part of this project to characteristic equations fitted to data from performance comparable tests by Bertrand (2011).

The equations are plotted to various graphs and the observations made and insights gained are discussed.

Chapter 5: COMPARISON BETWEEN EXPERIMENTAL RESULTS AND THE MODEL PREDICTIONS

The temperature profiles at the air- and water outlet that are measured during experimental crossflow tests are compared to the profiles predicted using the Reuter model for both rain zone and trickle fill tests. Reasons for the differences between model predictions and experimental results are discussed.

Chapter 6: CONCLUSIONS AND RECOMMENDATIONS

The work done in order to achieve the project objectives is summarized and the main outcomes are highlighted. The significance of the project findings is discussed and recommendations for ongoing study are made.

Appendices

The following supplementary information is provided in appendices:

APPENDIX A: Sample calculations

APPENDIX B: Crossflow test results in table form

APPENDIX C: Detailed information about thermocouples in the crossflow test facility

APPENDIX D: Report on improvements made to the crossflow test facility

APPENDIX E: Content of DVD submitted with thesis

2. METHODS USED TO MODEL WET-COOLING

2.1. Fill models currently used in industry and their shortcomings

According to Reuter (2010), the Merkel (Merkel, 1925), *e-NTU* (Jaber and Webb, 1989) and Poppe (Poppe and Rögener, 1991) methods of analysis are currently the most commonly used in industry to analyze and predict wet-cooling. Kloppers and Kröger (2005) critically evaluate these three methods.

Both the Merkel and *e-NTU* methods make use of the following three simplifying assumptions:

- The Lewis factor, Le_f , relating heat and mass transfer, is equal to 1.
- The air exiting the fill is saturated with water vapor and it is characterized only by its enthalpy.
- The reduction of water flow rate by evaporation is neglected in the energy balance.

The *e-NTU* and Merkel methods therefore do not accurately predict the state of the outlet air. Yet, the state of the outlet air is important when attempting plume abatement or when calculating the strength of the natural draft through cooling towers, which is a function of the density of the outlet air. The Poppe method does not make the simplifying assumptions of the Merkel and *e-NTU* methods and can be used to predict the state of the outlet air. However, since the Poppe method is derived in such a way that it can only be applied to strictly crossflow or strictly counterflow scenarios, it does not suffice to model fill in cross-counterflow.

In Appendix A.4, a sample calculation is provided for calculating the Merkel number from crossflow fill test results using the *e-NTU* method. Kloppers presents a sample calculation for a counterflow Poppe method.

2.2. The Reuter 2-dimensional evaporative cooling model

Reuter (2010) addresses the shortcomings of the Poppe model by developing a new 2-dimensional fill model, primarily for direct comparison to CFD results. Similar to Poppe, Reuter derived his equations from first principles, but unlike Poppe, he made provision for cross-counterflow in his equations. In order to compare the predictions made by the Reuter model to the experimental results, a fill simulation program, which is a direct numerical implementation of Reuter's model, is written as part of this project.

Gudmundsson (2012) does an extensive comparative investigation of the Reuter model against the Merkel, *e-NTU* and Poppe methods for cross- and counterflow cases. Gudmundsson also investigated various ways to numerically solve Reuter's model and his recommendations are implemented in this project: Reuter used differential equations for air temperature to solve his model, but Gudmundsson found that these equations became difficult to solve when the air became super-saturated and he suggested the use of equations for air-vapor enthalpy instead. Also, Gudmundsson applied a second order linear upwind differencing scheme to

the model instead of the first order upwind method and, in so doing, achieved a significant improvement in grid independence.

2.2.1. Assumptions made in the Reuter model

Because the nature of the interaction between the fill material, the water and the air inside the fill is complex and therefore difficult to model, the Reuter model makes the assumption that the flow direction of the water always remains vertical. This assumption prevents a direct numerical implementation of the Reuter model to take into consideration that the water is redistributed by the fill's geometry and that the water is dragged along by the air in certain cases. Some differences between the Reuter model predictions and experimental trickle fill test results are therefore to be expected.

Reuter's (2010) and Gudmundsson's (2012) direct numerical implementations of the Reuter model assume a constant and uniform Me/L_{fi} within the computational domain. However, it is possible (and sometimes useful) to implement the Reuter model using a non-uniform Me/L_{fi} , as is demonstrated in Section 5.2.

The Reuter model also does not provide equations that solve the air pressure and velocity fields within the fill, since this is normally handled by the CFD software into which the Reuter model is integrated. In a direct numerical implementation of the Reuter model, uniform and constant air pressure and velocity is therefore assumed. However, in reality, there exists a pressure gradient over the fill. Some of the equations used in the model have a slight dependence on pressure, but their sensitivity to the relatively small difference in pressure is considered negligible. It is also known that in reality, air velocity may be not entirely uniform due to non-uniform expansion of air and/or non-uniform air resistance of the fill. The variance in air velocity is, however, not expected to be very significant.

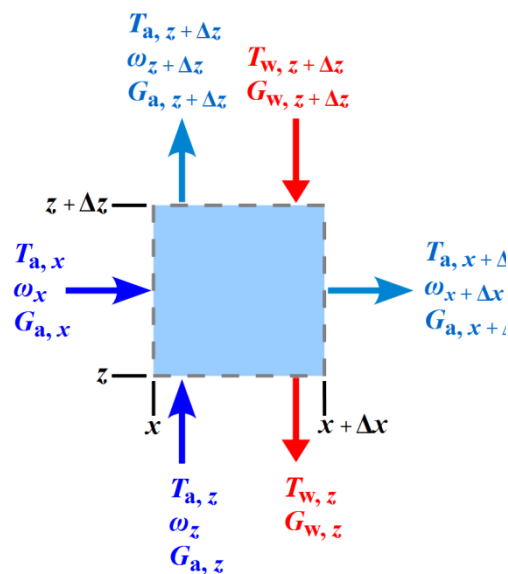


Figure 2.1: An elementary control volume in the fill zone of a rectangular cooling tower

2.2.2. Governing differential equations

Figure 2.1 shows an elementary control volume in a rectangular cooling tower fill zone. Since Reuter makes the assumption that water flow is only vertical, there is no term $G_{w,x}$ and horizontal flow of water is ignored in the model.

Reuter (2010) presents the derivation of his model for a circular cooling tower, in axisymmetric coordinates, and gives the governing differential equations for a rectangular tower. Gudmundsson (2012) presents the full derivation for a rectangular cooling tower. The derivations are not repeated in this text, but the derived

governing partial differential equations, for a rectangular cooling tower, are provided below.

For under-saturated air:

$$\frac{\partial G_w}{\partial z} = h_d a_{fi} (\omega_{s(T_w)} - \omega) \quad (2.1)$$

$$\frac{\partial T_w}{\partial z} = \frac{c_{pma} h_d a_{fi}}{c_{pw} G_w} \left[Le_f (T_w - T_a) + \frac{i_{fg(T_w)}}{c_{pma}} (\omega_{s(T_w)} - \omega) \right] \quad (2.2)$$

$$G_{a,z} \frac{\partial \omega}{\partial z} + G_{a,x} \frac{\partial \omega}{\partial x} = h_d a_{fi} (\omega_{s(T_w)} - \omega) \quad (2.3)$$

$$G_{a,z} \frac{\partial i_{ma}}{\partial z} + G_{a,x} \frac{\partial i_{ma}}{\partial x} = h_d a_{fi} \left[Le_f c_{pma} (T_w - T_a) + i_{v(T_w)} (\omega_{s(T_w)} - \omega) \right] \quad (2.4)$$

For super-saturated air:

$$\frac{\partial G_w}{\partial z} = h_d a_{fi} (\omega_{s(T_w)} - \omega_s) \quad (2.5)$$

$$\frac{\partial T_w}{\partial z} = \frac{c_{pma} h_d a_{fi}}{c_{pw} G_w} \left[Le_f c_{pma} (T_w - T_a) + \frac{i_{fg(T_w)}}{c_{pma}} (\omega_{s(T_w)} - \omega_s) \right] \quad (2.6)$$

$$G_{a,z} \frac{\partial \omega}{\partial z} + G_{a,x} \frac{\partial \omega}{\partial x} = h_d a_{fi} (\omega_{s(T_w)} - \omega_s) \quad (2.7)$$

$$G_{a,z} \frac{\partial i_{ma}}{\partial z} + G_{a,x} \frac{\partial i_{ma}}{\partial x} = h_d a_{fi} \left[Le_f c_{pma} (T_w - T_a) + i_{v(T_w)} (\omega_{s(T_w)} - \omega_s) \right] \quad (2.8)$$

where

$$i_{v(T_w)} = i_{fg0} + c_{pv} T_w (^\circ\text{C}) \quad \text{with } i_{fg0} = i_{fg(T=273.15\text{K})} = 2.5016 \times 10^6 \text{ J/kg} \quad (2.9)$$

and c_{pv} is evaluated at $(T_w + 273.15)/2$

In Eqs. (2.1) to (2.8), the thermophysical properties i_{fg} , ω_s , c_{pw} and c_{pma} are evaluated using the correlations from Kröger (2004). Many of these correlations are functions of T_a , which is obtained iteratively by solving Kröger's correlation for i_{ma} , given in Eq. (2.10), using a known i_{ma} and ω .

$$i_{ma}(T_a, \omega) = c_{pa}(T_a) + \omega \left[2.5016 \times 10^6 + c_{pv}(T_a) (T_a - 273.15) \right] \quad (2.10)$$

(T_w) in the subscript of a property means that the property is calculated using water (not air) temperature.

Le_f is determined using Bosnjakovic's (1960) relation:

$$Le_f = \frac{h}{h_d c_{pma}} = 0.865^{0.667} \left(\frac{\omega_{sw} + 0.622}{\omega + 0.622} - 1 \right) / \ln \left(\frac{\omega_{sw} + 0.622}{\omega + 0.622} \right) \quad (2.11)$$

2.2.3. Discretization of the governing differential equations

In order to use Eqs. (2.1) to (2.8) to numerically model a 2-dimensional fill zone, the zone is divided into $n_x \times n_z$ control volumes (or cells) of dimension $\Delta x \times \Delta z$,

which together form a computational domain. An internal cell within the computational domain is shown in Figure 2.2.

If the fill length in the definition of Me/L_{fi} Eq. (1.1) is taken as the height of a cell (Δz), Eq. (1.1) may be rearranged as follows:

$$h_d a_{fi} = \frac{Me_c G_w}{\Delta z} \quad (2.12)$$

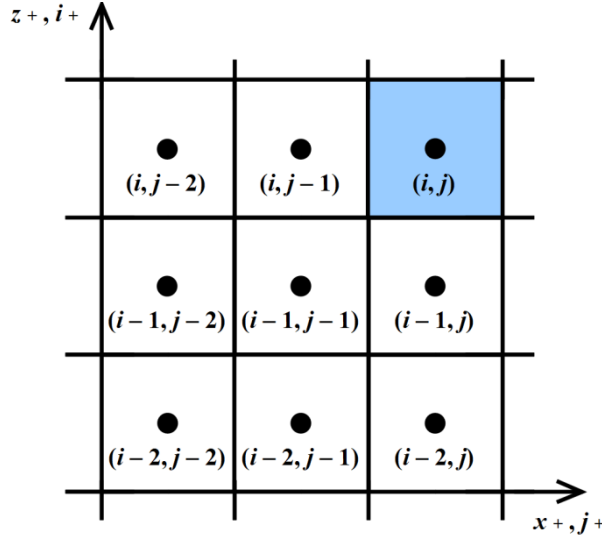


Figure 2.2: An internal cell and its neighboring cells in a second order upwind differencing scheme

Eq. (2.12) may now be substituted into the governing differential equations (Eq. (2.1) to (2.8)) to eliminate the term $h_d a_{fi}$. Since these equations represent gradients, they may be written as source terms.

For under-saturated air and saturated air:

$$\frac{S_{G_w}}{\Delta z} = \frac{\partial G_w}{\partial z} = Me_c G_w (\omega_{s(T_w)} - \omega) \quad (2.13)$$

$$\frac{S_{T_w}}{\Delta z} = \frac{\partial T_w}{\partial z} = \frac{Me_c c_{pma}}{c_{pw}} \left[Le_f (T_w - T_a) + \frac{i_{fg}(T_w)}{c_{pma}} (\omega_{s(T_w)} - \omega) \right] \quad (2.14)$$

$$\frac{S_{\omega}}{\Delta z} = G_{a,z} \frac{\partial \omega}{\partial z} + G_{a,x} \frac{\partial \omega}{\partial x} = Me_c G_w (\omega_{s(T_w)} - \omega) \quad (2.15)$$

$$\begin{aligned} \frac{S_{i_{ma}}}{\Delta z} &= G_{a,z} \frac{\partial i_{ma}}{\partial z} + G_{a,x} \frac{\partial i_{ma}}{\partial x} \\ &= Me_c G_w \left[Le_f c_{pma} (T_w - T_a) + (i_{fg0} + c_{pv} T_w(^{\circ}C)) (\omega_{s(T_w)} - \omega) \right] \end{aligned} \quad (2.16)$$

For super-saturated air:

$$\frac{S_{G_w}}{\Delta z} = \frac{\partial G_w}{\partial z} = Me_c G_w (\omega_{s(T_w)} - \omega_s) \quad (2.17)$$

$$\frac{S_{T_w}}{\Delta z} = \frac{\partial T_w}{\partial z} = \frac{Me_c c_{pma}}{c_{pw}} \left[Le_f (T_w - T_a) + \frac{i_{fg}(T_w)}{c_{pma}} (\omega_{s(T_w)} - \omega_s) \right] \quad (2.18)$$

$$\frac{S_\omega}{\Delta z} = G_{a,z} \frac{\partial \omega}{\partial z} + G_{a,x} \frac{\partial \omega}{\partial x} = Me_c G_w (\omega_{s(T_w)} - \omega_s) \quad (2.19)$$

$$\begin{aligned} \frac{S_{i_{ma}}}{\Delta z} &= G_{a,z} \frac{\partial i_{ma}}{\partial z} + G_{a,x} \frac{\partial i_{ma}}{\partial x} \\ &= Me_c G_w \left[Le_f c_{pma} (T_w - T_a) + (i_{fg0} + c_{pv} T_w(^{\circ}C)) (\omega_{s(T_w)} - \omega_s) \right] \end{aligned} \quad (2.20)$$

2.2.4. The second order upwind differencing scheme

The properties of an internal cell are determined by using a second order upwind differencing scheme, for which the equations for an internal cell are given below.

For the water side:

$$\varphi_{(i,j)} = \frac{4\varphi_{(i-1,j)} - \varphi_{(i-2,j)} + 2S_{\varphi(i,j)}}{3} \quad (2.21)$$

where φ may represent either G_w or T_w .

For the air side:

$$\varphi_{(i,j)} = \frac{G_{a,x} \frac{\Delta z}{\Delta x} (4\varphi_{(i,j-1)} - \varphi_{(i,j-2)}) + G_{a,z} (4\varphi_{(i-1,j)} - \varphi_{(i-2,j)}) + 2S_{\varphi(i,j)}}{3 \left(G_{a,x} \frac{\Delta z}{\Delta x} + G_{a,z} \right)} \quad (2.22)$$

where φ may represent either ω or i_{ma} .

Eq. (2.21) and (2.22) can only be used for internal cells, i.e. cells with $i > 2$ and $j > 2$. Special forms of the equations are required for cells where $i \leq 2$ and/or $j \leq 2$, and these are provided below.

For the water side:

$$\varphi_{(1,j)} = \varphi_{BC} + \frac{S_{\varphi(1,j)}}{2} \quad (2.23)$$

$$\varphi_{(2,j)} = \frac{5\varphi_{(1,j)} - 2\varphi_{BC} + 2S_{\varphi(2,j)}}{3} \quad (2.24)$$

where (again) φ may represent either G_w or T_w .

For the air side:

$$\varphi_{(1,1)} = \varphi_{BC} + \frac{S_{\varphi(1,1)}}{G_{a,x} \frac{\Delta z}{\Delta x} + G_{a,z}} \quad (2.25)$$

$$\varphi_{(2,1)} = \frac{\frac{5}{2} G_{a,z} \varphi_{(1,1)} + \left(2 G_{a,x} \frac{\Delta z}{\Delta x} - G_{a,z} \right) \varphi_{BC} + S_{\varphi(2,1)}}{2 G_{a,x} \frac{\Delta z}{\Delta x} + \frac{3}{2} G_{a,z}} \quad (2.26)$$

$$\varphi_{(1,2)} = \frac{\frac{5}{2} G_{a,x} \frac{\Delta z}{\Delta x} \varphi_{(1,1)} - \left(G_{a,x} \frac{\Delta z}{\Delta x} - 2 G_{a,z} \right) \varphi_{BC} + S_{\varphi(2,1)}}{\frac{3}{2} G_{a,x} \frac{\Delta z}{\Delta x} + 2 G_{a,z}} \quad (2.27)$$

$$\varphi_{(2,2)} = \frac{5 G_{a,x} \frac{\Delta z}{\Delta x} \varphi_{(2,1)} + 5 G_{a,z} \varphi_{(1,2)} - 2 \left(G_{a,x} \frac{\Delta z}{\Delta x} + G_{a,z} \right) \varphi_{BC} + 2 S_{\varphi(2,1)}}{3 \left(G_{a,x} \frac{\Delta z}{\Delta x} + G_{a,z} \right)} \quad (2.28)$$

For all the other cells in the first and second column:

$$\varphi_{(i,1)} = \frac{2 G_{a,z} \varphi_{(i-1,1)} - \frac{1}{2} G_{a,z} \varphi_{(i-2,1)} + 2 G_{a,x} \frac{\Delta z}{\Delta x} \varphi_{BC} + S_{\varphi(i,1)}}{2 G_{a,x} \frac{\Delta z}{\Delta x} + \frac{3}{2} G_{a,z}} \quad (2.29)$$

$$\varphi_{(i,2)} = \frac{5 G_{a,x} \frac{\Delta z}{\Delta x} \varphi_{(i,1)} - 2 G_{a,x} \frac{\Delta z}{\Delta x} \varphi_{BC} + 4 G_{a,z} \varphi_{(i-1,2)} - G_{a,z} \varphi_{(i-2,2)} + 2 S_{\varphi(i,2)}}{3 \left(G_{a,x} \frac{\Delta z}{\Delta x} + G_{a,z} \right)} \quad (2.30)$$

For all the other cells in the first and second row:

$$\varphi_{(1,j)} = \frac{2 G_{a,x} \frac{\Delta z}{\Delta x} \varphi_{(1,j-1)} - \frac{1}{2} G_{a,x} \frac{\Delta z}{\Delta x} \varphi_{(1,j-2)} + 2 G_{a,z} \varphi_{BC} + S_{\varphi(1,j)}}{\frac{3}{2} G_{a,x} \frac{\Delta z}{\Delta x} + 2 G_{a,z}} \quad (2.31)$$

$$\varphi_{(2,j)} = \frac{4 G_{a,x} \frac{\Delta z}{\Delta x} \varphi_{(2,j-1)} - G_{a,x} \frac{\Delta z}{\Delta x} \varphi_{(2,j-2)} + 5 G_{a,z} \varphi_{(1,j)} - 2 G_{a,z} \varphi_{BC} + 2 S_{\varphi(2,j)}}{3 \left(G_{a,x} \frac{\Delta z}{\Delta x} + G_{a,z} \right)} \quad (2.32)$$

In Equations (2.25) to (2.32), φ may represent (again) either ω or i_{ma} .

2.2.5. Iterative solution of a cell

In the present fill simulation program, the discretized governing differential equations, provided in Section 2.2.3 and 2.2.4, are solved iteratively at every cell before moving on to the next cell. The procedure for doing this is illustrated in Figure 2.3.

The alternative is to evaluate the discretized equations only once at every cell before moving on to the next one and when the last cell is reached to start again with the first one until the computational domain has converged as a whole. It was found during the development of the present fill simulation program that the former method is much faster than this latter one.

Also, note the use of relaxation factors in Figure 2.3. These are implemented because it was found that, if the newest property values are used as-is to update the

cell properties, some cells' properties never converge, but indefinitely alternate between two values.

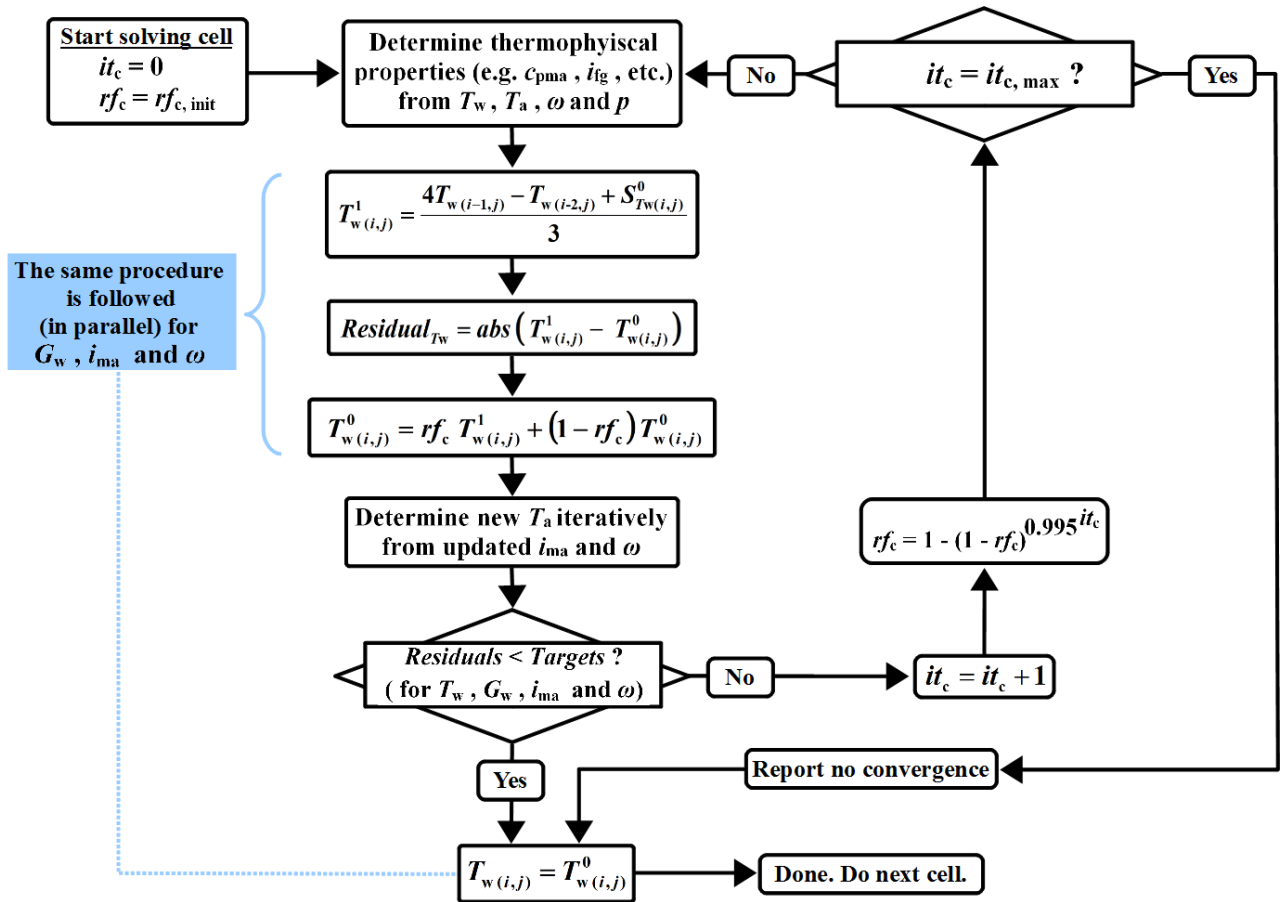


Figure 2.3: Procedure to iteratively solve T_w of an internal cell in the present fill simulation program

2.2.6. Iterative solution of the computational domain

In the present fill simulation program, a Gauss-Seidel method is used to solve the property values of all the cells iteratively. Two different sequences of converging cells are used: Forward and backward. Both the sequences, which are illustrated in Figure 2.4, are briefly discussed because the backward sequence provides much faster solutions, but is only the appropriate choice under certain circumstances as is explained later.

Both the forward and the backward sequence move left to right through all the columns of a given row before going on to the next row. The forward sequence starts with the bottom row, while the backward sequence starts with the top row. (Note that when the backward sequence is used, some of the discretized equations must be changed: The sign of the source term in all the water-side equations must be changed. In all equations $(i-1)$ and $(i-2)$ must be changed to $(i+1)$ and $(i+2)$ respectively. In Eqs. (2.23) to (2.32), the row numbers 1 and 2 must be replaced by n_z and (n_z-1) respectively)

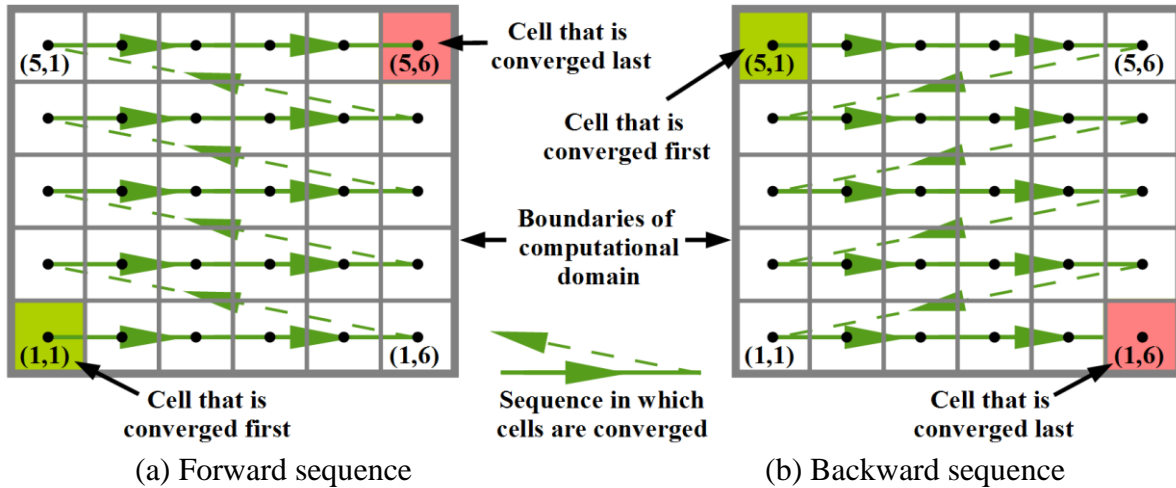


Figure 2.4: Two iteration sequences that can be used during a Gauss-Seidel solution of the computational domain

Since an upwind differencing scheme is used to solve the model, it is necessary that T_w , G_w , i_{ma} and ω are given for the first row to be solved (albeit the top or the bottom row). If these properties are not known, they must be guessed. After the entire domain has been solved, the guess may be improved and the model solved again.

The choice between using the forward- or backward sequence depends on whether it is preferred to guess T_w , G_w , i_{ma} and ω at the top or bottom of the computational domain. When the air flow has an upward vertical component, it is better to guess T_w and G_w at the bottom, where i_{ma} and ω are known, and to use the forward sequence. However, if the air flow has either a downward vertical component ($\alpha < 0$) or is in crossflow ($\alpha = 0$), the backward sequence may be used without having to guess T_w , G_w , i_{ma} or ω at all. This eliminates one iterative loop and allows for much faster simulations.

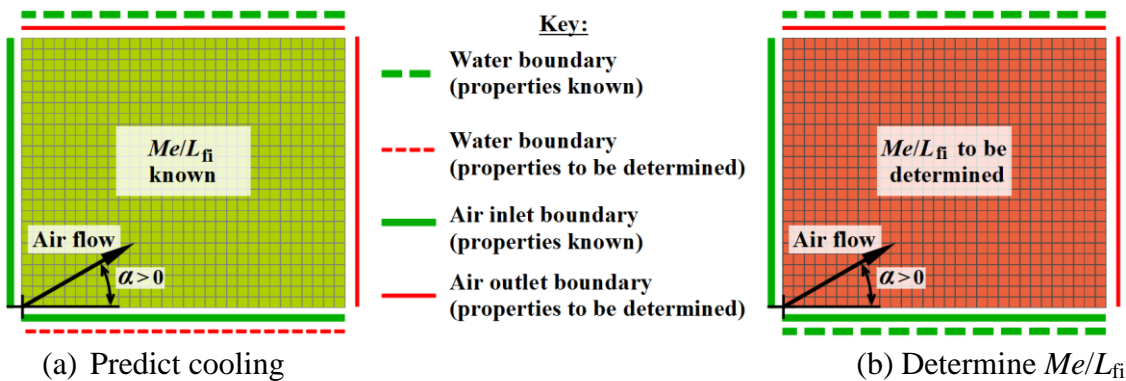


Figure 2.5: Illustration of the two purposes for which the fill simulation program is used

The present fill simulation program may be used for one of two purposes, which are illustrated in Figure 2.5.

- Predict cooling (Figure 2.5 (a)): Predict the outlet conditions (i.e. the cooling) if the inlet conditions and the Me/L_{fi} are known.
- Determine Me/L_{fi} (Figure 2.5 (b)): Determine the Me/L_{fi} of the fill if the inlet and outlet conditions are known, as would be the case when using experimental data to determine fill performance characteristics.

There are thus four different ways in which the fill simulation program may be run, these are shown in Table 2.1.

Table 2.1: Four ways in which the present fill simulation program may be run

Predict cooling + Forward sequence	Determine Me/L_{fi} + Forward sequence
Predict cooling + Backward sequence	Determine Me/L_{fi} + Backward sequence

In Figure 2.6 it the procedure used in each of these cases is illustrated.

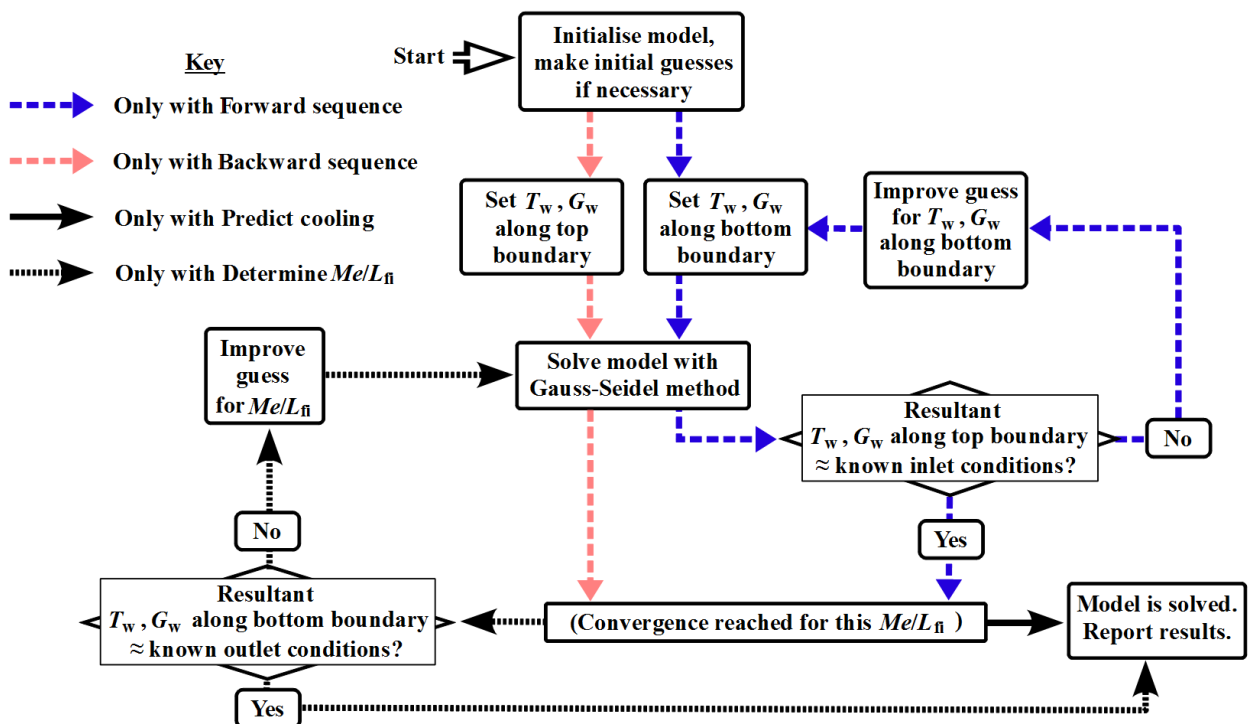


Figure 2.6: Flow diagram of the different ways in which the present fill simulation program solves the Reuter model

The most computationally expensive method of solving the model is when the forward sequence is used to solve for Me/L_{fi} . In such a case, the procedure consists of an initialization phase and then 2 nested iterative loops:

- > Me/L_{fi} is solved iteratively.
- >> For each Me/L_{fi} that is tried, the distribution of water temperature and water mass velocity at the outlet is solved iteratively.

Note that for each of the iterative loops, an iteration limit applies, even though this is not shown on Figure 2.6.

The simplest way to solve the Reuter model is when $\alpha \leq 0^\circ$ and the backward method is used to predict cooling. This way no iterative loop is required.

2.2.7. Methods to increase the solution speed of the model in a computer program

The Reuter model is implemented into a fill simulation program written in Python 2.7 and FORTRAN 95. These two languages complement each other: Python is a high level language and its comprehensive standard library, powerful extensions, dynamic type system and automatic memory management makes it easy to program in and suitable to create and display quality graphics such as graphs. FORTRAN, a low level language known for its high speed in numerical computation, is used to handle the majority of the program's numerical solution.

Since a considerable amount of experimental data had to be processed using the program, methods to increase the model's solution speed were investigated. The results of the investigation are reported for the benefit of future researchers who want to implement the Reuter model into a computer program.

The program was initially written only in Python. In this most basic form, the program takes 4902 seconds (1.4 hours) to solve the example case (presented in Section 2.2.8) using the forward iteration sequence on a given computer. However, the program may instead be set to use the backward iteration sequence, which is appropriate (only) for crossflow, and thereby the solution time is reduced to 1035 seconds (17 minutes).

The program may also be set to import tables (that were created at an earlier stage) on which T_a , as a function of i_{ma} , ω and p can be looked up instead of determining T_a iteratively from Eq. (2.10). This further reduces the solution time to 662 seconds (11 minutes).

The most computationally demanding parts of the program are compiled into a FORTRAN library, which may be called by the main program (that is still coded in Python). When the FORTRAN library is also made use of, the solution time is further decreased to 15 seconds.

The combined effect of the various methods to decrease the solution time is therefore a factor 326 ($= 4902 / 15$)

2.2.8. Example case and output of the present fill simulation program

The example case is based on Kröger's (2004) Example 4.3.1, for which the specifics are:

$$\begin{array}{lll} L_{fi,x} = 1.5 \text{ m} & p_{atm} = 101712.27 \text{ Pa} & T_{wi} = 39.67 \text{ }^\circ\text{C} \\ L_{fi,z} = 1.878 \text{ m} & T_{ai} = 9.7 \text{ }^\circ\text{C} & T_{wo} = 27.77 \text{ }^\circ\text{C} \\ L_{fi,y} = 1.5 \text{ m} & T_{wbi} = 8.23 \text{ }^\circ\text{C} & G_w = 1.7773 \text{ kg}\cdot\text{m}^{-1}\cdot\text{s}^{-1} \end{array}$$

The example case is based on Kröger's case because this case is also used by Gudmundsson (2012) and Kloppers (2004) and it is therefore useful for comparison.

However, the example case differs from Kröger's case on two points:

- It is in crossflow (i.e. $\alpha = 0^\circ$), while Kröger's case is in counterflow (but in Section 2.2.9, results for counterflow and cross-counterflow are also shown).
- Kröger specifies $m_a = 4.134 \text{ kg s}^{-1}$, but in the example case an (equivalent) $G_a = 1.8373 \text{ kg m}^{-2} \text{ s}^{-1}$ is specified instead. This is so that G_a may be kept constant when a side-by-side comparison with other air flow angles is done.

The settings that were used in the example case are given in Table 2.2. The same settings are used in other simulations in this study, unless otherwise stated.

Table 2.2: Setting used for example case in the present fill simulation program

Iteration sequence	Backward
Cell size ($\Delta x, \Delta z$)	(19, 19) mm
Tolerated deviation in ΔT_w	0.001 °C
Cell residual targets: for T_w	0.001 °C
for G_w	0.0001 $\text{kg.m}^{-1}.\text{s}^{-1}$
for i_{ma}	4 J/kg
for ω	$8 \times 10^{-7} \text{ kg/kg}$
Iteration limit when converging a cell (min, max)	(2, 50)
Relaxation factor when updating cell properties	0.8
Tolerated deviation when iteratively solving of T_a from i_{ma}, ω and p	0.05 % ⁽¹⁾

⁽¹⁾ Calculated as
$$deviation = \frac{i_{ma}(T_{a, \text{guessed}}, \omega_{\text{known}}, p) - i_{ma, \text{known}}}{i_{ma, \text{known}}} \times 100\%$$

where the 'known' quantities are the ones determined by Eqs. (2.22) to (2.32).

The present fill simulation program is used to determine the Me/L_{fi} of the example case, and the output is shown in Figures 2.7 and 2.8.

After Me was iterated 5 times, the obtained ΔT_w was within 0.0004 °C of the specified ΔT_w	
Determined	$Me/L_{fi} = 0.42392 \text{ m}^{-1}$ (Total $Me = 0.79612$)
	$EB = 0.66 \%$ (positive means $Q_a > Q_w$)
(Avg) outlet Air:	$T_{ao, \text{right}} = 24.75 \text{ °C}$
	$\phi_{o, \text{right}} = 108 \%$

Figure 2.7: Summary of present fill simulation program output for the example case

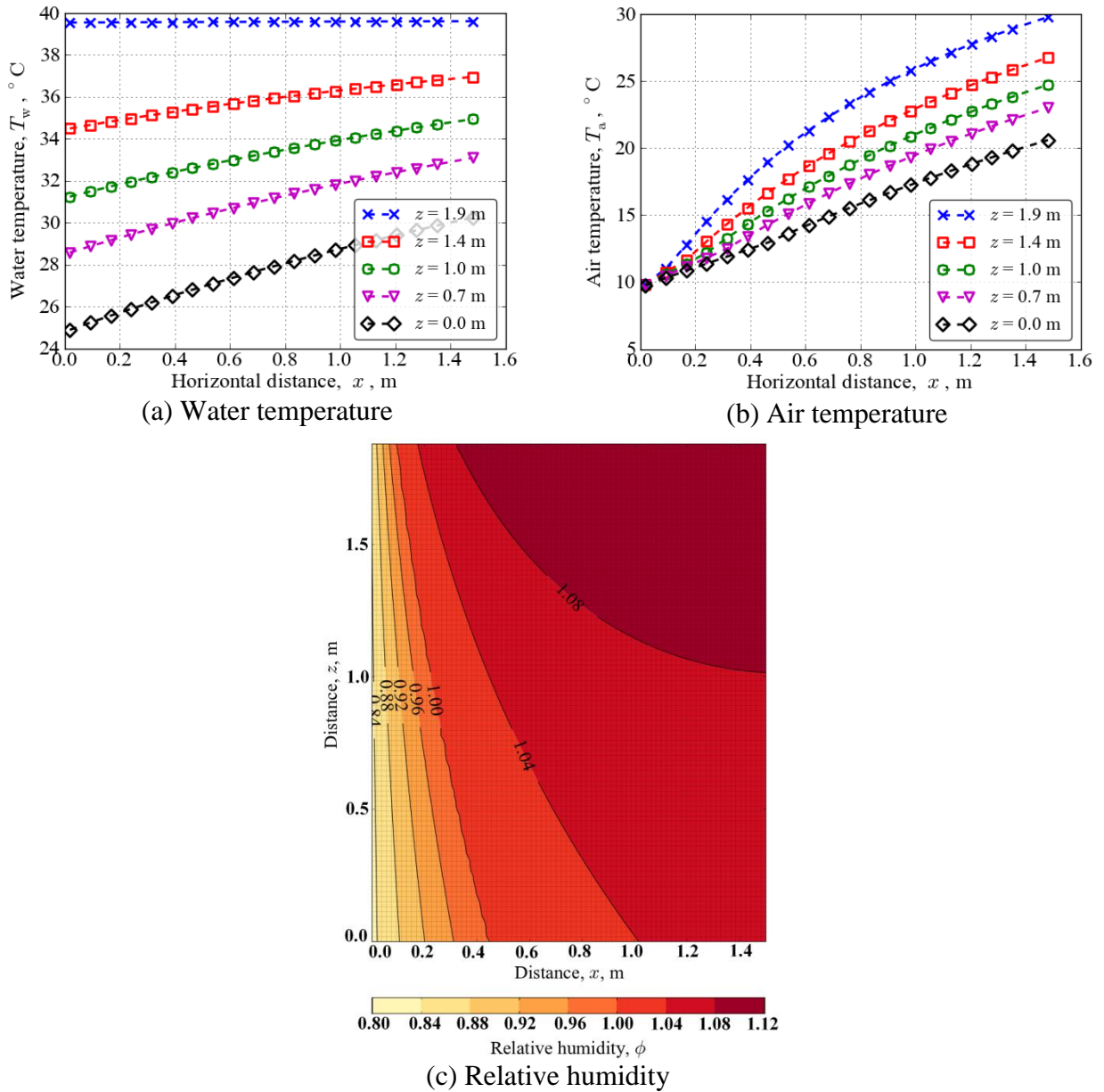


Figure 2.8: Graphical output of the simulation of the example case using the present fill simulation program, showing air and water properties throughout the computational domain

Gudmundsson (2012) provides a sample calculation for the Reuter model in cross-counterflow, which may be referenced as an additional example case.

2.2.9. Grid dependence and other dependencies

The effects of the cell size and the choice of iteration scheme (forward vs. backward) on simulation results are investigated simultaneously using the example case from Section 2.2.8 and the results are given in Table 2.3 and shown in Figure 2.9.

Table 2.3: Comparison between grid dependence for crossflow using the forward or backward sequence

Grid size ($x \times z$)	Cell size (mm)	Backward			Forward		
		Me/L_{fi} (m^{-1})	EB (%)	$\Delta^{(1)}$ (%)	Me/L_{fi} (m^{-1})	EB (%)	$\Delta^{(1)}$ (%)
5 x 5	300 x 376	0.36660	4.55	-13.99	0.35975	7.53	-15.59
10 x 10	150 x 188	0.40464	3.19	-5.06	0.40198	6.00	-5.68
20 x 25	75 x 75	0.42044	1.59	-1.35	0.41975	2.97	-1.52
40 x 50	38 x 38	0.42280	0.96	-0.80	0.42267	1.70	-0.83
80 x 100	19 x 19	0.42392	0.66	-0.54	0.42413	1.06	-0.49
160 x 200	9.3 x 9.3	0.42593	0.74	-0.07	0.42516	0.80	-0.25
320 x 400 ⁽²⁾	4.7 x 4.7 ⁽²⁾	0.42628	0.68	0.02	0.42482	0.47	-0.33

⁽¹⁾ $\Delta = 100 \% \times [Me/L_{fi} - (Me/L_{fi})_{ref}] / (Me/L_{fi})_{ref}$ where $(Me/L_{fi})_{ref} = 0.42621$, which is the Me/L_{fi} at an infinitely small cell size, according to Roache's (1997) method of grid refinement.

⁽²⁾ For the (4.7 x 4.7) cell size, the tolerated deviation in ΔT_w was increased to 0.002 °C.

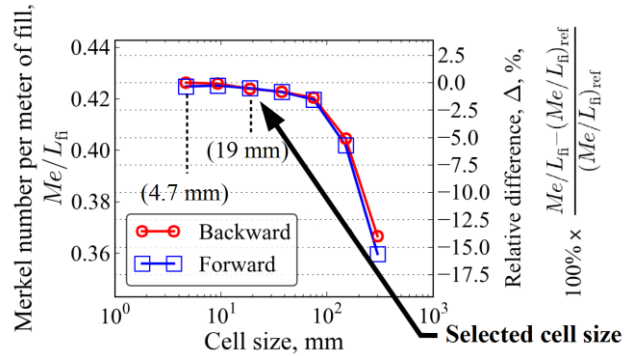


Figure 2.9: Absolute (Abs.) Me/L_{fi} as a function of cell size, shown with its relative difference (Rel.) to a reference Me/L_{fi} for the backward and forward iteration sequences

(Corresponds with data in Table 2.3)

From Figure 2.9, it can be seen that there is almost no difference in result between when the forward or backward iterations sequences are used. Roache's (1997) method of grid refinement is applied to the data for the two smallest cell sizes in the backward iteration sequence to determine the Me/L_{fi} for an infinitely small cell size as 0.42621. Table 2.3 shows that the Me/L_{fi} determined using a cell size of 19 x 19 mm is always within 0.6% of this value (0.42621) and 19 x 19 mm is therefore accepted as a sufficiently small cell size throughout the rest of this study.

The grid dependence for the different types of relative flow (simulated using the forward sequence) is shown in Figure 2.10.

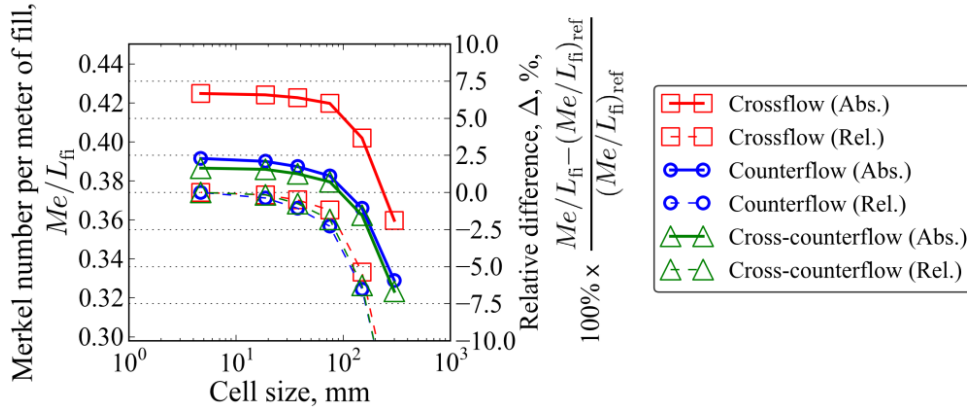


Figure 2.10: Me/L_{fi} (absolute) as a function of cell size, shown with its relative difference⁽¹⁾ to a reference Me/L_{fi} for different types of relative flow

⁽¹⁾ $\Delta = 100 \% \times [Me/L_{fi} - (Me/L_{fi})_{ref}] / (Me/L_{fi})_{ref}$, where $(Me/L_{fi})_{ref}$ is the Me/L_{fi} for an infinitely small cell size, calculated using Roache's (1997) method of grid refinement on the data for that specific type of relative flow.

From the relative plots in Figure 2.10, it is clear that the grid dependence of the present simulation program does not vary significantly for the various types of relative flow.

2.2.10. Verification of present fill simulation program results

In order to verify that the Reuter model was correctly implemented into the computer program, results are checked against those published by Gudmundsson (2012) and Reuter (2010)

1. Gudmundsson (2012)

Gudmundsson implemented the Reuter model into a computer simulation program written in SciLab. A comparison to results from his program, shown in Table 2.4, shows excellent agreement.

Table 2.4: Comparison between results from present fill simulation program and Gudmundsson's (2012) program

Case	Me/L_{fi} (m^{-1})		Δ ⁽³⁾ (%)
	GRO ⁽¹⁾	GUD ⁽²⁾	
⁽⁴⁾ Kröger (2004) Example 4.3.1, crossflow	0.42413	0.42377	0.08
⁽⁵⁾ Kröger (2004) Example 4.3.1, counterflow	0.39002	0.39131	-0.33
⁽⁶⁾ Kröger (2004) Example 4.3.1, cross-counterflow	0.38592	0.38679	-0.22
Experimental crossflow test #101002-18	0.81716	0.81860	-0.18

⁽¹⁾ Result from present fill simulation program, ⁽²⁾ Gudmundsson's result,

⁽³⁾ $\Delta = 100 \% \times (GRO - GUD) / GUD$, ⁽⁴⁾ $G_{a,x} = 1.4675 \text{ kg}\cdot\text{m}^{-1}\cdot\text{s}^{-1}$, $G_{a,z} = 0$,

⁽⁵⁾ $G_{a,x} = 0$, $G_{a,z} = 1.8373 \text{ kg}\cdot\text{m}^{-1}\cdot\text{s}^{-1}$, ⁽⁶⁾ $G_{a,x} = 1.1038$, $G_{a,z} = 1.2992 \text{ kg}\cdot\text{m}^{-1}\cdot\text{s}^{-1}$

Figure 2.11 shows that the temperature profiles at the water- and air outlet predicted by the present fill simulation program compare very closely to those

predicted by Gudmundsson for the crossflow case based on Kröger's (2004) Example 4.3.1.

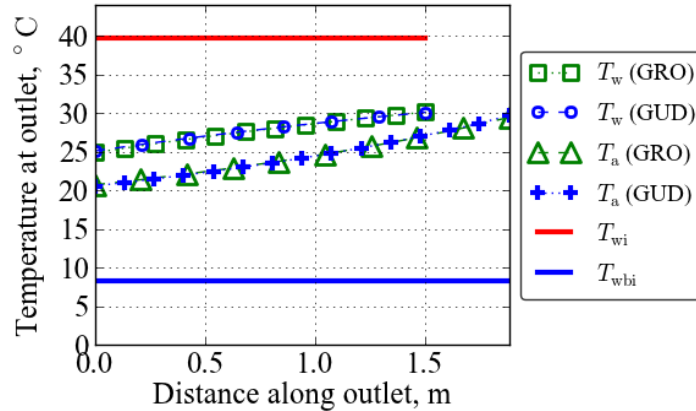


Figure 2.11: Comparison between outlet profiles predicted by the present fill simulation program (GRO) and by Gudmundsson (GUD) for crossflow

2. Reuter (2010)

The present fill simulation program was used to simulate 5 cases that Reuter (2010) simulated using his own numerical implementation of the model. The reference models that are used in the comparative simulations are identical. A comparison between the results, given in Table 2.5, shows excellent agreement.

Table 2.5: Comparison between results from the present fill simulation program and from Reuter (2010)

Air flow angle	$\Delta T_{w, \text{avg}}$ (°C)		$\Delta^{(3)}$ (%)
	GRO ⁽¹⁾	REU ⁽²⁾	
$\alpha = 90^\circ$	1.1814	1.18	0.12
$\alpha = 67.5^\circ$	1.1891	1.18	0.77
$\alpha = 45^\circ$	1.1736	1.17	0.31
$\alpha = 22.5^\circ$	1.1431	1.14	0.27
$\alpha = 0^\circ$	1.0976	1.09	0.70

⁽¹⁾ Results from the present fill simulation program. A cell size of $\Delta x, \Delta z = 0.01, 0.01$ m was used.

⁽²⁾ Results from Reuter (2010). Reuter only provides results to two decimals.

⁽³⁾ $\Delta = 100\% \times (\text{GRO} - \text{REU})/\text{REU}$

The high degree of agreement between results verifies that the model was correctly implemented into the computer program.

2.3. Model of a single drop free falling through an oblique air stream

The motion of a single drop free falling through an oblique air stream, as well as the heat and mass transfer between the drop and the air, can be analytically modeled using correlations found in literature. Such an analytical model is useful because, unlike the other evaporative cooling models that are discussed in this chapter, it does not require experimentally determined transfer characteristics in order to predict cooling. It can therefore be used to model cooling tower rain zones and the results can be compared to that of other models or experimental tests.

Reuter (2010) presents a detailed derivation of such a single drop model, compares various correlations from literature that can be used in it, and recommends some of them. In this study, the model is implemented into a single drop simulation program written in Python 2.7 and used for comparison to experimental results in Chapter 5, where it plays an essential role in understanding the differences between the Reuter model predictions and the experimental results.

In sections 2.3.1 to 2.3.4 the equations that are used in the single drop simulation program are shown and sufficient detail is provided to reproduce a single drop simulation program that gives identical results to the present one. Since no sample calculation for a drop in cross-counterflow was found in literature, such a sample calculation is presented, in detail, in Appendix A.

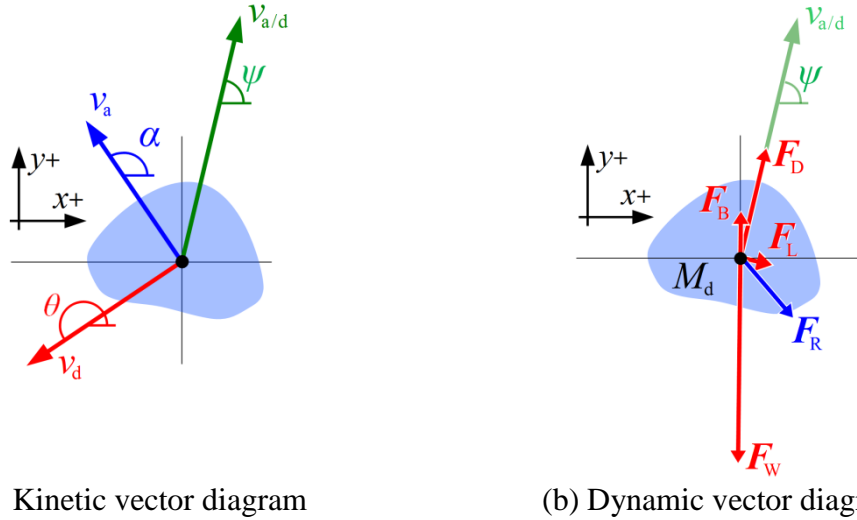
2.3.1. Governing equations for drop motion

The relation between the velocity and force vectors that govern drop motion are respectively given as

$$\vec{v}_{a/d} = \vec{v}_a - \vec{v}_d \quad (2.33)$$

$$\vec{F}_R = \vec{F}_W + \vec{F}_B + \vec{F}_D + \vec{F}_L \quad (2.34)$$

These relationships are illustrated in Figure 2.12.



(a) Kinetic vector diagram

(b) Dynamic vector diagram

Figure 2.12: Vector diagrams of a drop free falling through an oblique air stream

The change in the velocity of the drop may expressed as

$$\frac{d\vec{v}_d}{dt} = \frac{\vec{F}_R}{M_d} \quad (\text{by Newton's 2}^{\text{nd}} \text{ law of motion}) \quad (2.35)$$

\vec{F}_R is determined using the following equations:

$$\vec{F}_W = M_d \vec{g} \quad (2.36)$$

$$\vec{F}_B = -\rho_{av} V_d \vec{g} \quad (2.37)$$

$$\vec{F}_D = C_D \frac{1}{2} \rho_{av} |v_{a/d}|^2 A_{fr} \vec{e}_{a/d} \quad (2.38)$$

$$\vec{F}_L = C_L \frac{1}{2} \rho_{av} |v_{a/d}|^2 A_{fr} \vec{e}'_{a/d} \quad (2.39)$$

The determination of the drag- and lift coefficients (C_D and C_L respectively) is covered in Section 2.3.2.

2.3.2. Drag and lift coefficients for a drop

Dreyer (1994) proposes the following correlation to determine the drag coefficient of a drop that is falling in a gravity field, based on the data from of Gunn and Kinzer (1949):

$$\frac{C_D}{C_{DS}} = 1.0 - 0.17185(1-E) + 6.692(1-E)^2 - 6.605(1-E)^3 \quad (2.40)$$

for $E > 0.4$

$$\text{where } E_T = \frac{1}{1 + 0.148 Eo^{0.85}} \quad \forall Eo > 0 \quad (2.41)$$

$$\text{and } Eo = \frac{(\rho_d - \rho_{av}) |g| d_S^2}{\sigma_d}$$

E is a drop deformation factor determined as

$$E = 1 - \left(\frac{v_{a/d}}{v_T} \right)^2 (1 - E_T) \quad (2.42)$$

where E_T is the drop deformation at terminal velocity

Turton and Levenspiel (1986) provide an appropriate equation to determine C_{DS} :

$$C_{DS} = \frac{24}{Re_S} \left(1 + 0.173 Re_S^{0.657} \right) + \frac{0.413}{1 + 16300 Re_S^{-1.09}} \quad (2.43)$$

where the Reynolds number Re is taken as

$$Re_S = \frac{\rho_{av} v_{a/d} d_S}{\mu_{av}} \quad (2.44)$$

The drop's frontal diameter is considered to be a function E and is expressed as

$$d_{fr} = d_S E^{-1/3} \quad (2.45)$$

The drop's frontal area is then calculated from its frontal diameter as $A_{fr} = \pi d_{fr}^2/4$.

The terminal velocity v_T of drops may be determined using a curve fit to the data from Gunn and Kinzer (1949) or by numerically solving Eq. (2.34) using Dreyer's equations with $E = E_T$ to find the drag coefficient. A comparison between these two methods is shown in Figure 2.13.

The numerical solution of the Dreyer model is preferred for the purposes of this study, because it can be used for drops with a larger diameter than 6 mm and because it keeps model results comparable to those of Reuter (2010), which is the only source against which results from the computer program could be validated.

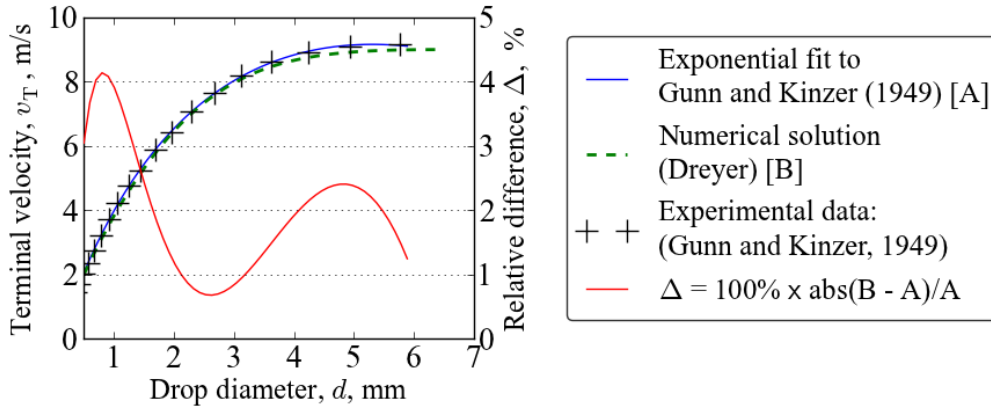


Figure 2.13: Comparison between two methods of predicting drop terminal velocity and experimental data

No literature sources on calculating the lift coefficient of drops were found. Lift on the drop will be zero as long as the drop is axis-symmetric and its axis of symmetry is collinear with $\vec{v}_{a/d}$, but otherwise there will be lift (albeit very small). In the context of cooling towers, this will usually be the case when the drop diameter is larger than 3 mm and either the drop or the air has a significant horizontal velocity component. Drops with a diameter smaller than 3 mm remain close enough to spherical to assume zero lift. It is expected that, even if the lift force does exist, it will be negligibly small compared to the drag force.

Due to the lack of literature on the subject, lift on drops is assumed to be zero. It is recommended that the effect of lift on a drop falling through an oblique air stream be investigated in future research.

Note also that Dreyer's method of calculating drop deformation assumes the drop is falling vertically in a gravity field. The Dreyer model is therefore at best a fair approximation in the case of oblique flow.

2.3.3. Mass change of the drop

The change in drop mass is caused only by evaporation, so

$$\frac{dM_d}{dt} = m_{\text{evap}} \quad (2.46)$$

Mass transfer is calculated using a mass base:

$$m_{\text{evap}} = h_d A_d (\rho_{v,d} - \rho_{v,\infty}) \quad (2.47)$$

Reuter recommends the following combination of correlations in order to determine h_d .

The mass transfer coefficient h_D from the definition of the Sherwood number:

$$h_D = \frac{Sh D}{d_S} \quad (2.48)$$

The diffusion coefficient D from Fuller *et al.* (1966):

$$D = \frac{(1/M_a + 1/M_v)^{0.5} T_a^{1.75}}{\sqrt{2} \left(\sum \Delta_{va}^{0.333} + \sum \Delta_{vb}^{0.333} \right)^2 p_{\text{atm}}} \quad (2.49)$$

$$\text{where } M_a = 28.9583, \quad M_v = 18.013, \quad \sum \Delta_{va} = 19.7, \quad \sum \Delta_{vb} = 13.1$$

The Sherwood number from Ranz and Marshall (1952):

$$Sh = 2 + 0.6 Re^{1/2} Sc^{1/3} \quad (2.50)$$

The Schmidt number Sc is a dimensionless group, and in the case of a drop falling through air, it is defined as

$$Sc = \frac{\mu_{\text{av}}}{\rho_{\text{av}} D} \quad (2.51)$$

In the present fill simulation program, Re , Sh and Sc are evaluated at film conditions when the mass transfer coefficient is calculated.

Film conditions are defined as

$$T_f = \frac{T_a + T_d}{2}, \quad \omega_f = \omega_{\infty}, \quad p_f = p_{\infty}$$

If free-stream (bulk) conditions are used instead of film conditions to evaluate Re , Sh and Sc , it has very small effect on the simulation result.

The relationship between the mass transfer coefficients h_d and h_D may then be found using an equation that Reuter adapted from Incropera and DeWitt (1996):

$$h_d = \frac{h_D p}{R_v (\omega - \omega_{s(T_d)})} \left[\frac{\omega_{s(T_d)}}{(\omega_{s(T_d)} + 0.622) T_d} + \frac{\omega}{(\omega + 0.622) T_a} \right] \quad (2.52)$$

$$\text{where } \omega_{(T_d)} \text{ is saturated humidity at } T_d \text{ and } p_{\text{atm}} \text{ and } R_v = 461.9151111$$

2.3.4. Calculation of the temperature change of the drop

The convective heat transfer between the drop and the air is calculated as

$$Q_{d-a} = h A_d (T_d - T_a) \quad (2.53)$$

The average convective heat transfer coefficient is obtained through the definition of the Nusselt number:

$$h_{\text{avg}} = Nu_{\text{avg}} \frac{k_{\text{av},f}}{d_s} \quad (2.54)$$

Reuter (2010) recommends the correlation from Ranz and Marshall (1952) to calculate the average Nusselt number:

$$Nu_{\text{avg}} = 2 + 0.6 Re_f^{1/2} Pr_f^{1/3} \quad (2.55)$$

Reuter derives the following equation for temperature change in the drop from an energy balance:

$$\frac{dT_d}{dt} = \frac{-1}{M_d c_v} \left[m_{\text{evap}} i_{\text{fg},d} + h A_d (T_d - T_a) \right] \quad (2.56)$$

2.3.5. Implementation of model into a single drop simulation program

With the initial velocity, temperature and mass of the drop known, the change in these properties over time is calculated using Euler's method to numerically integrate Eqs. (2.35), (2.46) and (2.56) over time. This is done using a computer program written in Python 2.7 from which a sample simulation case and output is shown in Figure 2.14. This example case is based on the same parameters as the sample calculation presented in Appendix A.2.

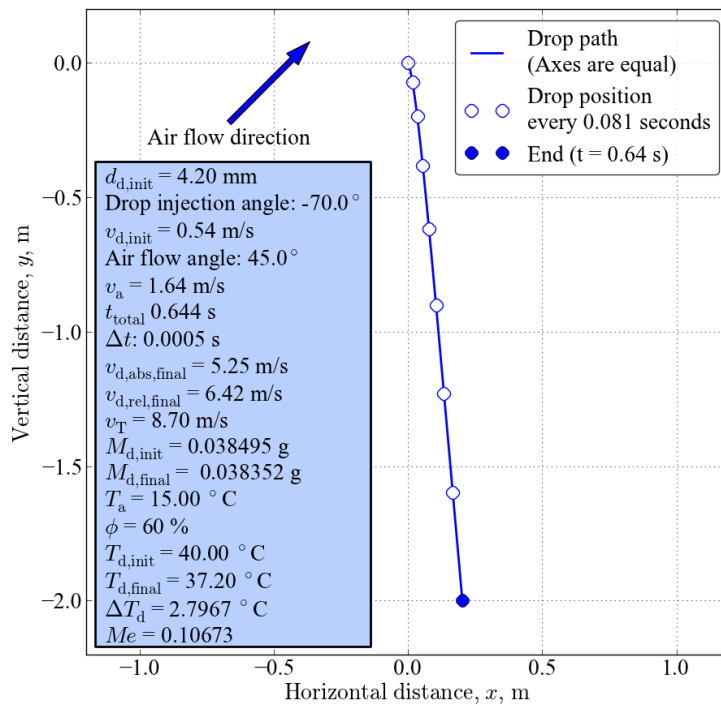


Figure 2.14: Present single drop simulation program results for an example case

2.3.6. Drop Merkel number

The Merkel number is defined as

$$Me = \frac{h_d A}{m_w} \quad (2.57)$$

The “mass flow rate of a single drop” through a domain may be considered to be the drop’s mass divided by the time that it takes the drop to cross the domain.

$$m_d = \frac{M_d}{t_t} = \frac{M_d v_{d,\text{avg}}}{z} = \frac{\pi \rho_d d_d^3 v_{d,\text{avg}}}{6 z} \quad (2.58)$$

The surface area of the drop is simply calculated as the surface area of a sphere ($A_d = \pi d_s^2$).

If an average mass transfer coefficient is known, a mean Merkel number for a single falling drop may be calculated by hand as follows:

$$Me_{avg} = \frac{\pi h_{d,avg} d_s^2 z}{M_d v_{d,avg}} = \frac{6 h_{d,avg} z}{\rho_d d_s v_{d,avg}} \quad (2.59)$$

A marginally more accurate Merkel number may be found when the slight changes in drop mass and surface area are taken into account through numerical integration in a numerical model:

$$Me_{avg} = \Delta t \sum_{i=0}^N \frac{h_{d,i} A_d}{M_{d,i}} \quad (2.60)$$

2.3.7. Validation of single drop simulation program results

A case that is simulated by Reuter (2010) is simulated using the present single drop simulation program and the same reference models as Reuter are used. The results are compared in Table 2.6.

Table 2.6: Comparison of single drop model results to results from Reuter (2010)

α	Me [REU ⁽¹⁾]	Me [GRO]	Δ ⁽²⁾
90.0 °	0.04549	0.04496	-1.2%
67.5 °	0.04509	0.04443	-1.5%
45.0 °	0.04394	0.04336	-1.3%
22.5 °	0.04233	0.04176	-1.3%
0.0 °	0.04058	0.03999	-1.5%
-45.0 °	0.03761	0.03699	-1.6%
-90.0 °	0.03647	0.03576	-1.9%

⁽¹⁾ Results from Reuter (2010), ⁽²⁾ $\Delta = 100\% \times (\text{GRO} - \text{REU})/\text{REU}$

The reason for the average difference of 1.5% between the two result sets remains unclear at this point, but it may be because of different temperatures chosen for the evaluation of thermophysical properties or the value of diffusion coefficient as given by Eq (2.49). However, the single drop model is used for a very specific purpose in this project, which is to determine the variation of Me/L_{fi} over the test section height within a rain zone (see Section 5.2) so that a better comparison can be made between the Reuter model prediction and the experimental results. The impact of a constant 1.5% deviation in Me will not have a significant impact on the comparative results.

2.4. Comparison between model predictions made by the Reuter model and the single drop model

A crossflow, counterflow and a cross-counterflow case, all based on rain zone test #100920-12 (see Appendix B) is simulated in both the present implementation of

the Reuter model and in the present single drop simulation program that is presented in Section 2.3.

G_a has the same magnitude is used in all the three cases and in the single drop simulation, the drop is assumed to always travel at terminal velocity. The single drop simulation is used to determine a Me/L_{fi} . This Me/L_{fi} is then used to predict the cooling with the fill simulation program, and the outlet water temperature determined in this way is compared to the final drop temperature determined by the single drop model.

In order to make a fair comparison, the single drop simulation must use a T_{wb} equal to the average T_{wb} between the outlet and inlet in the fill simulation program. An iterative procedure is therefore necessary to determine $T_{wb,avg}$: The single drop simulation is used to determine a Me/L_{fi} using some $T_{wb,avg}$, which is initially guessed as the T_{wbi} from the experimental test. The Me/L_{fi} determined through the single drop simulation is then used in the fill simulation, which (always) uses the air inlet conditions from the experimental test. The air outlet condition determined by the fill simulation program is then used to calculate a new $T_{wb,avg}$, which is then used in the single drop simulation to recalculate Me/L_{fi} . This procedure is repeated until Me/L_{fi} and $T_{wb,avg}$ converge.

The compared results are shown in Table 2.7.

Table 2.7: Comparison between results from present fill- and single drop simulation programs

Air flow angle	Me/L_{fi}	$T_{wb,avg}$	$\Delta T_{w,avg}$ ($^{\circ}C$)		$\Delta^{(3)}$ (%)
			GRO ⁽¹⁾	SD ⁽²⁾	
$\alpha = 90^{\circ}$	0.03465	11.93	2.202	2.241	-1.75
$\alpha = 45^{\circ}$	0.03179	12.13	2.040	2.058	-0.89
$\alpha = 0^{\circ}$	0.02590	11.22	1.692	1.725	-1.89

⁽¹⁾ Results from the present model implementation. A cell size of $\Delta x, \Delta z = 0.01, 0.01$ m was used.

⁽²⁾ Results from present single drop simulation program

⁽³⁾ $\Delta = 100\% \times (GRO - SD)/SD$

A difference between the simulation results are expected since they employ entirely different models, yet it is encouraging to see in Table 2.7 that the difference between their result is consistently smaller than 2%.

3. EXPERIMENTAL APPARATUS AND METHODOLOGY

3.1. Overview of test facilities and experimental procedures

The combined crossflow and counterflow experimental fill test facilities at Stellenbosch University are shown schematically in Figure 3.1.

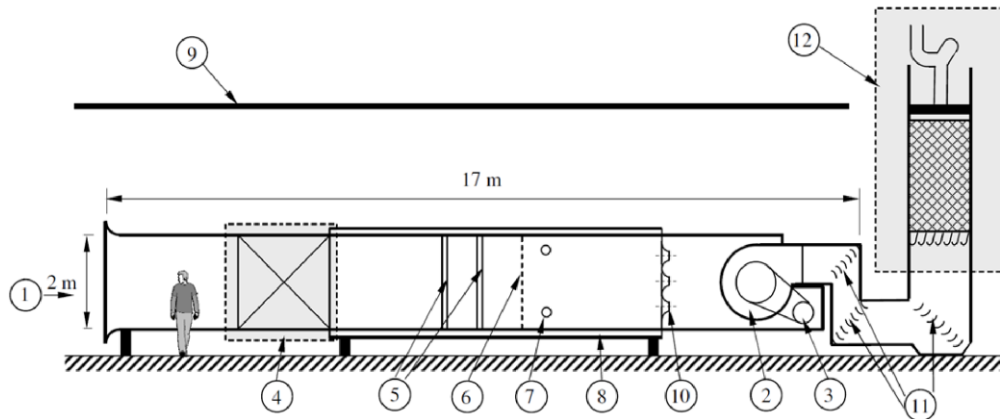


Figure 3.1: Diagram of the fill test facility the Stellenbosch University
(Adapted from Bertrand 2011)

The facility is designed based on the standards laid out in CTI (2000).

Air is drawn into a 2 m x 2 m wind tunnel inlet (1) by a centrifugal fan (2). The fan is driven by a 50 kW electric motor (3), which is connected to a variable speed drive allowing for controllable air speed through the tunnel. After entering the tunnel, the air flows through the crossflow fill test section (4) and then through mixing vanes (5) and a settling screen (6).

Four pairs of thermocouples in aspirated psychrometers (7) measure the dry- and wetbulb air temperatures downstream of the settling screen. Insulation with a 100 mm thickness (8) and a roof (9) shield the facility from convection and solar radiation heat transfer to ensure accurate temperature measurements.

The air then flows through ASHRAE 51-75 (1975) elliptical nozzles located in a nozzle plate (10). The pressure drop measured over these nozzles is used to calculate the air-vapor mass flow rate, m_{av} , through the wind tunnel. Turning vanes (11) guide the air around 90° bends into the counterflow fill test section (12).

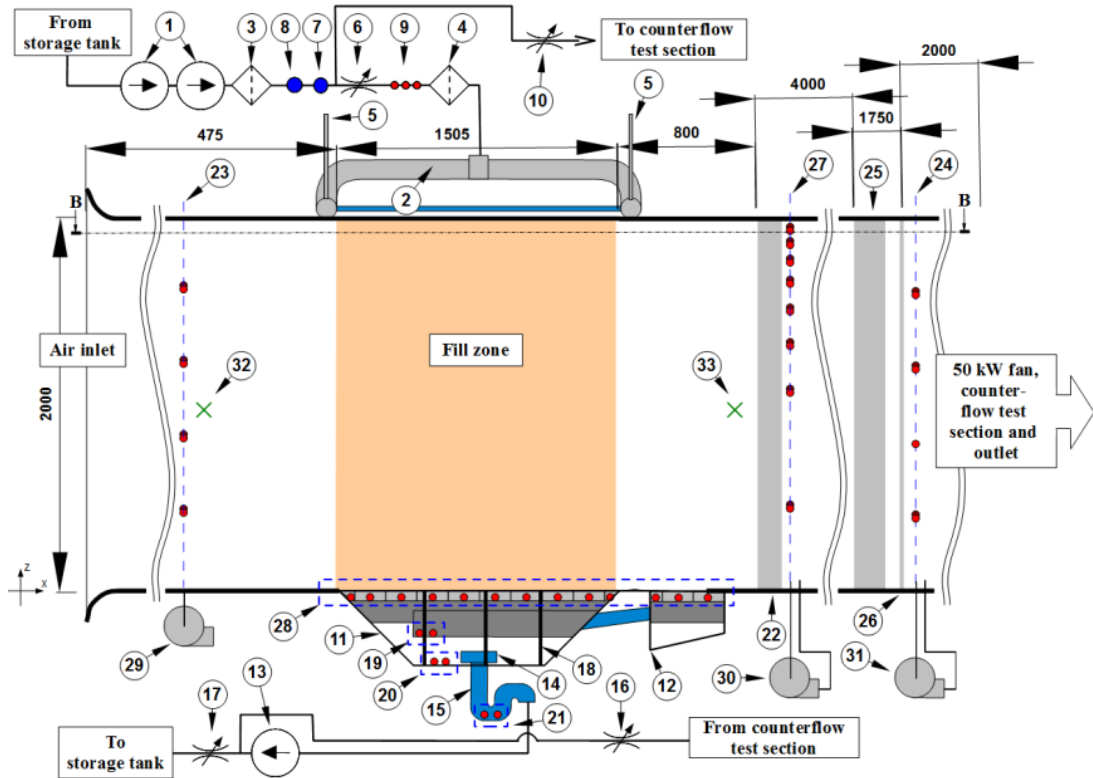
The water that is used during a test is stored in an underground storage tank with a capacity of 45 m³. Before a test, the water is heated to the desired temperature (usually about 50 °C) by circulating it through a 100 kW diesel-fired boiler.

More detail of the respective test facilities is provided in Sections 3.1.1 and 3.1.2.

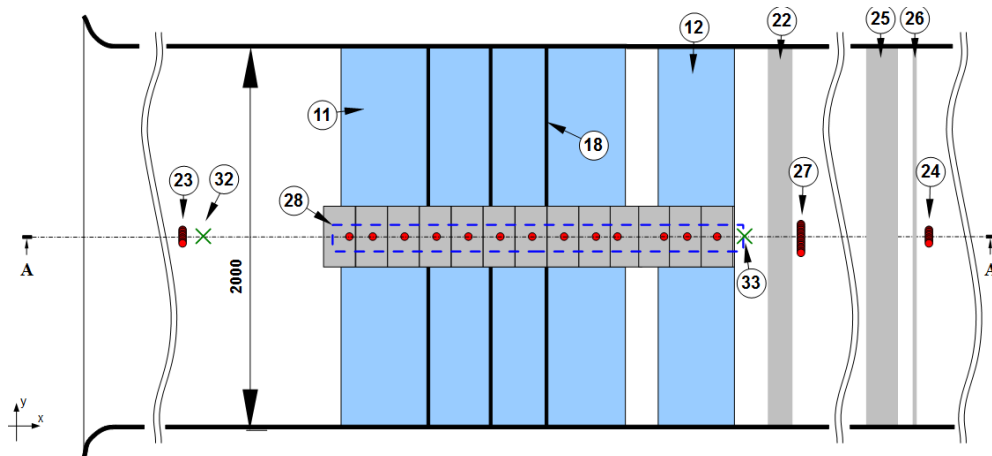
3.1.1. Crossflow test facility

The crossflow test facility is shown schematically in Figure 3.2.

Two supply pumps (1) pump hot water from the underground storage tank to the crossflow test facility, where it is distributed evenly over the fill zone by a water distribution spray frame (2). On its way to the test facility, the water passes through a strainer (3) and a cartridge filter (4). Any air that may have entered the water supply line escapes through bleed valves (5) on the water distribution spray frame. Any air that may have entered the water supply line escapes through bleed valves (5) on the water distribution spray frame.



(a) Side view (section A-A)



(b) Top view (section B-B)

Figure 3.2: Diagram (side view and top view) of the crossflow test facility

In the water supply line, the water flow rate is controlled using a valve (6) and measured using an electromagnetic flow meter (7). This measurement is verified by measuring the pressure drop across an orifice plate (8) installed in the supply line. The water inlet temperature is measured by three thermocouples (9) just before the water enters the water distribution spray frame.

Immediately upstream of the control valve at (6), there is a T-junction through which water flow can be diverted to the counterflow section instead of the crossflow section by closing valve (6) and opening valve (10).

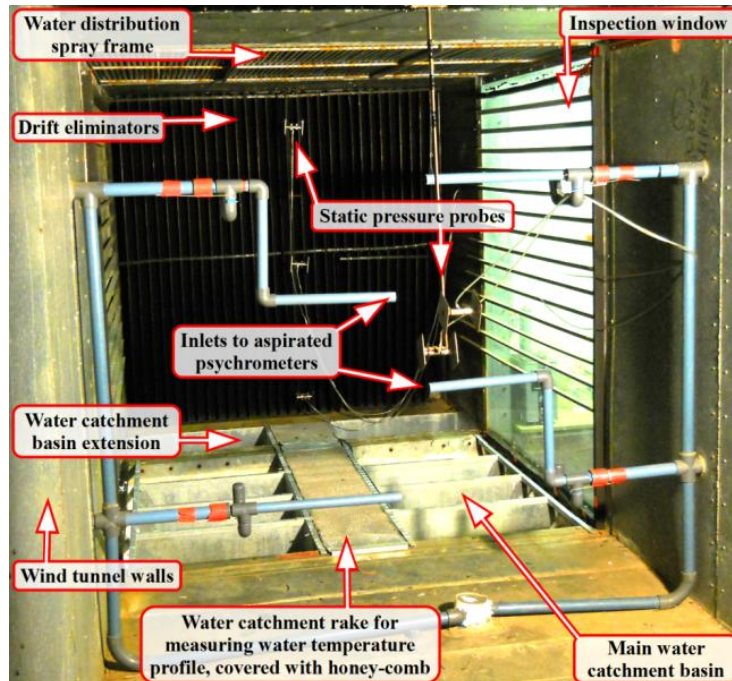


Figure 3.3: Photo of the empty fill zone in the crossflow test facility

After the water has passed through the fill zone, it is collected in the two water catchment basins (11 and 12). A pump (13) drains the collected water through a strainer (14) and outlet pipe (15) and pumps it back to the storage tank. A pipe joins with the crossflow outlet pipe at a T-junction immediately downstream of the drain pump (13). This pipe is the counterflow outlet pipe and it may be sealed by a closing a valve (16). The crossflow test facility's return water flow rate is controlled by a valve (17). Vertical plates (18) impede circumventive air flow through the main water catchment basin, forcing the air to pass through the fill zone instead.

The water outlet temperature is measured at three stages of mixing: in the mixing duct (19), the primary catchment basin (20) and in a u-tube in the outlet pipe (21). Each of these stage temperatures is measured by a set of two thermocouples.

Drift eliminators (22) are installed immediately downwind of the fill zone to reduce the drift losses.

The air dry bulb and wet bulb temperatures at both the inlet and outlet are measured by aspirated psychrometer stations (23 and 24 respectively). Such a station is visible on the foreground of Figure 3.3. Before reaching the outlet station, the air passes through air-mixing vanes (25) and a settling screen (26).

It is known that the air at the outlet is (almost) always super saturated. However, since the degree of super saturation is not measured, the air at the outlet is assumed to be saturated, this assumption is validated by measuring both the drybulb and wetbulb temperatures.

Sensor rakes are used to measure the temperature profiles in both the outlet air and water. The outlet air rake (27) is also an aspirated psychrometer station consisting of 8 pairs of thermocouples, while the water outlet rake (28) consists of 13 thermocouples. All three the psychrometer stations are aspirated by centrifugal fans that are installed underneath the tunnel (29, 30 and 31).

Pressure probes are fixed in front of (32) and behind (33) the fill zone to measure the pressure drop over the fill. The probes are connected by tubes to a Betz manometer inside the lab. Once test conditions have stabilized, the reading from the manometer is taken and recorded by hand. Atmospheric pressure is read off a mercury barometer.

The 53 thermocouples, the electromagnetic water flow meter and the nozzle- and orifice plate pressure transducers, are all connected to an Agilent data logger, which is in turn connected to a PC through an USB cable. On the PC, LabView software is installed through which the sensors are monitored in real-time. Once test conditions have stabilized, all monitored test data are written and saved to disc. The saved data files are processed using Python 2.7 scripts and MS Excel.

3.1.2. Counterflow test facility

Experimental work in this project is limited to the crossflow test facility. Bertrand (2011) did similar work in the counterflow test facility and his test results are compared to results from this study in order to determine the anisotropic fill performance characteristics of a trickle fill. The experimental equipment and procedures that were used by Bertrand for counterflow tests are similar to the equipment and procedures that are described for crossflow in this study and is described in detail in Bertrand (2010).

3.2. Measurement techniques and instrumentation

This subsection discusses specifically measurement techniques. More detail about the accuracy and calibration of the various sensors is given in Section 3.6 while additional details about the location of the individual sensors are provided in Appendix C.

3.2.1. General temperature measurement

In the crossflow test facility, temperatures are measured with T-type thermocouples. In order to increase the confidence level of the measurements, all temperatures are measured with 2 or more thermocouples (except for the 13 temperatures in the profile at the water outlet). The amount of thermocouples used to measure the various temperatures are shown in Table 3.6 in Section 3.5.2.

3.2.2. Dry- and wetbulb temperature measurement with aspirated psychrometers

Air dry- and wetbulb temperatures are measured using aspirated psychrometers according to the standard of CTI (2000). As illustrated in Figure 3.4, both the dry- and wetbulb thermocouples are mounted inside a pipe.

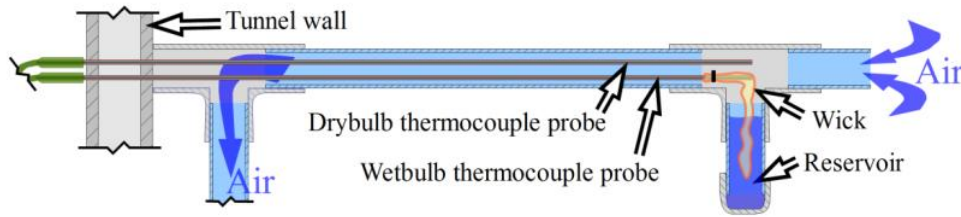


Figure 3.4: Configuration of an aspirated psychrometer station

The thermocouple that is used to measure wetbulb temperature has a wick pulled snugly over the end of its probe. This wick hangs into a small water reservoir that is built into the pipe and in this way it is ensured that the tip of the thermocouple is always in contact with the wet wick. A blower fan, installed below the tunnel, sucks air from inside the tunnel in through the pipe. As the air flows over the wet wick, water evaporates from the wet wick cooling it down to wetbulb temperature, which the thermocouple measures.

The aspirated psychrometers are visible on the photos shown in Figures 3.3 and 3.5.

3.2.3. Temperature profile measurement with rakes

In the crossflow test facility, rakes are used to measure the temperature profiles in both the outlet air and the outlet water.

The outlet air rake, shown in Figure 3.5, is located downwind of the fill zone, immediately behind the drift eliminator, as is illustrated in Figure 3.2 (a) and (b). It consists of 8 aspirated psychrometers with their inlets arranged in a straight vertical line in the center of the tunnel. The outlet air rake was upgraded to the present 8 sensors during this study. (Previously, it consisted of only 4).

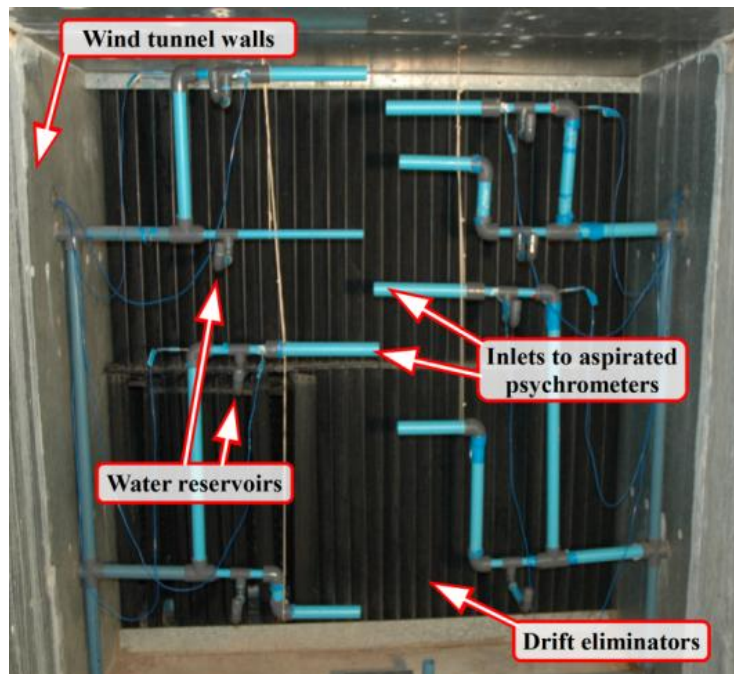


Figure 3.5: Sensor rake at air outlet

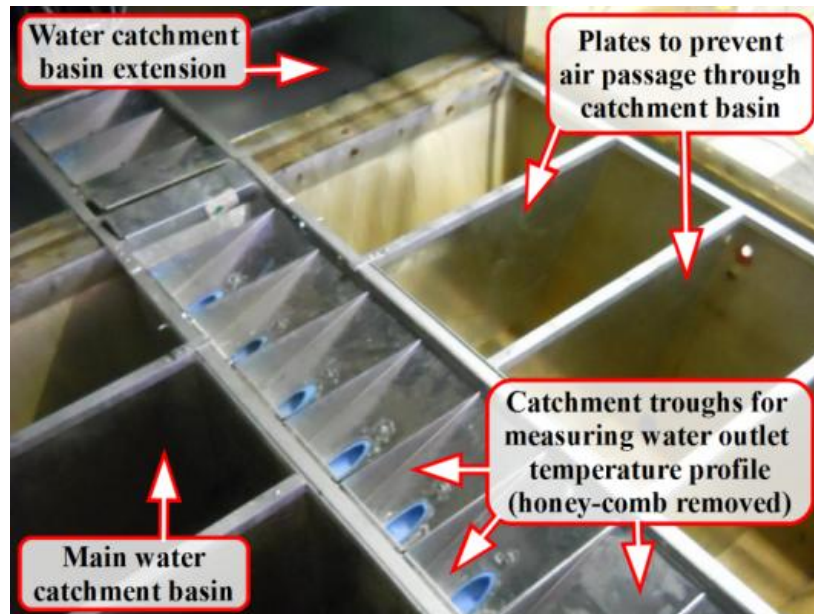


Figure 3.6: Sensor rake at water outlet

The outlet water rake, shown in Figure 3.6, consists of 13 evenly spaced water catchment troughs. Each of the troughs capture water within a rectangular area of 180 x 300 mm. Figure 3.7 shows how thermocouples are installed in (1) the pipes that drain the catchment troughs to measure the water temperature in every trough. The water drained from the troughs flows into the top mixing duct, directly beneath the troughs.

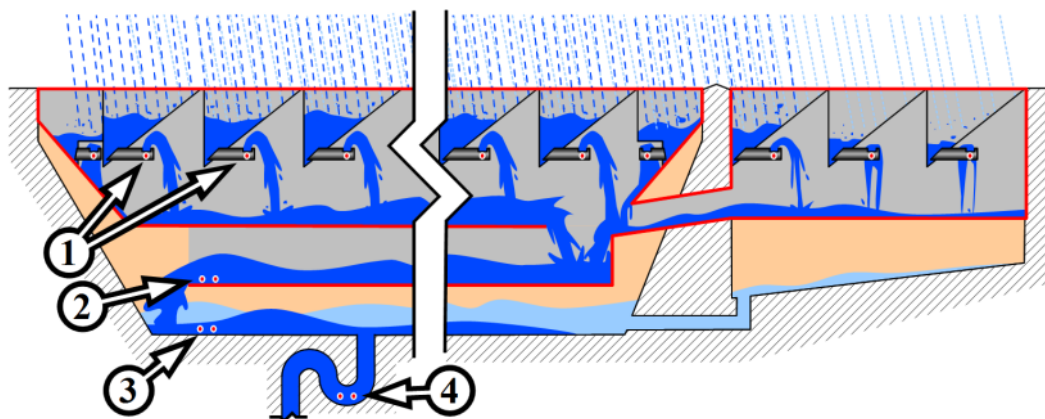


Figure 3.7: Locations where water outlet temperatures are measured

From the top mixing duct, the water flows to the bottom mixing duct and its mixed temperature (2) is measured just before it falls into the main water catchment basin. Additionally, the temperature of the mixed water in the main water catchment basin (3) and in a u-tube (4) in the drain pipe is measured.

The catchment troughs are covered with honey-comb material so that water (moving in a vertical direction) is not impeded, while air (moving in a horizontal direction) cannot easily come into contact with the water in the catchment troughs.

All of the equipment that is presently used to measure water outlet temperatures were designed, manufactured and installed as part of this project.

3.2.4. Mass flow rate measurement

The mass flow rates are calculated using measured volume flow rates and densities that are determined by measured temperatures and pressures.

The electromagnetic flow meter that is used to measure the water's volume flow rate, is shown in Figure 3.8. To verify its reading, the volume flow rate is calculated by measuring the pressure drop across an orifice plate (shown in Figure 3.9) installed in the supply line according to British Standard 1042 (British Standard, 1981).



Figure 3.8: Photo of electromagnetic flow meter installed in water supply line



(a) Orifice plate in water supply line

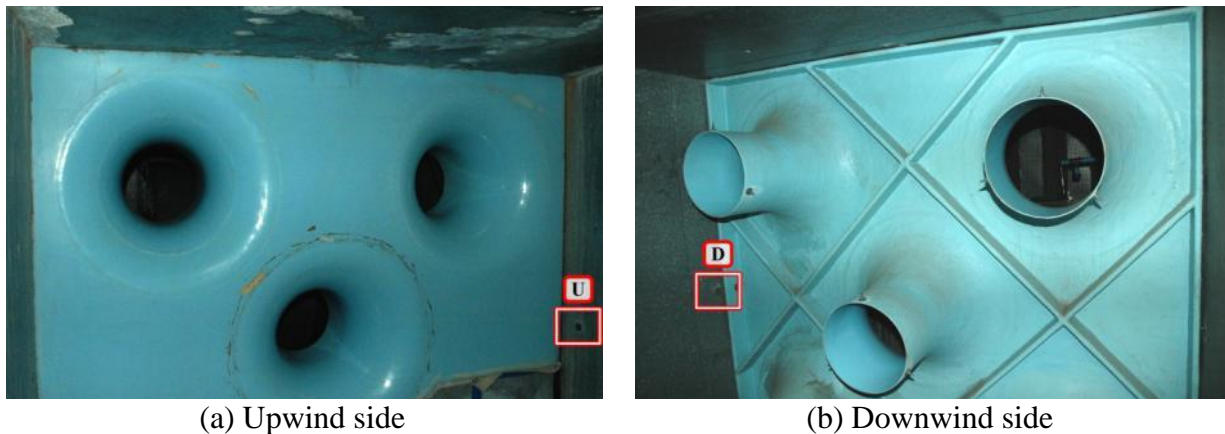


(b) Pressure transducers

Figure 3.9: Photos of orifice plate installed in water supply line and the pressure transducers to which it is connected

The volume flow rate of the air is determined by measuring the average static pressure difference across three ASHRAE 51-75 elliptical nozzles that are installed in the wind tunnel, as shown in Figure 3.10. There are three static pressure tapping points (one on each wall and one in the roof) on each side of the nozzles. Such a tapping point is visible on both Figure 3.10 (a) and (b), and is indicated by U and D on the respective figures. A close-up photo of a pressure tapping point is shown in Figure 3.10. The tubes attached to the three upwind pressure taps are connected to one another and so are the three tubes connected to the downwind taps. These two “combined” tubes are then connected to a calibrated electronic pressure transducer, shown in Figure 3.11 (b).

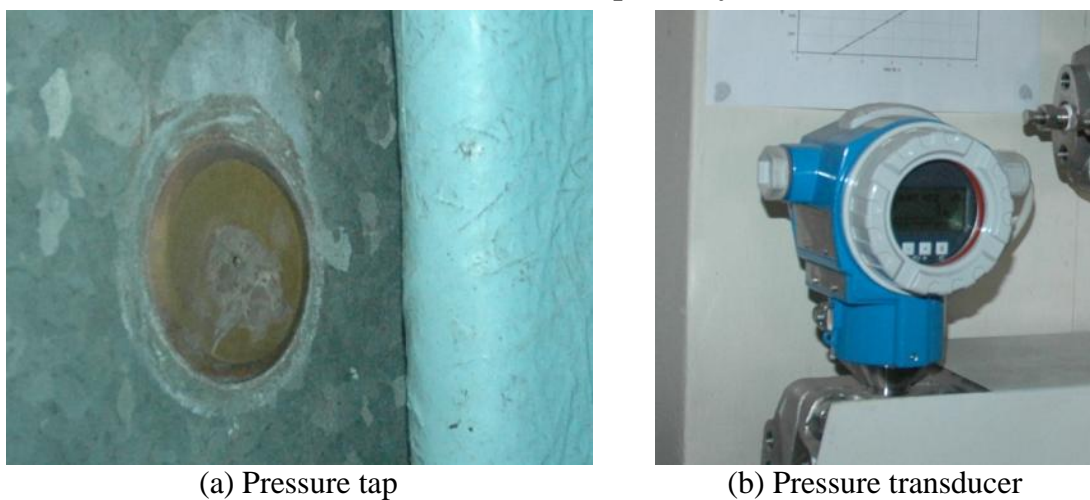
The procedure to calculate the volume flow rate from the pressure drop over the nozzles is described in Section 3.5.2 and a sample calculation is provided in Appendix A.3.



(a) Upwind side

(b) Downwind side

Figure 3.10: Nozzles for measuring air mass flow rate, seen from the upwind side and the downwind side respectively



(a) Pressure tap

(b) Pressure transducer

Figure 3.11: One of the pressure taps (U on Figure 3.10 b) that is connected to the pressure transducer that measures the pressure drop over the nozzles

3.2.5. Pressure measurement

To measure the fill pressure drop, static pressure probes are fixed upwind and downwind of the fill zone as indicated on Figure 3.2 and Figure 3.3. The probes are connected by tubes to a Betz manometer (shown in Figure 3.12) inside the lab. Once a test has stabilized, the reading from the manometer is taken by hand.

Once per test series, atmospheric pressure is read from a mercury barometer.

3.3. Drop size distribution in the crossflow test facility

The drop size distribution by the water distribution spray frame in the crossflow test facility was measured by Banda (2008) using a photographic measuring technique developed by Terblanche (2007). Banda (2008) states that drop sizes (diameters) of 4.34 mm, 3.72 mm and 4.2 mm are measured 230 mm below the crossflow water distribution system at water flow rates of 1.40 kg/m²s, 2.84 kg/m²s and 4.20 kg/m²s, respectively.

This shows that the drop size is influenced by the water mass velocity and a relative variation of about 17% is observed.

3.4. Data acquisition

3.4.1. Data acquisition system

Data acquisition is controlled from the control room (shown in Figure 3.12) next to the wind tunnel, from where the fill zone can be observed through an inspection window.

The 53 thermocouples, the electromagnetic water flow meter and the nozzle- and orifice plate's pressure transducers, are all connected to an Agilent data logger that reads the voltage or current signals from the sensors. It takes the data logger about 11 seconds to scan all the sensors.

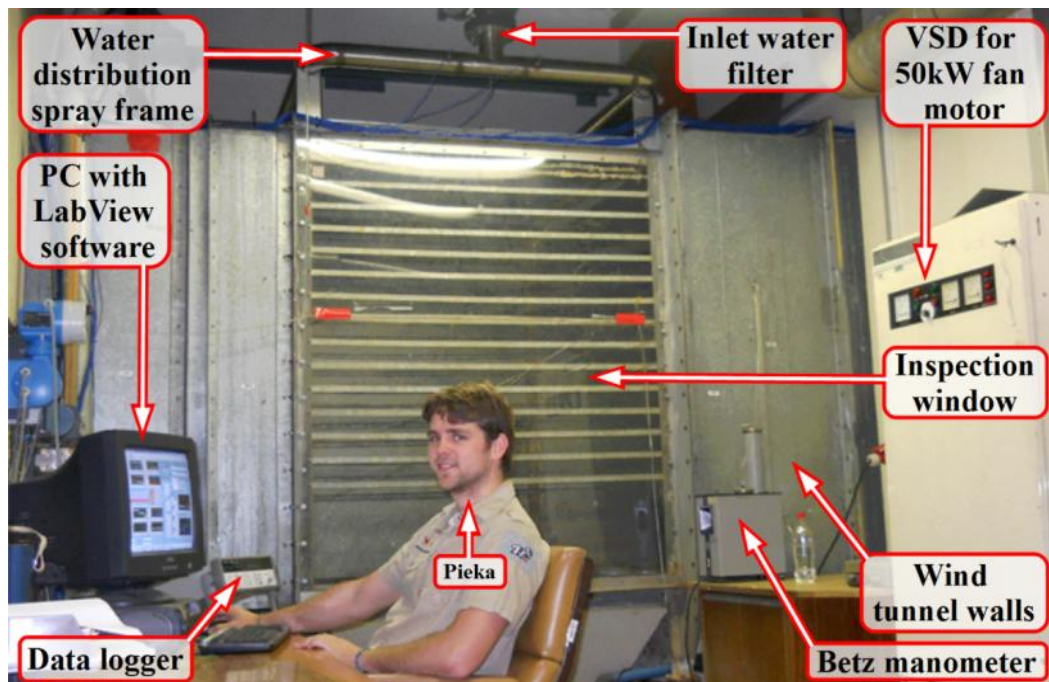


Figure 3.12: The crossflow test facility control room

The data logger, in turn, is connected to a PC through a USB cable. On the PC there is a LabView interface that was programmed for specific use in this test facility. The interface is used to monitor all flow and temperature measurements in real time and to record and write test data to disc as raw data text files. Additionally, the interface shows various graphical displays of measured quantities relative to time and/or relative to one another and it calculates and displays averages for all the measurements. It also calculates and displays Me/L_{fi} and EB . A screenshot of the program's user interface is shown in Figure 3.13.

The atmospheric pressure is read off a mercury barometer once per test series. This atmospheric pressure is typed into the LabView interface and is written to the LabView output file with the rest of the sensor data. Although the atmospheric pressure may change slightly during the course of a test series (typically two

hours), a single reading is acceptable because the energy balance, transfer coefficient and the loss coefficient show very low sensitivity to these small changes in atmospheric pressure.

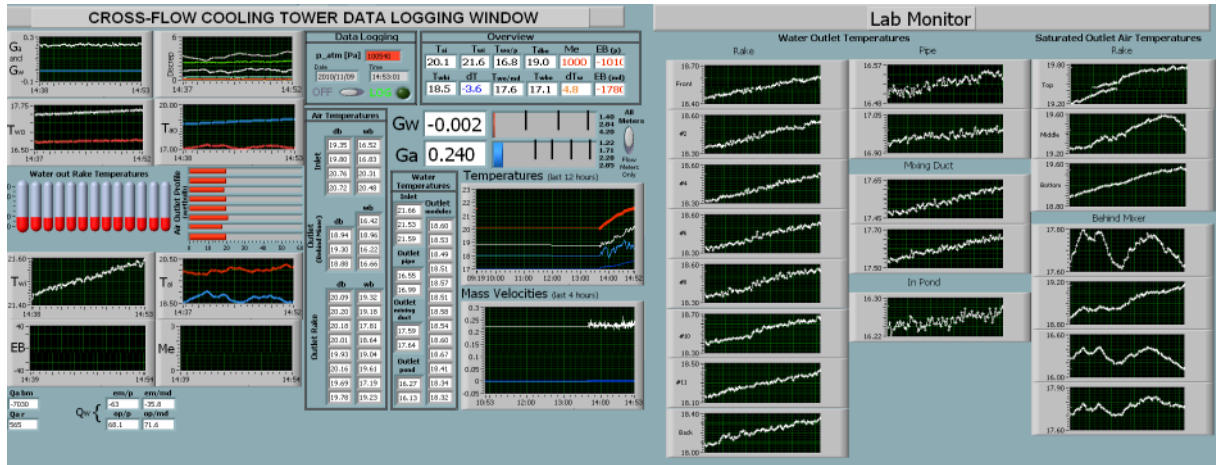


Figure 3.13: Screenshot of LabView monitor program

The fill pressure drop is measured using a Betz water manometer, and the measurement is taken by hand. This is done once per test and the measurement is added to the raw data at a later stage.

3.4.2. Measurement correction during data acquisition

The temperatures that are read from the thermocouples are adjusted using correction factors determined during the procedure that is described in more detail in Section 3.6.2. The correction formula is

$$T_{\text{true}} = c_1 T_{\text{meas}} + c_2 \quad (3.1)$$

where c_1 and c_2 are determined during calibration, although c_1 is equal to one in most cases.

These corrections are applied immediately after the sensors are scanned by LabView and it is the corrected readings that are written to the tab-delimited output file.

3.4.3. Recording and saving of data

The LabView interface enables the continuous monitoring of all sensors, but recording of this data is initiated manually only once the test has stabilized, i.e. when there is minimal change over time in all the measurements. It is unfortunately impossible for a test in this facility to reach complete steady state, because of a continuous but slow decrease in inlet water temperature. This happens because the water is circulated without being re-heated and there are various heat losses along the way.

When the test has stabilized to a satisfactory degree, data recording is initiated. The recording period for a test is roughly a minute, which translates to between 4 and 7 readings from each sensor. During the recording period, the LabView inter-

face writes all recorded data to an output file on the computer's hard drive, which can be read using Microsoft Excel. At the end of the recording period, the writing to the output file ceases.

3.5. Data processing

3.5.1. Statistical analysis of the raw data

During the statistical analysis, the raw data is not modified in any way. The purpose of the analysis is both to evaluate the statistical characteristics of the measurements and to reveal broken sensors, bad outliers or other problems within the data, if any. The analysis is also of interest to the critical evaluation of the test facility (see Section 3.6).

There are three statistical checks that are done on the recorded raw data and these are described below with the aid of the sample of raw data that is provided in Table 3.1.

Table 3.1: Sample raw data set: measurements from the four thermocouples that T_{ai} during a crossflow test

Time [s]	Inlet air drybulb temperature [°C]			
	$T_{ai,1}$	$T_{ai,2}$	$T_{ai,3}$	$T_{ai,4}$
0	17.058533	17.042026	17.073224	17.071317
11	17.058533	17.057912	17.079176	17.088194
22	17.024777	17.020183	17.071239	17.084223
33	17.003928	17.037062	17.066279	17.097128
44	16.985065	17.002312	17.058342	17.087201

1. Maximum time variance

The maximum variance in an individual sensor's readings over the test period is determined. In $T_{ai,1}$ from the sample raw data set, the maximum reading during the test $y_{\max(\text{time})}$ is 17.058533 and the minimum reading during the test $y_{\min(\text{time})}$ is 16.985065.

The maximum test time variance for this sensor is therefore given by

$$\begin{aligned} \text{Max. time variance} &= y_{\max(\text{time})} - y_{\min(\text{time})} \\ &= 0.073468 \end{aligned}$$

The definition of maximum time variance is shown graphically in Figure 3.14.

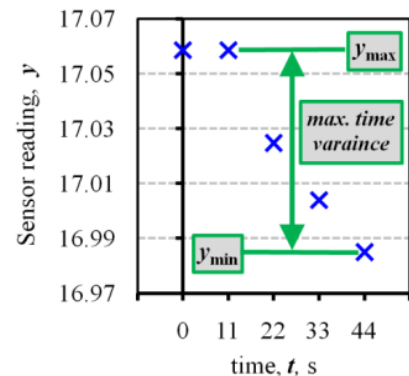


Figure 3.14: Maximum time variance in $T_{ai,1}$ from the sample raw data set

2. Deviation

Measurement deviations are assumed to be around a mean. The mean is considered to be a linear function of time, and mean function is determined by a first order curve fit (least squares) through the measurements to yield the formula.

$$mean(x) = mx + c$$

where x is simply the index of the measurement. In the $T_{ai,1}$ example case, the least squares fit yields $m = -0.0201541$ and $c = 17.0866295$.

The mean value for the second time step in the example case is therefore

$$mean(2) = -0.0201541(2) + 17.0866295 = 17.0463213$$

The deviation from this mean is calculated as

$$deviation(x) = |y(x) - mean(x)|$$

So, in the case of the second time step,

$$\begin{aligned} deviation(2) &= |17.058533 - 17.0463213| \\ &= 0.0122117 \end{aligned}$$

The deviations and mean values for the $T_{ai,1}$ example case are given in and shown graphically in Figure 3.15.

The mean deviation for the $T_{ai,1}$ example case is 0.004885. The maximum deviation 0.0122117.

3. Sensor variance

Sensor variance is checked in cases where multiple sensors are used to measure the same property. This accounts for all the temperature sensors except for those that measure the temperature profile in the outlet water. The water mass flow is also included in this group.

In the example data set in Table 3.1, the maximum sensor value $y_{\max(\text{sensor})}$ in the first time step is that of $T_{ai,3}$, which is 17.073224. The minimum sensor value $y_{\min(\text{sensor})}$ for the first time step is that of $T_{ai,2}$, which is 17.042026.

The sensor variance for the first time step is therefore given by

$$\begin{aligned} sensor\ variance &= y_{\max(\text{sensor})} - y_{\min(\text{sensor})} \\ &= 17.073224 - 17.042026 = 0.031198 \end{aligned}$$

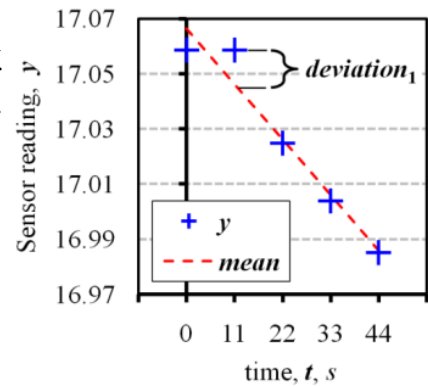


Figure 3.15: Deviation in the example case

Table 3.2: Deviation data for example case

t	y	$mean(x)$	$deviation$
0	17.058533	17.0664754	0.0079424
11	17.058533	17.0463213	0.0122117
22	17.024777	17.0261672	0.0013902
33	17.003928	17.0060131	0.0020851
44	16.985065	16.985859	0.0007940

Summarizing statistical data

The results of the statistical analysis from the sample raw data set are shown in Table 3.3 and Table 3.4.

Table 3.3: Summary of statistical analysis on sample raw data set, Part 1

	$T_{ai,1}$	$T_{ai,2}$	$T_{ai,3}$	$T_{ai,4}$
<i>maximum time variance</i>	0.07346800	0.055600	0.0208340	0.02581100
<i>mean deviation</i>	0.00488468	0.0124704	0.0030952	0.00563872
<i>max deviation</i>	0.01221170	0.0159852	0.0052579	0.00744520

In order to make it possible to inspect the statistical analyses of an entire test series (consisting of 16 tests) in a short time, the statistical data must be condensed. However, There are two statistical aspects of interest that need to be preserved when the results are condensed:

General statistical quality of the data, which is determined by averaging the statistical data.

Severity of outlier data, which is determined through use of maximum() functions.

In Table 3.5, it is shown how all the data in Table 3.3 (a) and (b) is condensed to 6 data points, while conserving the aforementioned statistical information.

To enable the inspection of the statistical results from an entire test series at a glance, a similar approach than before is followed. Averages and maximums are taken, but this time from entire series:

Table 3.4: Summary of statistical analysis on sample raw data set, Part 2

Time [s]	<i>Sensor variance</i>
0	0.031198
11	0.030282
22	0.064040
33	0.093200
44	0.102136

- Avg(avg): the average of the average value of the respective tests in the series.
- max(avg): the worst average value in the entire series
- Avg(max): the average of the worst values of the respective tests in the series.
- max(max): the worst value in the entire test series

Table 3.5: Condensed statistical results for the example T_{ai} sensor set

<i>time variance</i>		<i>deviation</i>		<i>sensor variance</i>	
average	max	mean	max	average	worst
0.043928	0.073468	0.006522	0.015985	0.064171	0.102136

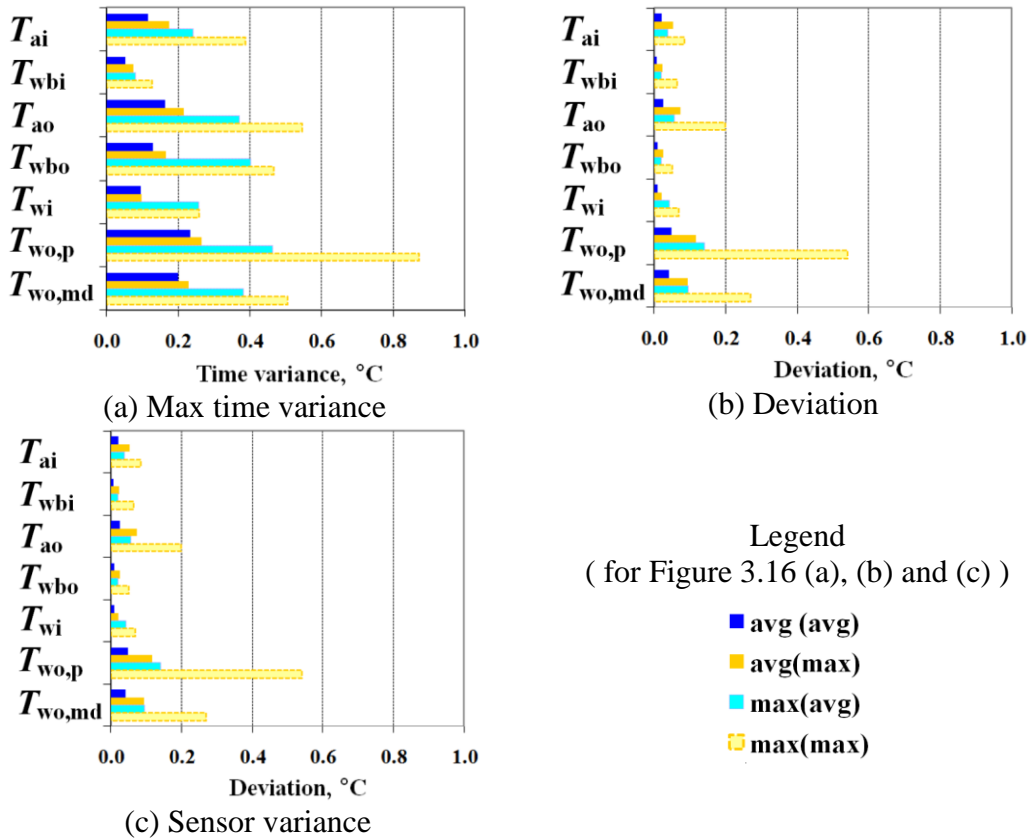


Figure 3.16: Example of summarized results from the statistical analysis of a test series

With the data from a test series condensed in this way, it is displayed on charts such as is shown in Figure 3.16, which enable quick detection of problematic outliers or sensors with poor average performance. These figures and a few other similar ones (shown in Appendix E.2) are the end product of the statistical analysis and makes effective quality control of data possible.

3.5.2. Processing of recorded data

The first step in data processing is to calculate the air-vapor mass flow rate from the pressure drop that is measured over the ASHRAE 51-75 nozzles as described in Section 3.2.4. Kröger (2004) provides equations to convert this measured pressure drop over the nozzles to an air-vapor mass flow rate. Since there is a weak inter-dependence between the outlet air-vapor mass flow rate and the absolute static pressure at the nozzles, an iterative procedure is employed to solve these two unknowns simultaneously. The iterative procedure is shown in Appendix A.3.

After the air-vapor mass flow rate has been determined, the final values for the various measured quantities listed in Table 2.6 are determined by averaging and rounding the raw data. The data is rounded to ensure the measurements, which are reported to a limited amount decimals on tables, yield the reported Me/L_{fi} , K_{fidm}/L_{fi} and EB .

Table 3.6: Amounts of sensors used to measured various properties during a crossflow test

	T_{ai}	T_{wbi}	T_{wi}	T_{wo}	m_{avo}	m_w	Δp_{fi}	T_{wbo}	p_{atm}
Amount of sensors	4	4	3	2	1	2	1	4	1

Two Merkel numbers are calculated from the test data:

Me_{Reuter} is determined using the simulation program and procedure presented in Section 2.2.6.

Me_{e-NTU} is calculated according to the method presented in Kröger (2004: 274). The main equations, which are solved simultaneously, are given below:

$$Me_{e-NTU} = NTU C_{e\min} / m_w \quad (3.2)$$

$$e_e = 1 - \exp\left[NTU^{0.22} \left\{ \exp(-C_e NTU^{0.78} - 1) \right\} / C_e\right] \quad (3.3)$$

$$e_e = Q / Q_{\max} \quad (3.4)$$

$$Q = m_a (i_{mao} - i_{mai}) \quad (3.5)$$

$$Q_{\max} = C_{e\min} (i_{maswi} - \lambda - i_{mai}) \quad (3.6)$$

$$\lambda = (i_{maswo} + i_{maswi} - 2i_{masw}) / 4 \quad (3.7)$$

$$C_{e\min} = \min\left(m_w c_{pw} / \frac{di_{masw}}{dT_w}, m_a\right) \quad (3.8)$$

$$C_{e\max} = \max\left(m_w c_{pw} / \frac{di_{masw}}{dT_w}, m_a\right) \quad (3.9)$$

$$\frac{di_{masw}}{dT_w} \approx \frac{i_{maswi} - i_{maswo}}{T_{wi} - T_{wo}} \quad (3.10)$$

$$C_e = C_{e\min} / C_{e\max} \quad (3.11)$$

where NTU is solved iteratively from Equation (3.3).

K_{fdm}/L_{fi} is calculated using Equation (1.2).

EB is calculated as

$$EB = 100\% \times \frac{(Q_a - Q_w)}{Q_w} \quad (3.12)$$

$$Q_a = m_a (i_{mai} - i_{maso(Twbo,avg)}) \quad (3.13)$$

$$Q_w = m_{wi} c_{pwi}(T_{wi} - 273.15) - m_{wo} c_{pwo(Two,avg)}(T_{wo,avg} - 273.15) \quad (3.14)$$

$$m_{wo} = m_{wi} - m_a (\omega_s(Twbo,avg) - \omega_1) \quad (3.15)$$

where the temperatures in subscripted brackets, e.g. $(Twbo,avg)$, indicate the temperature at which the thermophysical property is evaluated.

In all the equations the thermophysical properties are calculated using the property relations from Kröger (2004). The use of equations (3.2) to (3.12) is demonstrated in a sample calculation in Appendix A.4.

During the processing of the raw data, the temperature profiles at both the air and water outlets and the water outlet temperature at other stages of mixing (see Figure 3.7) are also drawn from the raw data.

Finally, the results from data processing are summarized and put into tables and into graphs where appropriate.

3.6. Critical evaluation of crossflow test facility

3.6.1. Miscellaneous improvements

During the critical evaluation of the crossflow test facility, multiple opportunities for improvement were identified and consequently addressed. Note that the description of the facility that is given in Sections 3.1 and 3.2, is of the facility after improvements had been made. These improvements are briefly described in Appendix D, and are listed below.

- 4 additional aspirated psychrometers were installed to measure the temperature and humidity of the mixed air downwind of the fill zone.
- 3 additional thermocouples were installed so that the temperature of the water at the outlet can be measured at three stages of mixing rather than at just one.
- A section of the tunnel floor immediately downstream of the fill zone was cut away and an additional water catchment basin was designed, manufactured and installed in order to collect and drain water that is dragged along by the air.
- Pressure probes were mounted in the center of the tunnel both upwind and downwind of the fill zone.
- 40 angle irons that were permanently mounted on the insides of the tunnel walls in the fill zone were removed in order to eliminate air gaps between the fill and the tunnel walls during trickle fill tests.
- The warped wooden sheets for impeding flow through the water catchment basin were replaced by galvanized plates.
- The water catchment basins were insulated.
- A strainer was designed, manufactured and installed onto the pipe through which the water catchment basins are drained.

3.6.2. Accuracy of relative temperature measurements

In order to determine how accurately relative temperature differences are measured in the crossflow test facility, all the thermocouples were moved to a central location and put into a water-filled thermos flask with a platinum thermometer, as is illustrated in Figure 3.17. Note that the thermocouples were not disconnected from the data logger at any point during this process.

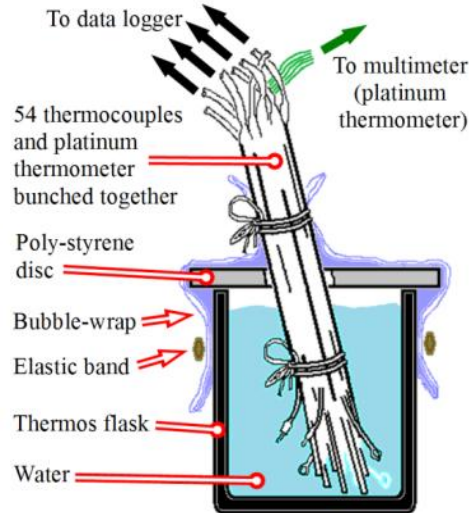
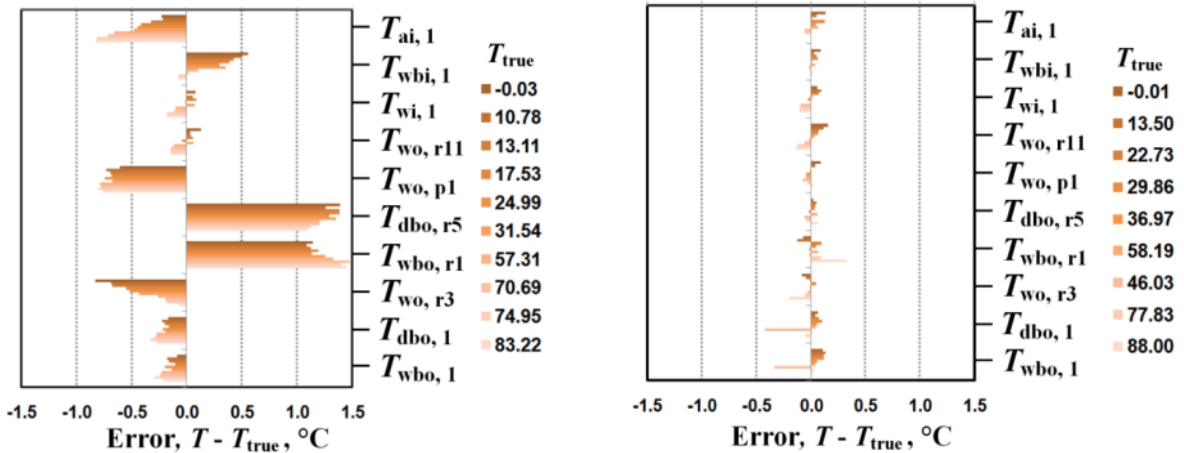


Figure 3.17: Set-up to evaluate accuracy of relative temperature measurements



(a) Before correction factors were determined and applied

(b) After correction factors were determined and applied

Figure 3.18: Difference between T measured by some of the thermocouples and T_{true} before and after correction factors were determined and applied

The temperature measured by the platinum thermocouple was taken as the true temperature T_{true} and the readings from the other 53 thermocouples were compared to this T_{true} at 10 different temperatures. It was determined that the difference in reading could be as high as 1 °C.

Correction factors were consequently determined and are applied using Eq. (3.1) to the respective thermocouples. The difference that the correction factors make can be seen in Figure 3.18. The correction factors themselves are given in Appendix D.

After the correction factors were implemented, the error was measured again at 15 different temperatures (9 of which are shown on Figure 3.18) and from these measurements the average absolute error was determined as 0.0631 °C, and maximum

measured error as 0.4219 °C. These give a good indication of how accurately relative temperatures can be measured in the crossflow test facility.

3.6.3. Uniformity of water distribution

In order to determine the uniformity of the water distribution within the crossflow test facility, the local mass velocity was measured at 130 (13 x 10) points in the test section, using the experimental setup that is shown in Figure 3.19.

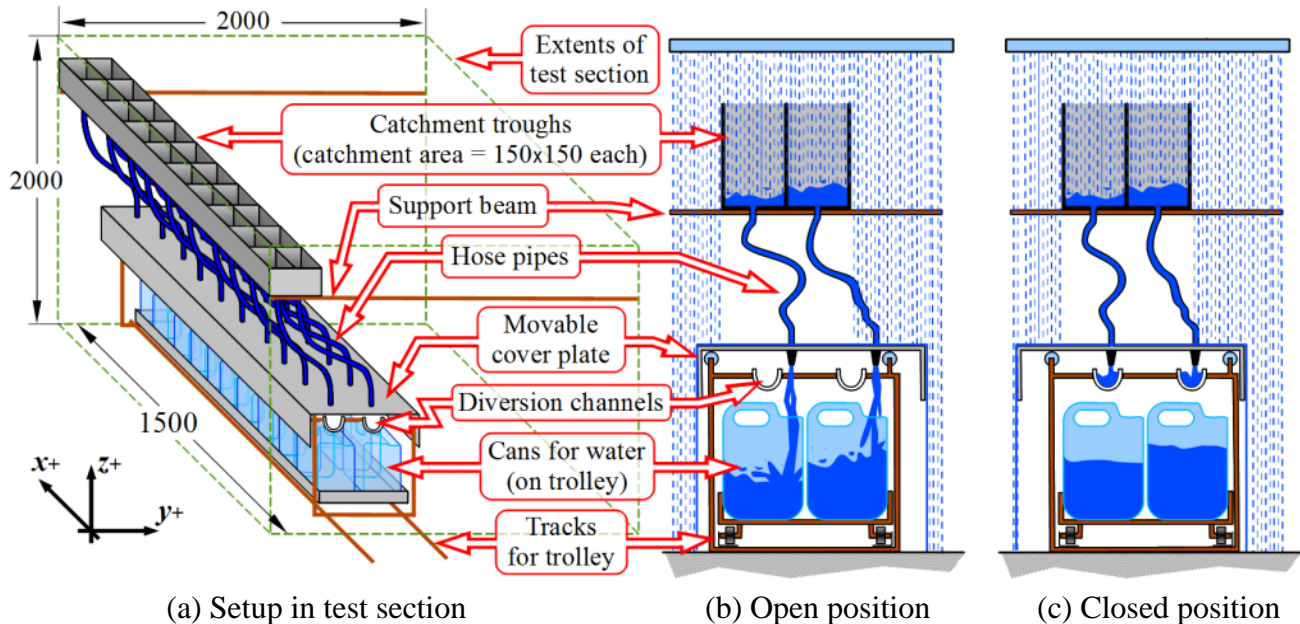


Figure 3.19: Experimental setup to measure uniformity of water distribution in the crossflow test facility

A collection of 20 catchment troughs is suspended about 50 mm below the water distribution spray frame, where it can be moved sideways in order to measure the water distribution of the whole test section. The water that is collected by the catchment troughs can be directed to either the water cans or to the diversion channels by moving the cover plate between the open and closed positions. A stopwatch is used to measure the time that water is flowing into the water cans.

The cover plate is then moved to the closed position and the trolley with the 20 water cans on them is pulled out and the cans are weighed using a scale.

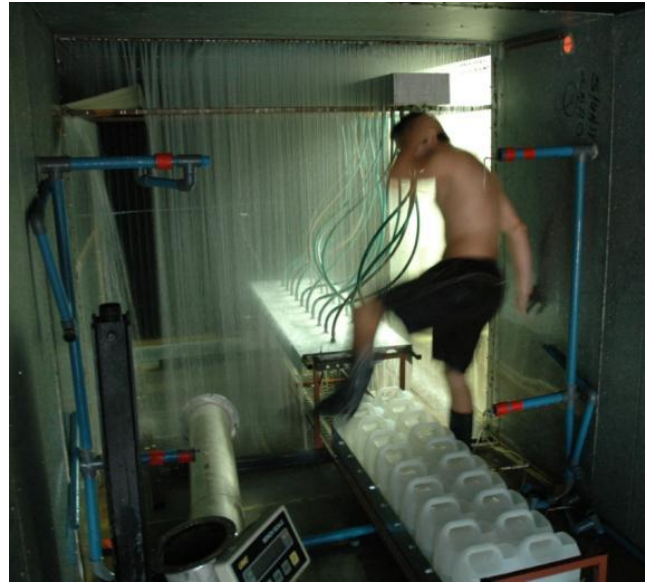
The local mass velocity can then be calculated as

$$G_w(x, y) = \frac{M_{\text{can}}}{t_{\text{stopwatch}} A_{\text{trough}}} \quad (3.16)$$

Distribution tests in progress are shown in Figure 3.20.



(a) With previous equipment

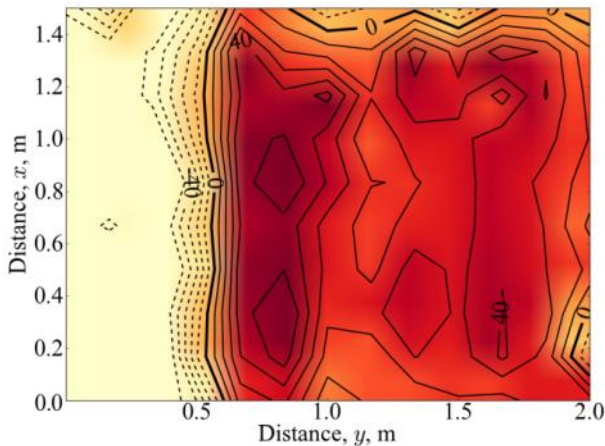


(a) With equipment constructed during this study

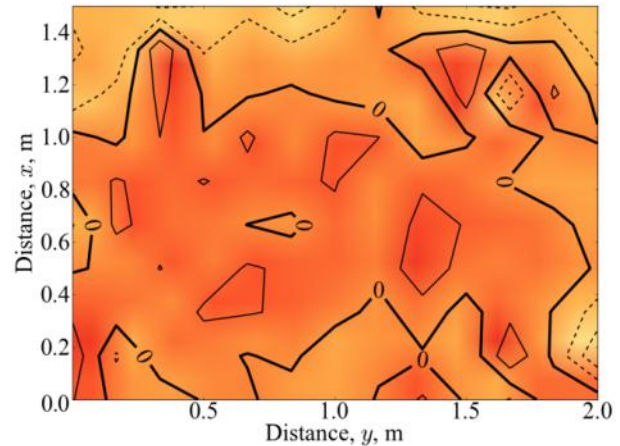
Figure 3.20: Water distribution tests in progress

Three series of water distribution were done in the crossflow test facility:

1. The first test series showed that the water distribution is poor at low flow rates ($G_w < 1.7 \text{ kg}\cdot\text{m}^{-2}\cdot\text{s}^{-1}$) and the spray frame was consequently modified with bleed valves.



(a) Before flow reducers were installed



(b) After flow reducers were installed

(Contours show deviation from average measured G_w , $100\% \times (G_w(x,y) - G_{w,avg}) / G_{w,avg}$, in 10% intervals)

Figure 3.21: Comparison between water distribution at $G_w \approx 1.6 \text{ kg}\cdot\text{m}^{-2}\cdot\text{s}^{-1}$ measured before and after flow reducers were installed in spray frame.

2. Improved equipment for measuring the water distribution was designed and manufactured as part of this project and used for the second (and third) distribution test series. Results from the 2nd test series, shown in Figure 3.21 (a), revealed that the bleed valves did not resolve the water distribution problem.
3. About 130 flow reducers were consequently inserted (in parallel) into the spray frame and the distribution was measured a third time. It was found that the increased overall flow resistance in the water distribution spray frame caused a pressure in the spray frame that was sufficient to obtain a more uniform water distribution at the low flow rates, as is shown in Figure 3.22.

The measurements made during the final series of water distribution tests that are summarized in Table 3.7 show that the standard deviation in the water distribution is consistently about 10%. Contour plots of the test results in Figure 3.22 indicate that there is a lower flow zone at $1.3 < x < 1.55$.

It is believed that the lower flow zone is caused by localized fouling in the spray frame. However, due to time constraints this was not addressed during this project.

Table 3.7: Summarized results from final water distribution tests

$G_{w,\text{mean}}$ $\text{kg m}^{-2} \text{s}^{-1}$	$\sigma^{(1)}$ $\text{kg m}^{-2} \text{s}^{-1}$	$100\% \times \frac{\sigma}{G_{w,\text{mean}}}$
1.61	0.191	11.86
3.28	0.298	9.09
4.91	0.487	9.92
1.58	0.156	9.87

(1) Standard deviation

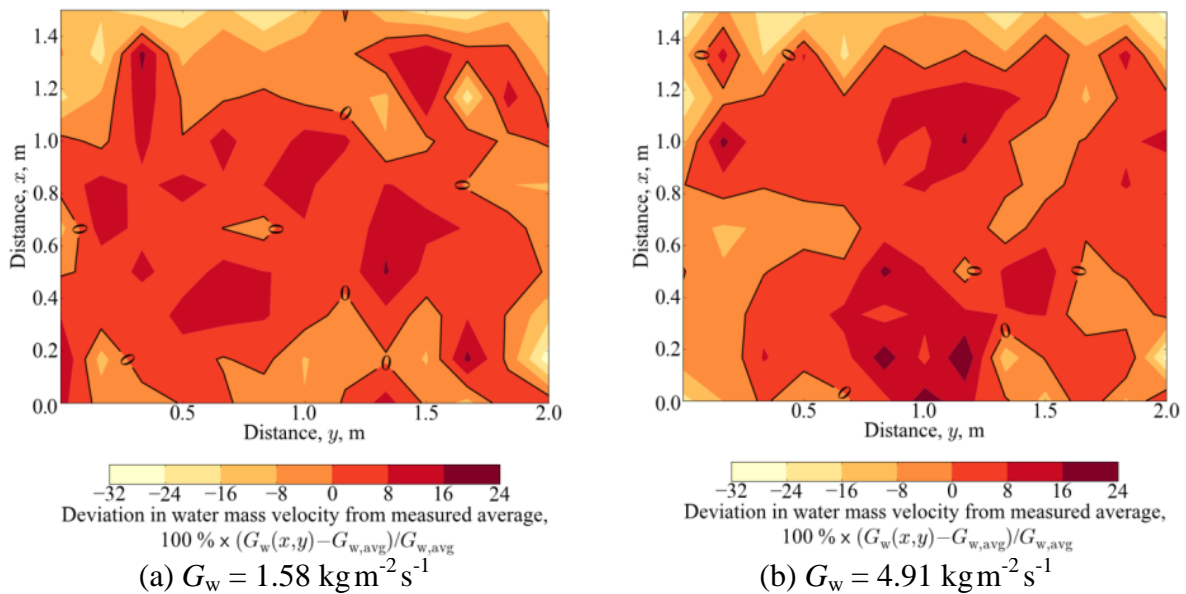


Figure 3.22: Final water distribution measured

3.6.4. Mass flow rate measurements

Duss (2009) critically evaluated the air flow rate measurement of the nozzles in the crossflow test facility by comparing it to air velocity profiles measured with calibrated anemometers. He states that 4.2% is the absolute average uncertainty in the air flow rate measurement.

Both Banda (2008) and Bertrand (2010) performed a calibration on the electromagnetic water flow meter by measuring the time it took to fill up a large tank of known volume at a constant flow rate that is measured by the electromagnetic flow meter. Banda (2008) determined an average and maximum uncertainty as respectively 0.97% and 1.98%, while Bertrand determined it as respectively 0.56% and 0.95%.

3.6.5. Uncertainty in the calculated Me/L_{fi} , K_{fdm}/L_{fi} and EB

An analysis is done to determine the uncertainty of the Me/L_{fi} , K_{fdm}/L_{fi} and EB that are calculated using the measured test data.

Firstly, the measurement uncertainties of the test facility is determined by considering the substantial amount of statistical data generated from the crossflow tests, the measurements made during thermocouple calibration and at the findings of Duss (2009) and Banda (2008). The accuracies that were approximated in this way for the various sensors are given in Table 3.8 as (avg Δ) and (max Δ), which refer to respectively a reasonable average and a worst case accuracy for the applicable sensor.

Secondly, the sensitivity of calculated Me/L_{fi} , K_{fdm}/L_{fi} and EB to these measurement errors is approximated in terms of a *sensitivity gradient*. A sensitivity gradient expresses the relative change (in percentage) in Me/L_{fi} , K_{fdm}/L_{fi} or EB as a function of the error in a given measurement. The unit of this error in measurement is predefined as either [$^{\circ}\text{C}$], [% of mass flow] or [Pa]. Sensitivity gradients can be visualized as the gradients of the lines in Figure 3.23.

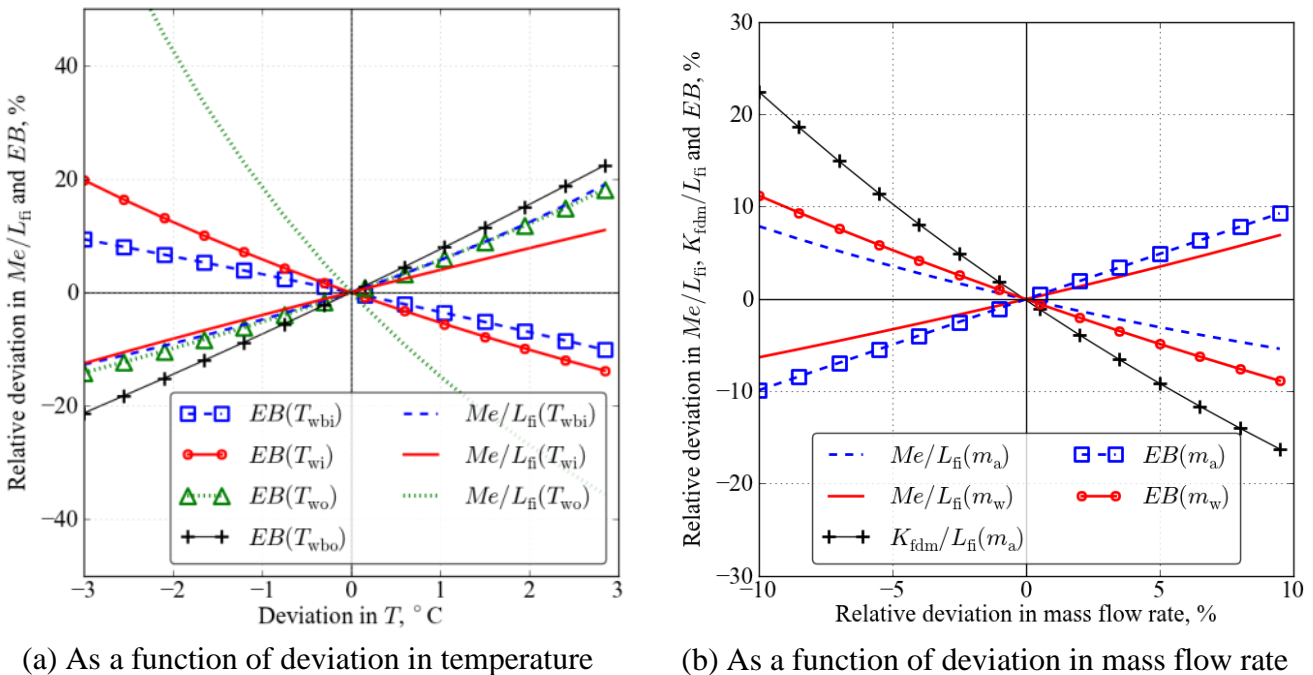


Figure 3.23: Deviations in Me/L_{fi} , K_{fdm}/L_{fi} and EB as a function of deviations in various measurements, as calculated for a specific test case

From Figure 3.23 it is also clear that the sensitivity gradients are not always constant. They also differ from test case to test case. In order to determine a general sensitivity gradient of Me/L_{fi} , K_{fdm}/L_{fi} and EB , average sensitivity gradients are determined.

To demonstrate how these gradients are determined, the procedure to calculate the gradient for Me/L_{fi} with regard to T_{wi} is set out below:

1. The (unmodified) data from a certain experimental test (1 of 16) of a specific⁽¹⁾ test series is used to calculate a reference $(Me/L_{fi})_{Ref}$.

⁽¹⁾The data from the test series with trickle fill, done on 02 October 2011, was used. The data is recorded in Appendix C as tests number #101002-01 to #101002-16.)

2. T_{wi} is set to $[T_{wi,ref} - \Delta T_{wi}]$.
 $Me/L_{fi(Tw\ low)}$ is then calculated from this modified data set.
3. T_{wi} is set to $[T_{wi,ref} + \Delta T_{wi}]$.
 $Me/L_{fi(Tw\ high)}$ is then calculated from this modified data set.
4. $Grad_{Me/L_{fi}}$ for T_{wi} for this test 1 (of 16) is then calculated as

$$Grad_{Me/L_{fi}} = 100\% \times \frac{Me/L_{fi(Tw\ high)} - Me/L_{fi(Tw\ low)}}{2\Delta T_{wi} (Me/L_{fi})_{Ref}} \quad (3.17)$$

5. Steps 1-4 are repeated for experimental tests 2 to 16, and the final $Grad_{Me/L_{fi}}$ is calculated as the average of the gradients determined for the 16 individual tests.

The sensitivity gradients that were calculated in this way for the various measurements are given as $Grad_{Me/L_{fi}}$, $Grad_{K_{fdm}/L_{fi}}$, $Grad_{EB}$ in Table 3.8.

Finally, the approximated measurement uncertainties and sensitivity gradients are used together to estimate the uncertainty of Me/L_{fi} , K_{fdm}/L_{fi} and EB determined from the measured data as follows:

$$\Delta y = Grad_y \Delta x \quad (3.18)$$

Table 3.8: Estimated measurement uncertainty in crossflow test facility and sensitivity gradients of derived Me/L_{fi} , K_{fdm}/L_{fi} and EB

x	T_{wbi}	T_{wi}	T_{wo}	m_{avo}	m_w	Δp_{fi}	T_{wbo}	$SS^{(1)}$
$Grad_{Me/L_{fi}}$	13.4 %/K	16.9 %/K	-47.8 %/K	-1.6 %/%	1.6 %/%	0.0 %/Pa	0.3 %/K	0.0 %/%
$Grad_{K_{fdm}/L_{fi}}$	-0.1 %/K	1.2 %/K	-1.2 %/K	-1.9 %/%	0.1 %/%	2.5 %/Pa	0.0 %/K	-0.0 %/%
$Grad_{EB}$	-3.4 %/K	-7.1 %/K	7.0 %/K	1.0 %/%	-1.0 %/%	0.0 %/Pa	7.6 %/K	0.1 %/%
avg Δx	0.047 K	0.071 K	0.048 K	2.70 %	0.97 %	0.5 Pa	0.104 K	10 %
max Δx	0.280 K	0.167 K	0.164 K	3.22 %	1.98 %	3.5 Pa	0.370 K	20 %
avg $\Delta Me/L_{fi}$	0.6 %	1.2 %	-2.3 %	-4.4 %	1.6 %	0.0 %	0.0 %	0.1 %
max $\Delta Me/L_{fi}$	3.7 %	2.8 %	-7.9 %	-5.3 %	3.2 %	0.0 %	0.1 %	0.1 %
avg $\Delta K_{fdm}/L_{fi}$	0.0 %	0.1 %	-0.1 %	-5.1 %	0.1 %	1.2 %	0.0 %	0.0 %
max $\Delta K_{fdm}/L_{fi}$	0.0 %	0.2 %	-0.2 %	-6.0 %	0.2 %	8.7 %	0.0 %	0.0 %
avg ΔEB	-0.2 %	-0.5 %	0.3 %	2.7 %	-1.0 %	0.0 %	0.8 %	1.1 %
max ΔEB	-0.9 %	-1.2 %	1.2 %	3.2 %	-2.0 %	0.0 %	2.8 %	2.1 %

⁽¹⁾ ss refers to super saturation and the value for Δ is the percentage above 100% saturated.

The influence of the average and maximum inaccuracy of individual sensors on the derived quantities are shown in Table 3.8 and illustrated (as Δy) in Figure 3.24.

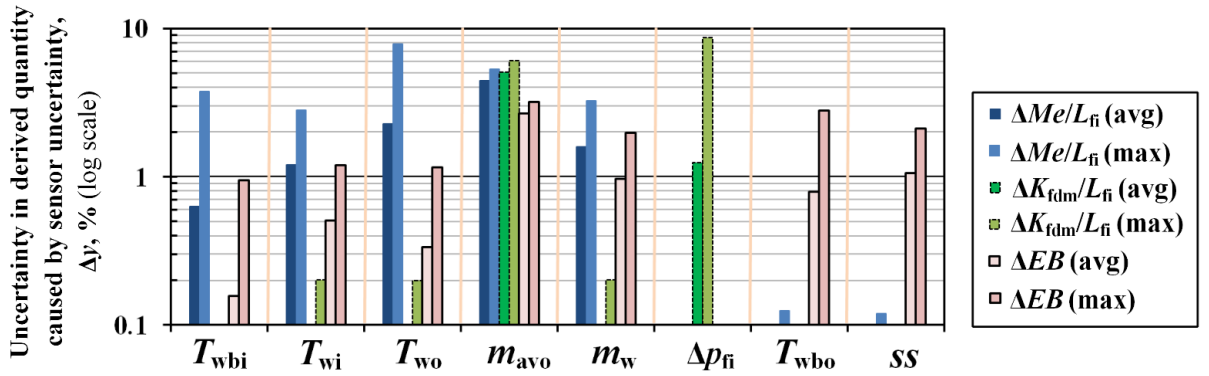


Figure 3.24: Sensitivities of derived quantities to measurement inaccuracies

Note that the influence of the measurement inaccuracies in T_{ai} , T_{ao} and p_{atm} are negligible and therefore omitted from Table 3.8 and Figure 3.24. Although the degree to which the outlet air is super saturated is not measured in the test facility, it is assumed to be 100% saturated in calculations, whilst it is known that it is actually supersaturated. The assumption of 100% saturation may therefore be considered a 'measurement inaccuracy' and therefore it is also shown in Table 3.8 and Figure 3.24.

The (pessimistic) cumulative influence of measurement uncertainties on the derived Me/L_{fi} is calculated as

$$(\Delta Me/L_{fi})_{total} = \sqrt{\sum (Grad_{Me/L_{fi}} \Delta x_i)^2} \quad (3.19)$$

and similar equations are applied for K_{fdm}/L_{fi} and EB .

The cumulative inaccuracies determined in this way are given in Table 3.9:

Table 3.9: Pessimistic estimated accuracy of Me/L_{fi} , K_{fdm}/L_{fi} and EB that are determined from crossflow test data

	$(\Delta Me/L_{fi})_{Total}$	$(\Delta K_{fdm}/L_{fi})_{Total}$	$(\Delta EB)_{Total}$
avg	5.4 %	5.2 %	3.0 %
max	11.1 %	10.6 %	5.0 %

3.7. Experimental tests done

The crossflow test facility was used to perform multiple fill tests in order to determine the difference between crossflow and counterflow fill performance characteristics of a trickle fill. This is discussed in detail in Chapter 4.

4 series of rain zone tests were also done for comparison to model predictions. This comparison is presented in Chapter 5.

The data that was recorded in all the experimental tests are summarized in table form in Appendix B.

4. COMPARISON OF CROSSFLOW AND COUNTERFLOW FILL PERFORMANCE

4.1. Definition of tested fill configurations

The trickle fill that was used in the comparative experimental tests, shown in Figure 1.4 (c), has cross-fluted channels to facilitate air flow in a specific direction. Normally, the fill is installed so that these channels align with the expected direction of air flow, i.e. when installed in counterflow, these channels will be vertically orientated.

In the comparative experimental tests, three fill configurations were tested:

- In the counterflow test facility with the fill orientated as it would normally be in counterflow (channels vertical). These tests were done by Bertrand (2010).
- In the crossflow test facility with the fill orientated as it would normally be in crossflow (channels horizontal).
- In the crossflow test facility with fill orientated as it would normally be in counterflow (channels vertical). This configuration is henceforth referred to as “Crossflow (counterflow config.)”.

These three configurations are shown schematically in Figure 4.1

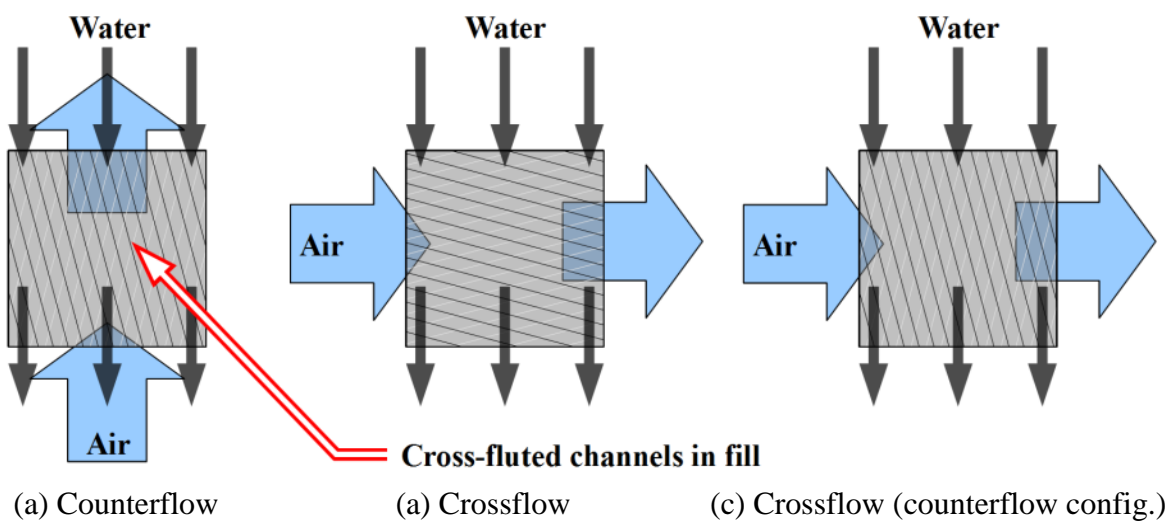


Figure 4.1: Illustration of the three tested fill configurations

4.2. Scope of experimental data

The characteristic equations that are determined for the fill are based on data from multiple fill tests. The test results are presented in table form in Appendix B. This subsection briefly describes the scope of the data on which the presented fill characteristic equations are based.

A single *test* is defined as a period of about 1 minute during which all data from the experimental facility was recorded. During this time, all the independent va-

riables, i.e. the water mass velocity G_w , air mass velocity G_a and water inlet temperature T_{wi} remained (very close to) constant and there was (very close to) no change in the outlet conditions.

A *test series* is defined as a group of tests that were done one shortly after the other. Within a test series all possible combinations of several predefined air- and water mass velocities are tested together in respective tests, e.g. 3 predefined water mass velocities and 4 predefined air mass velocities makes for $3 \times 4 = 12$ tests within the test series. Water inlet temperature decreases throughout the tests in the same order that the tests were done in. Table 4.1 shows the data recorded from such a test series of 12 tests.

Table 4.1: Experimental data recorded during a test series in the crossflow test facility

G_w^* kg/m ² s	G_a^* kg/m ² s	T_{wi} °C	T_{ai} °C	T_{wbi} °C	T_{wo} °C	dp_{fi} Pa	T_{wbo} °C	p_a Pa
1.5	1.0	52.012	19.208	17.178	29.719	27	39.036	100 860
1.5	1.5	51.014	19.138	17.152	26.259	55	35.533	100 860
1.5	2.0	49.928	19.070	17.098	23.366	95.5	32.502	100 860
1.5	2.5	49.427	19.008	17.072	22.452	163	30.307	100 860
3.0	1.0	48.235	19.023	17.035	34.339	31	42.302	100 860
3.0	1.5	47.502	19.180	17.125	30.970	60	39.650	100 860
3.0	2.0	46.472	18.991	17.048	28.142	106	37.077	100 860
3.0	2.5	45.623	18.777	16.942	25.855	174	34.739	100 860
4.5	1.0	43.891	19.076	17.035	35.470	36	40.852	100 860
4.5	1.5	42.936	18.964	16.999	32.757	66	38.818	100 860
4.5	2.0	41.343	18.772	16.923	29.707	121	36.127	100 860
4.5	2.5	40.253	18.625	16.854	27.608	192	34.080	100 860

*Rounded

The amount of experimental tests on which the various fill performance characteristic equations are based is given below.

Crossflow:

3 Test series with 4 water mass velocities and 4 air mass velocities
Total = 48 tests

Counterflow:

3 Test series with 4 water mass velocities and 7 air mass velocities
Total = 84 tests

Crossflow (counterflow config.):

4 Test series with 3 water mass velocities and 4 air mass velocities = 48 tests
1 Test series with 4 water mass velocities and 4 air mass velocities = 16 tests
Total = 64 tests

4.3. Determined fill characteristics

Fill characteristics data can be correlated by means of the following functions:

$$Me/L_{fi} = c1 G_w^{c2} G_a^{c3} T_{wi}^{c4} \quad (4.1)$$

$$K_{fdm}/L_{fi, x} = k1 G_w^{k2} G_a^{k3} + k4 G_w^{k5} G_a^{k6} \quad (4.2)$$

where T_{wi} is measured in °C

An optimizer is used to minimize the least squares error between the experimental data and the predictions made by Equations (4.1) and (4.2) by changing the values of the constants $c1$, $c2$, $c3$, $c4$, $k1$, $k2$, $k3$, $k4$, $k5$ and $k6$.

The characteristic equations that were determined for the three fill configurations, using this method are given in Table 4.2 and 4.3.

Table 4.2: Determined fill characteristic equations for Merkel number for different cross- and counterflow fill configurations

Fill configuration	Determined fill characteristic equations for $Me/L_{fi, z}$	R^2
Crossflow	$Me/L_{fi} = 1.2330 G_w^{-0.7550} G_a^{0.3450} T_{wi}^{-0.0279}$	0.987
Counterflow	$Me/L_{fi} = 1.6293 G_w^{-0.9250} G_a^{0.7760} T_{wi}^{-0.0986}$	0.994
Crossflow (counterflow config.)	$Me/L_{fi} = 1.5258 G_w^{-0.7754} G_a^{0.7996} T_{wi}^{-0.0730}$	0.983

Table 4.3: Determined fill characteristic equations for loss coefficient different cross- and counterflow fill configurations

Fill configuration	Determined fill characteristic equation for K_{fdm}/L_{fi}	R^2
Crossflow	$K_{fdm}/L_{fi, x} = 11.007 G_w^{0.2458} G_a^{-0.0974} + 3.4886 \times 10^{-7} G_w^{5.6876} G_a^{6.5011}$	0.994
Counterflow	$K_{fdm}/L_{fi, z} = 3.1980 G_w^{0.4920} G_a^{-1.4110} + 7.6960 G_w^{0.1100} G_a^{0.0910}$	0.982
Crossflow (counterflow config.)	$K_{fdm}/L_{fi, x} = 29.0167 G_w^{0.1332} G_a^{-0.0774} + 2.9590 \times 10^{-7} G_w^{8.9749} G_a^{2.0027}$	0.939

Note that Me/L_{fi} refers to Me_{e-NTU}/L_{fi} throughout this chapter.

The correlation coefficients (R^2), given in the last column of Table 4.2 and 4.3, show how well the determined fill characteristic equations approximate the experimental data. A correlation coefficient of 1 will indicate that the equation fits perfectly through the data. Figure 4.2 shows how the fill characteristic equations approximate the experimental data.

The fill characteristic equations are plotted on comparative graphs in Figures 4.3 to 4.10. Since it is clear from the characteristic equations in Table 4.2 that Me/L_{fi} number is a very weak function of water inlet temperature, all graphs are plotted only for a single water inlet temperature, namely $T_{wi} = 45\text{ }^\circ\text{C}$.

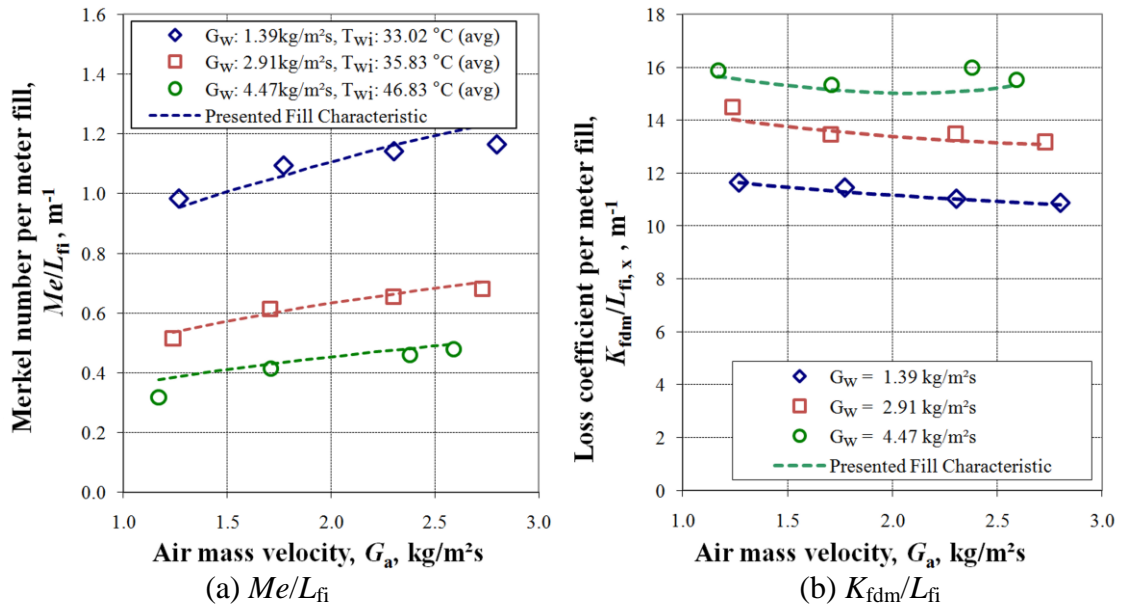


Figure 4.2: Sample comparison between experimental data from the crossflow test and presented fill characteristic equations for Me/L_{fi} and K_{fdm}/L_{fi}

Figures 4.7 and 4.8 show how the Merkel number and loss coefficient of the counterflow configuration compares to that of the others. Figures 4.9 and 4.10 show comparisons between the relative performance of the three fill configurations, where the relative fill performance is the Merkel number per meter of fill divided by the loss coefficient per meter of fill.

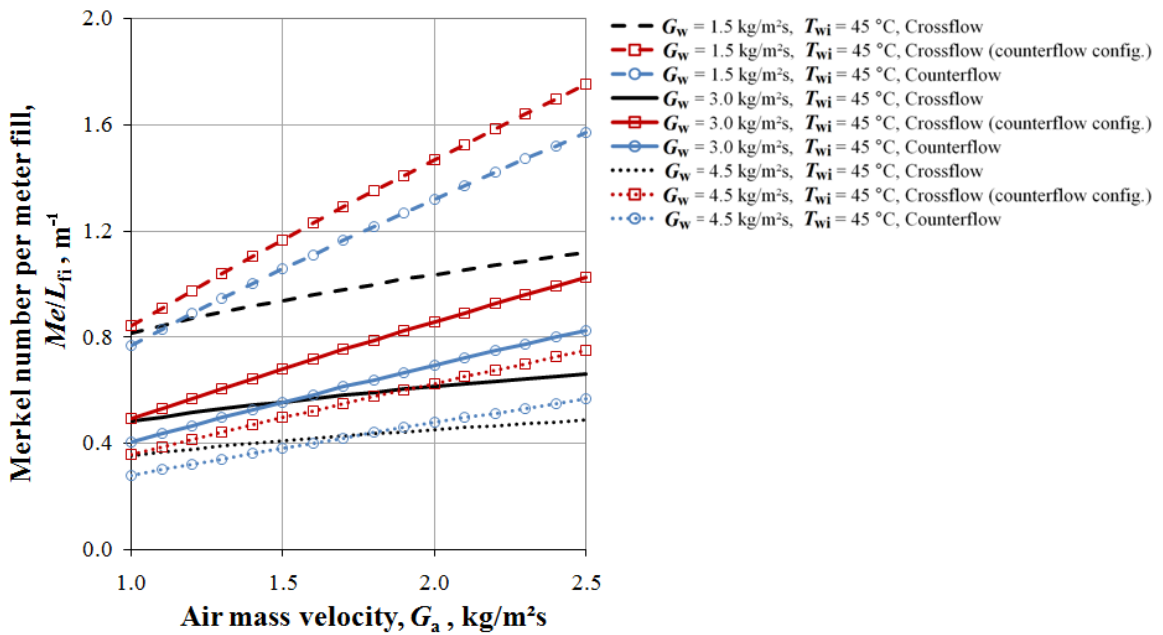


Figure 4.3: Me/L_{fi} predicted by fill characteristic equations, as a function of G_a , for different cross- and counterflow fill configurations and values for G_w

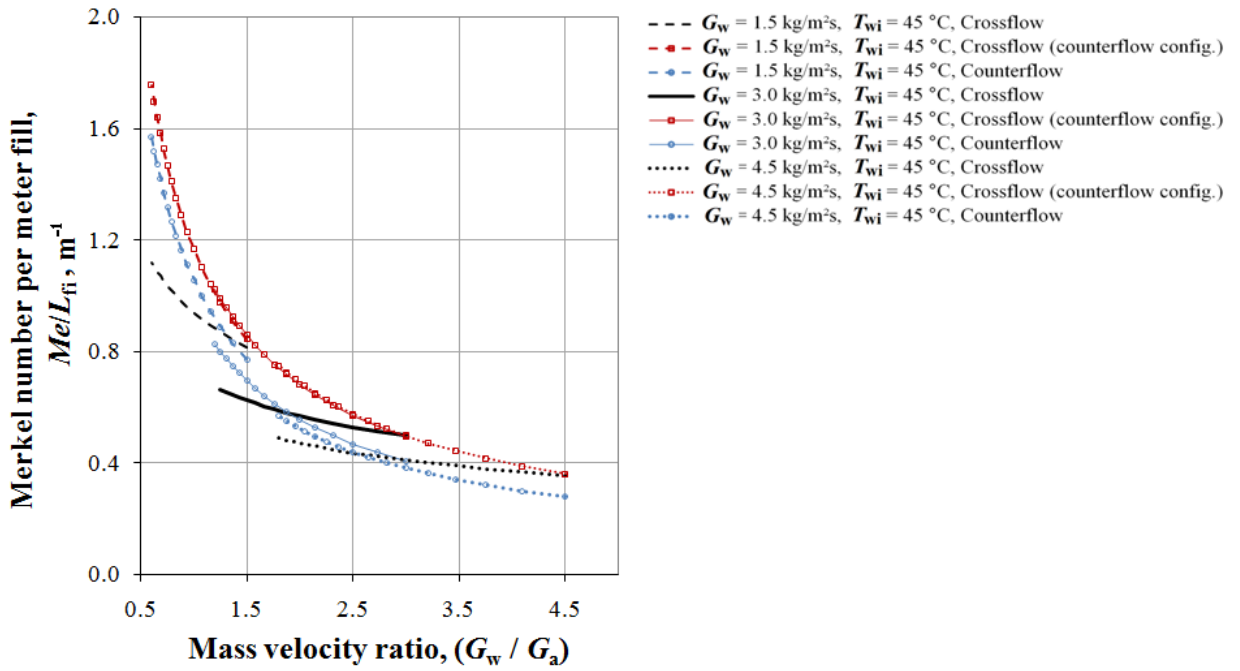


Figure 4.4: Me/L_{fi} predicted by fill characteristic equations, as a function of (G_w/G_a) for different cross- and counterflow fill configurations and values for G_w

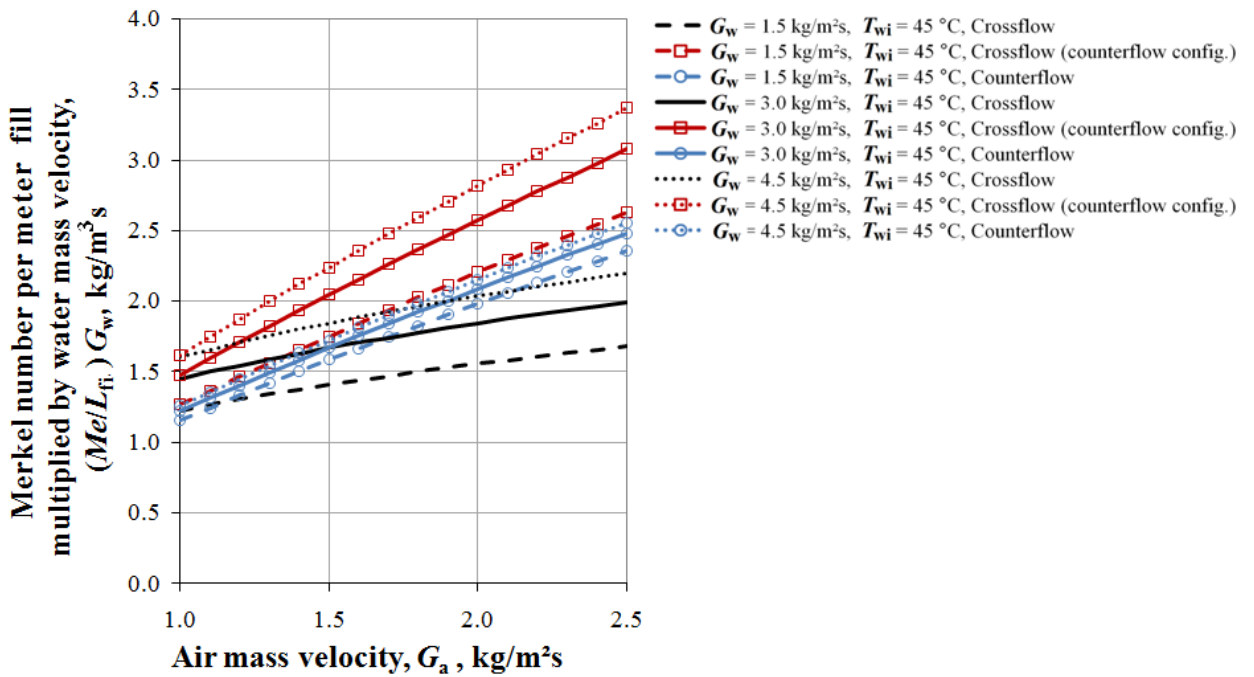


Figure 4.5: Me/L_{fi} predicted by fill characteristic equations, multiplied by G_w , i.e. effectively $h_d A_{fi} / L_{fi}$, as a function of G_a for different cross- and counterflow fill configurations and values for G_w

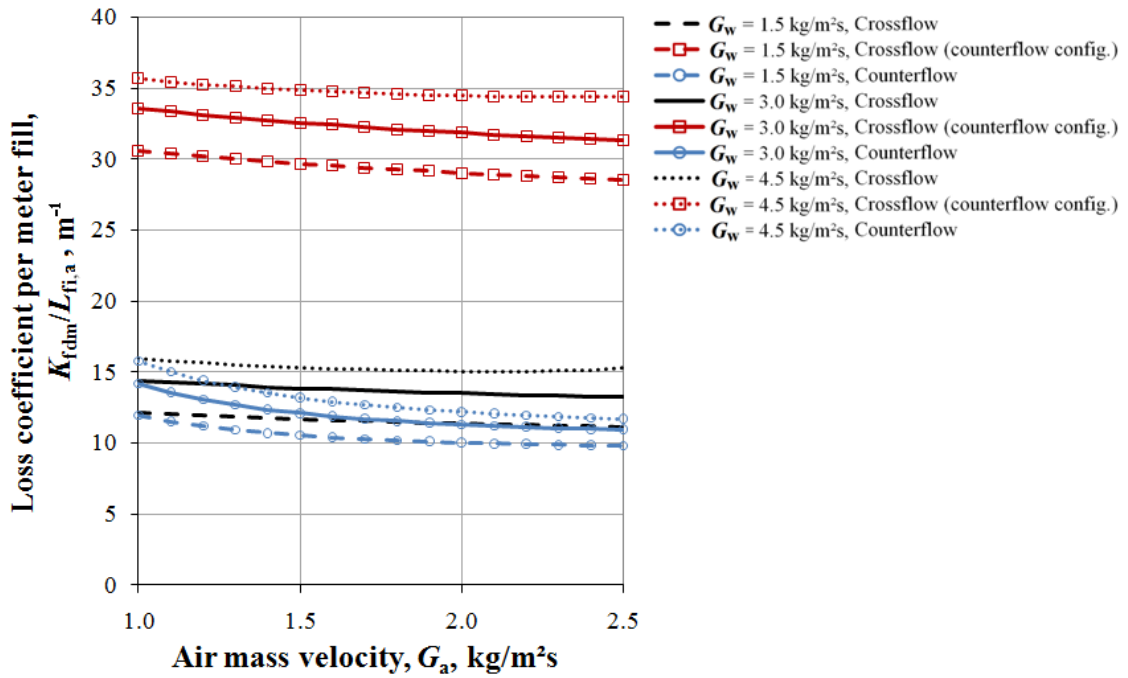


Figure 4.6: K_{fdm}/L_{fi} predicted by fill characteristic equations, as a function of G_a for different cross- and counterflow fill configurations and values for G_w

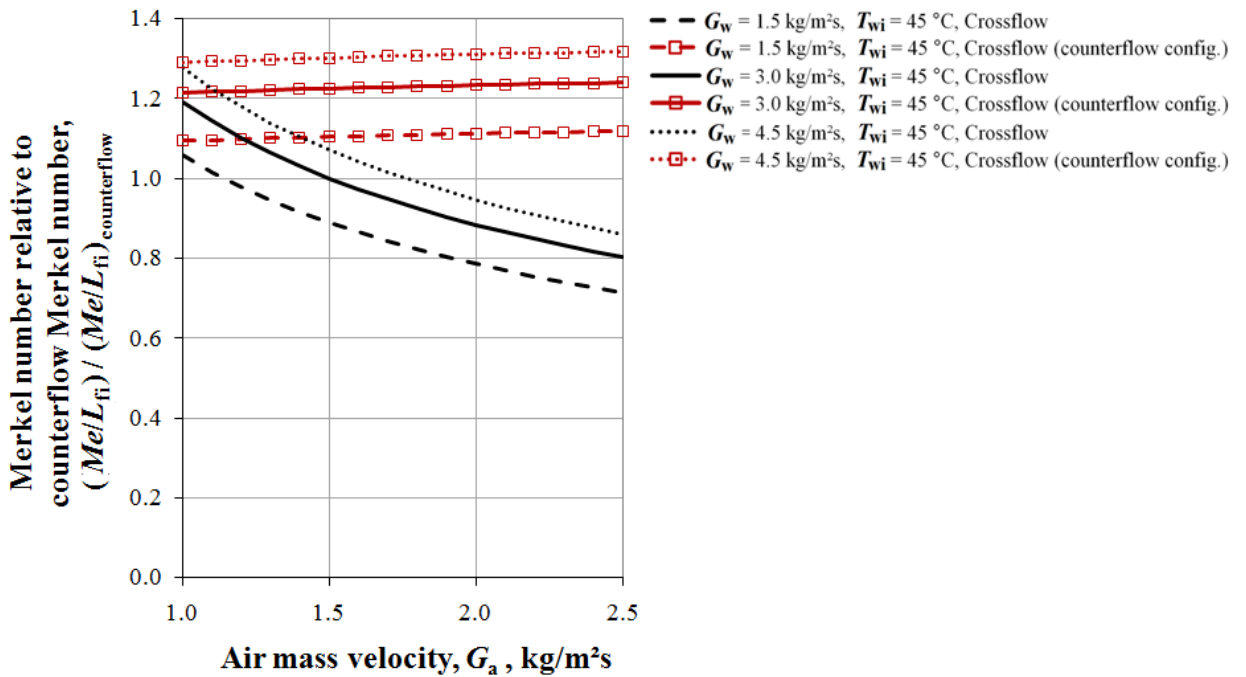


Figure 4.7: Me/L_{fi} for different crossflow fill configurations divided by Me/L_{fi} for fill in counterflow configuration, predicted by the fill characteristic equations, as a function of G_a for different values for G_w

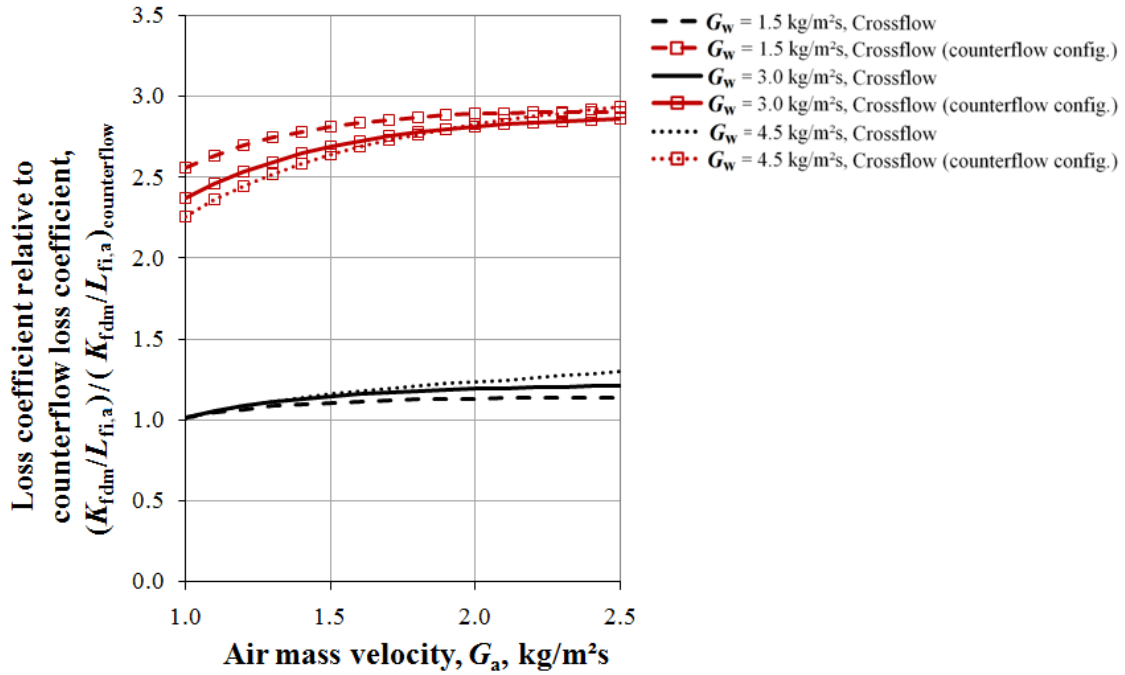


Figure 4.8: $K_{f,dm}/L_{fi}$ for different crossflow fill configurations divided by $K_{f,dm}/L_{fi}$ of fill for fill in counterflow configuration, predicted by the fill characteristic equations, as a function of G_a for different values for G_w

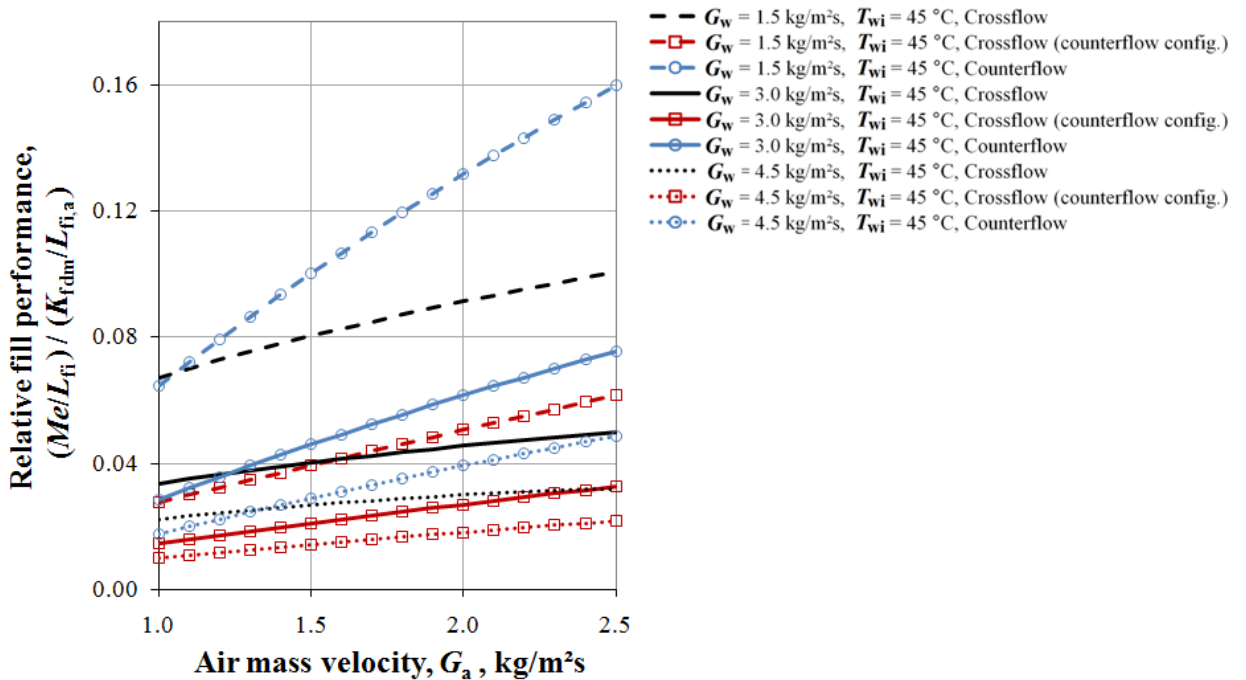


Figure 4.9: Relative fill performance predicted by fill characteristic equations, as a function of G_a for different cross- and counterflow fill configurations and values for G_w

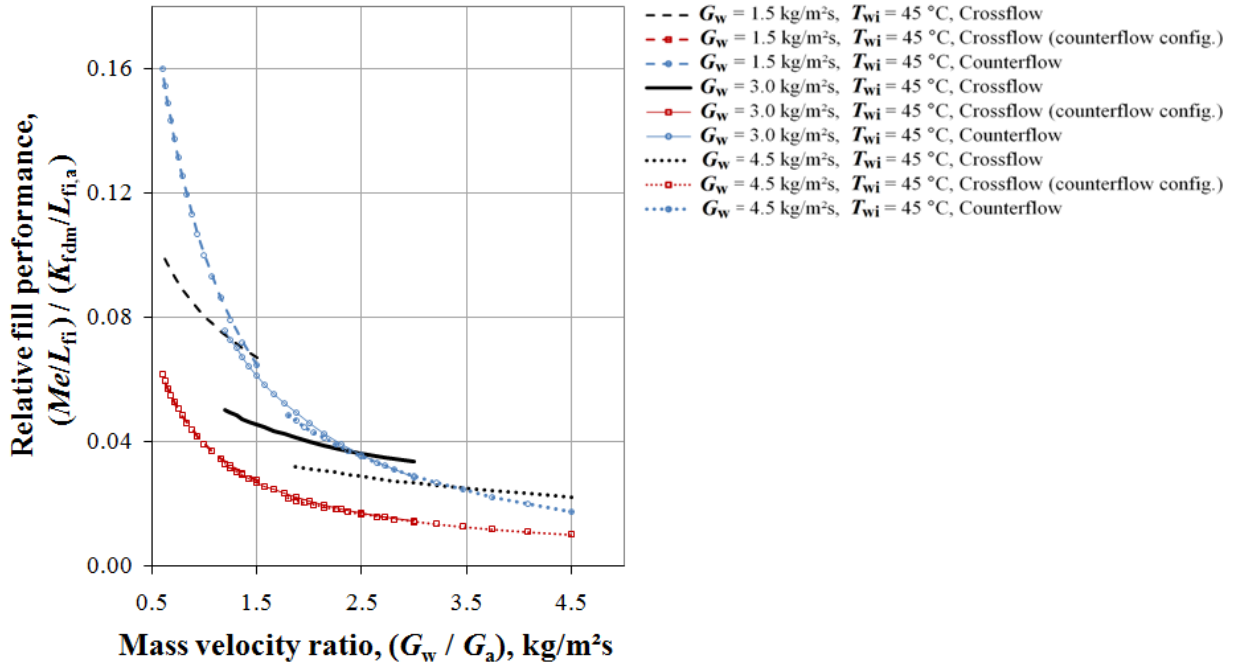


Figure 4.10: Relative fill performance predicted by fill characteristic equations, as a function of (G_w/G_a) , for different cross- and counterflow fill configurations and values for G_w

4.4. Discussion of results

From the characteristic equations it can be seen the Merkel number is a very weak function of water inlet temperature for all the tested fill configurations. However, the fill's behavior is highly dependent on the relative angle between the water and the air through it.

When the cross-fluted channels are not aligned with the air flow direction, the loss coefficient per meter of fill doubles (approximately) and a 25% (approximately) increase in Me/L_{fi} is observed. The higher loss coefficient is expected because of the aforementioned misalignment and it is speculated that the increase in heat transfer is due to higher turbulence that is associated with the steeper pressure gradient across the fill.

From Figure 4.3 it is observed that this particular fill displays a higher Me/L_{fi} in counterflow than in crossflow for the majority of air- and water mass velocities. It is believed that this is because, in counterflow, the water flow is retarded by the air flow, with the result that a given water particle spends a longer time in the cooling zone than it would in crossflow. This theory is further supported by the observation that crossflow performance relative to counterflow increases as the ratio of water mass velocity to air mass velocity increases, with crossflow even slightly outperforming counterflow at the highest (G_w/G_a) ratios. This can be observed best on Figures 4.4 and 4.10.

In this particular fill, the loss coefficient for counterflow is always lower than for crossflow. This is not due to the natural draft effect that is only present in counter-

flow: that is already taken into account when the loss coefficient is calculated (the term $(\rho_{avi} - \rho_{avm}) g L_{fi}$). Rather, it is speculated that the cause for this effect lies in the micro flow pattern of the water: In counterflow, the water flow is almost aligned to the cross-fluted channels in the fill, and it is therefore expected that the water would mostly 'stick' to the perimeter of the channels, causing little obstruction of the channel. In crossflow, the water falls closer to perpendicular to the channels, which should mean that more of the water drips through the channels. These falling drops would partly obstruct flow through the channels, and cause a slightly higher loss coefficient.

The characteristic equations in Table 4.2 show that, in the counterflow characteristic equation for the Merkel number, the exponent of G_w is close to -1, i.e. the counterflow Merkel number is almost inversely proportional to the water mass velocity. When we substitute the definition of the Merkel number (per meter of fill) $h_d a_{fi} / (G_w L_{fi})$ into the characteristic equation, G_w appears under the line on both sides of the equation and may be cancelled to reveal that, in counterflow, the term $h_d a_{fi}$ is practically independent of water mass velocity. This is illustrated in Figure 4.4, where the lines for different water mass velocities in counterflow lie very close to each other.

The independence of the term $h_d a_{fi}$ from water mass velocity is what one would expect from a film fill, where the water flows mainly in a film. When the water mass velocity increases, this film merely becomes thicker and there is little change in a_{fi} . Therefore the term $h_d a_{fi}$ remains almost constant. Evidently the tested trickle fill, when in counterflow, behaves similar to a film fill. This supports the previous assertion with regard to the water 'sticking' to the channel sides when in counterflow.

The fact that the crossflow configurations do show some dependence, albeit weak, on water mass velocity, support the current understanding of the flow mechanics within the fill: When in crossflow, significant dripping does take place within the fill and a higher water mass velocity will lead to more (and bigger) drops, increasing a_{fi} and consequently increasing $h_d a_{fi} / L_{fi}$, as is seen in Figure 4.4.

The amount of heat transferred in a fill zone depends mainly on the term $h_d a_{fi}$, rather than on the Merkel number. Therefore, it may be better to describe fill performance in terms of $h_d a_{fi}$ rather than in terms of the Merkel number, especially if $h_d a_{fi}$ is given as a characteristic equation in terms of G_a and G_w . Such equations would plainly reveal how some fills, such as film fills, do not transfer more heat when G_w increases, while other fills, such as splash fills, can take some advantage out of higher water mass flow rates.

5. COMPARISON BETWEEN EXPERIMENTAL RESULTS AND THE MODEL PREDICTIONS

The temperature profiles at the air- and water outlet that are measured during experimental crossflow tests, as described in Section 3.2.2, are compared to the profiles predicted using the Reuter model.

The procedure to do this is to determine a $Me_{\text{Reuter}}/L_{\text{fi}}$ from the experimental results presented in Appendix B using the methodology described in Section 2.2.6. The determined $Me_{\text{Reuter}}/L_{\text{fi}}$ is then used in the Reuter model to predict the cooling and the associated temperature profiles at the air- and water outlets, which are compared to the experimental results. Such a comparison is shown for a rain zones in Figure 5.1 and for trickle fill test in Figure 5.2.

Note that in these figures, the ‘distance along outlet’ is from the tunnel floor to the tunnel roof for the vertical T_{ao} , and from the air inlet side to the air outlet side for the horizontal T_{wo} .

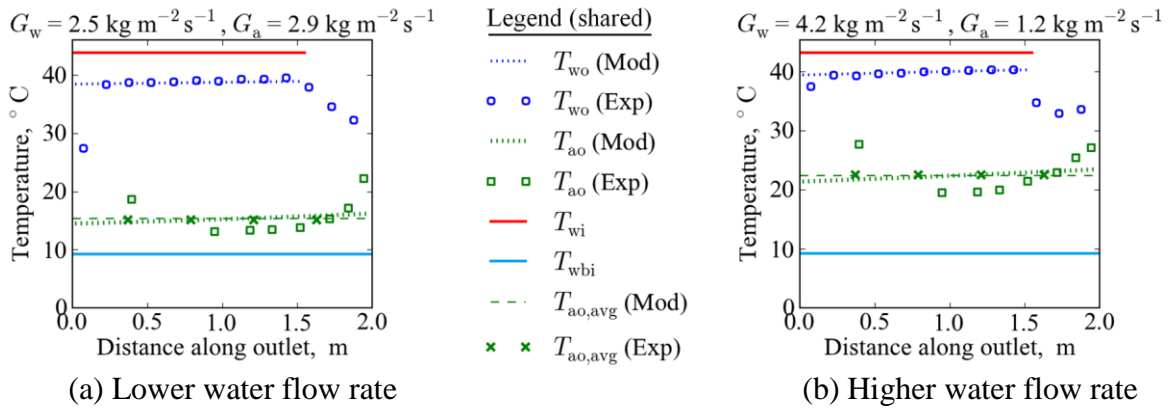


Figure 5.1: Comparison between the temperature profiles at the air- and water outlets of a rain zone that were predicted (Mod) the by the Reuter model and that were measured (Exp) during experimental tests

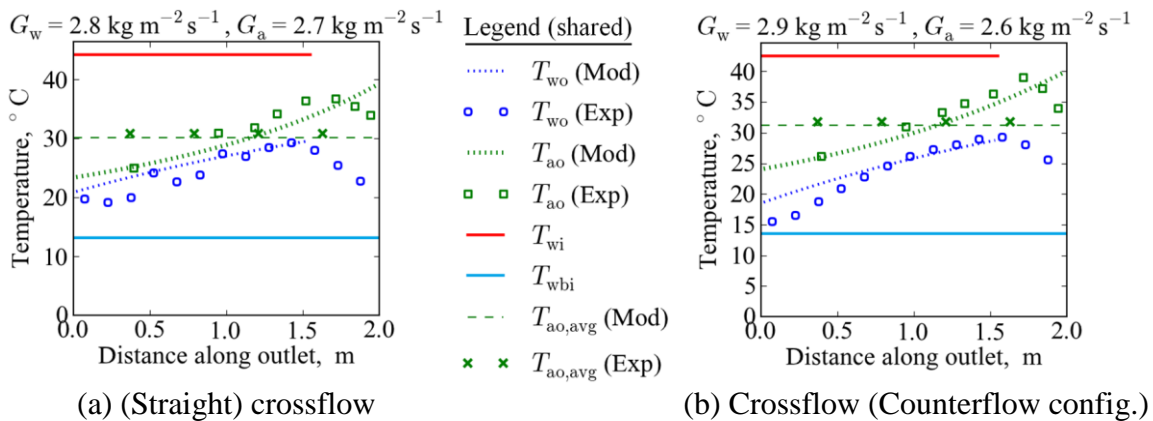


Figure 5.2: Comparison between the temperature profiles at the air- and water outlet of a trickle fill that were predicted (Mod) by the Reuter model and that were measured (Exp) during experimental tests

Figure 5.1 (a) and (b) are from respectively rain zone test #109020-08 and #100920-09. Figure 5.2 (a) is from trickle fill test #101002-07, while Figure 5.2 (b) is from trickle fill test #101209-08. This test data is provided in Appendix B.

5.1. Discussion of differences between model and experimental results for rain zone tests

The most notable differences between the model and experimental results for the rain zone that are marked as respectively D, S and C on Figure 5.3 are discussed below.

Effect of air drag

[D in Figure 5.3]

Because the falling water is dragged along by the air, the first (most upwind) trough in the water outlet rake catches little or no water.

The mass flow rate through that trough is therefore relatively low, and the water has some time to cool down before reaching the thermocouple at the trough outlet, which explains why the temperature measured in the first trough is significantly lower than that of its neighbor.

Some of the water that is dragged along by the air falls into the troughs located downwind from the spray frame (between 1.5 and 2.0 m) and the further the troughs are downwind from the spray frame, the less water they catch. The water in these troughs is colder than the water in the troughs below the spray frame because:

- Since, the smaller drops are dragged along more than the bigger drops, the downwind troughs catch mostly smaller drops and smaller drops cool down much faster than big ones (Reuter, 2010)
- The mass flow rate through these troughs is lower, which (just like with the first trough) allows the water to cool down somewhat while in the trough.

Since the Reuter model assumes strictly vertical water motion, it does not reproduce the air's drag effect at either the air inlet or outlet side.

Splash effect [S in Figure 5.3]

As the drops hit the measurement equipment at the bottom of the test section, it splashes back up into finer drops, which lead to a much higher interfacial area between the drops and the air near the water outlet of the test section. This effectively increases the heat transfer and the associated Me/L_{fi} here, which explains why the air temperature that is experimentally measured near the water outlet is so

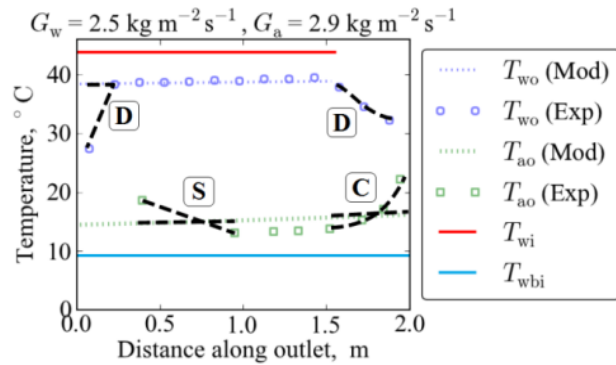


Figure 5.3: Notable differences between experimental and model results for a rain zone

high. This effect cannot be reproduced with the Reuter model if a uniform Me/L_{fi} is used, as was the case in this comparison. However, with knowledge of the drop sizes, throughout the test section, including that of the splashing drops, this effect could be reproduced by using a discrete phase CFD model or by using the single drop model to determine approximate Me/L_{fi} s as a function of z and then using the Reuter model, with a variation in local Me/L_{fi} s, to determine the water and air outlet condition. Due to time constraints, this was not attempted in this study.

Effect of varying drop concentration [C in Figure 5.3]

The drops just below the water inlet have a lower velocity than the drops further down and therefore the concentration of drops just below the water inlet is the highest. This higher concentration means a higher interfacial area between the water and the air, which effectively increases the heat transfer and the associated Me/L_{fi} . The Reuter model cannot take this denser spacing into account if a uniform Me/L_{fi} is assumed as is usually done, and this is why the air outlet temperature that is experimentally measured just below the water inlet is considerably higher than the model result.

However, the Reuter model and the single drop model could be used together to take this local variation in Me/L_{fi} into account. This is done in Section 5.2.

5.2. Using the Reuter model with a non-uniform Me/L_{fi}

With the inlet conditions and Sauter mean drop diameter given, the single drop model may be used to determine a Me/L_{fi} for the top segment of the test section. For this purpose, the experimental values are used for the inlet conditions, while the drop diameters corresponding to the inlet water mass velocities are drawn from experimentally measured drop size data from Banda (2008) and Terblanche (2007). The Reuter model may then be used with the Me/L_{fi} predicted by the single drop model used to predict the air outlet condition and a $T_{wb,avg}$, which can be plugged back into the single drop model until $T_{wb,avg}$ and Me/L_{fi} converge for that segment of the test section.

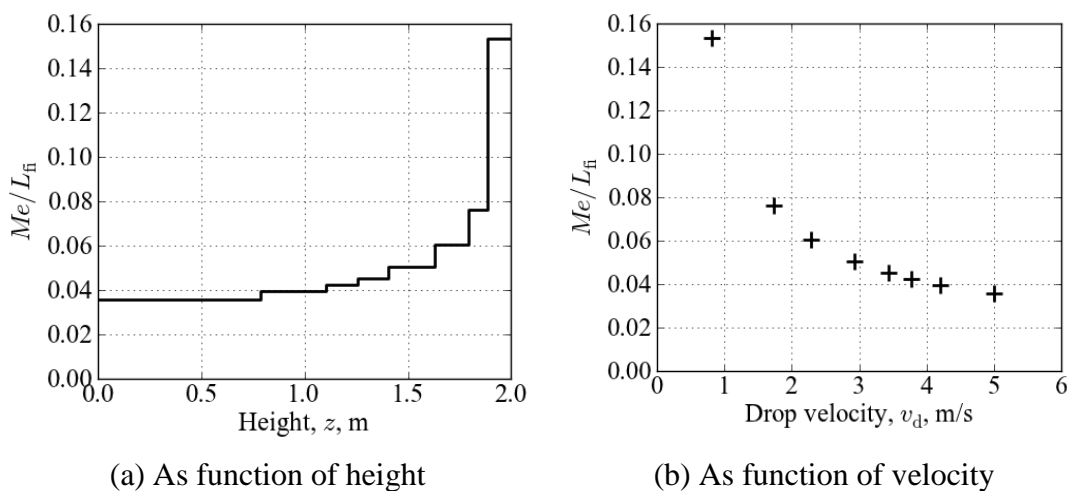


Figure 5.4: Variation in Me/L_{fi} (per zone) in a rain zone for a specific test case

The variation of Me/L_{fi} over the test section that is determined using the above methodology is shown in Figure 5.4. It is clear that the average local Me/L_{fi} will be a function of rain zone height. This also applies to fills.

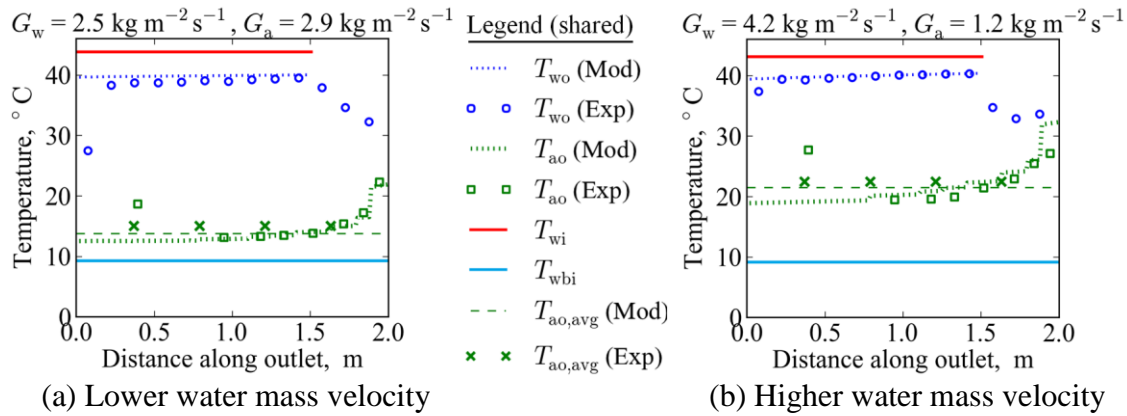


Figure 5.5: Comparison between experimental results and results from a combination of the Reuter and single drop models

The water outlet condition from the top segment of the test section is then used as an inlet condition for the second segment and the procedure to converge $T_{wb,avg}$ and Me/L_{fi} is repeated. In this way, all of the segments of the test section can be modeled and the results obtained for the water outlet of the bottom segment represent the water outlet for the entire test section and the air outlet conditions of the various segments may be 'stacked' on top of each other to obtain the model's prediction for the air outlet. The results from modeling a rain zone in this way are compared to experimental results in Figure 5.5.

The model shows warmer water outlet and colder air outlet than the experimental results, or, in other words: less heat is transferred in the model than in the experimental case. This is because the model is now no longer based on the average water outlet condition and additional heat transferred by the splash effect, which causes increased heat transfer, cannot be taken into account.

5.3. Discussion of differences between model and experimental results for trickle fill tests

The most notable differences between the model and experimental results for a trickle fill that are marked by respectively F, I, W and D on Figure 5.6 are discussed below.

Drag effect [D in Figure 5.6]

The drag effect near the air outlet for the trickle fill test is similar to the drag effect near the air outlet discussed in Section 5.1.

Effect of non-homogenous fill [F in Figure 5.6]

The irregularity that is observed in the experimental water outlet temperature profile can be understood by considering the arrangement of the blocks of fill shown in Figure 5.7 (a): The small gaps between the blocks of fill run down from the top of the test section to the bottom. Since the water can run freely through the gap, it

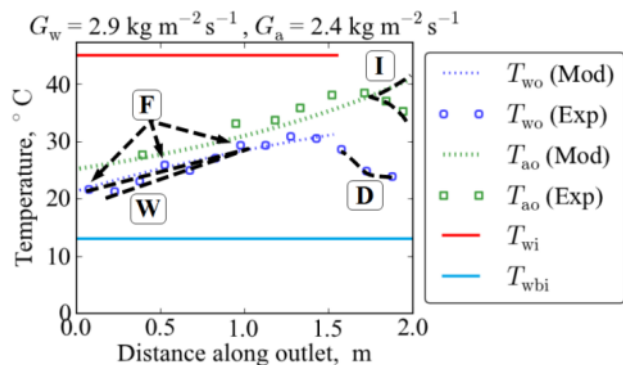


Figure 5.6: Most notable differences between experimental and model results for a trickle fill

travels faster and is not distributed over a larger surface area and is therefore not cooled as much as the water within the fill.

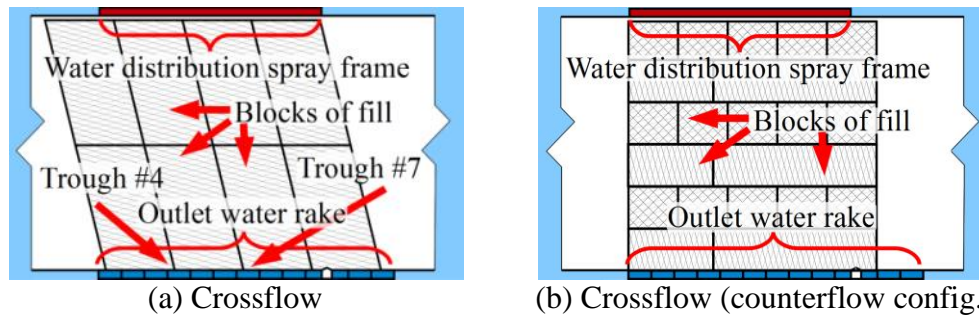


Figure 5.7: Comparison between arrangement of fill blocks in the crossflow test section for trickle fill test configurations

Note how, in Figure 5.7 (a), the gaps between the blocks of fill end just above the first, fourth and seventh trough in the water outlet rake, and how, correspondingly, these troughs show higher experimentally measured water temperatures than their neighbors in Figure 5.2 (a). Conversely, the arrangement of blocks of fill for the crossflow (counterflow config.), shown in Figure 5.7 (b), has no gaps running from top to bottom and, accordingly, the irregularity in the water outlet profile is not observed in Figure 5.2 (b).

The gaps in the straight crossflow fill arrangement represent an experimental shortcoming which, now that its significance has been observed, should be addressed in future tests. Effectively, they cause regions within the test section to have a much lower Me/L_{fi} than the rest of the test section. This is not reproduced when the Reuter model is used with a uniform Me/L_{fi} .

Reduced interfacial area between water and air near water inlet

[I in Figure 5.6]

The lower air temperature that is observed near the water inlet is attributed to the combination of two factors:

- Due to practical restrictions, a small gap in between the fill's 'top' and the water inlet is unavoidable. The water free falls through this gap.
- The water, which leaves the water distribution spray frame through a matrix of $\varnothing 3$ mm holes spaced 30x30mm, needs to flow through the fill for some distance in order for the fill to redistribute it over a larger area. The top segment of the test section is therefore expected to have a lower interfacial area between the water and the air.

Both of these factors imply that the interfacial area between the water and the air is less near water inlet than in the rest of the test section and therefore the Me/L_{fi} and heat transfer rate is lower also.

Decreased water mass velocity near air inlet [W in Figure 5.6]

The water outlet temperatures near the air inlet that are measured experimentally are consistently lower than what the model predicts. This is attributed to the fact

that the water mass velocity near the air inlet is less than in the rest of the fill. This latter statement is substantiated in Section 5.4.

From the fill characteristic equation for this fill, provided in Table 4.2, it can be seen that a lower local water mass velocity should lead to a higher local Me/L_{fi} , which, in turn, will result in a more rapid (local) cooling of the water. It is therefore expected that the model, which assumes a constant Me/L_{fi} throughout the fill, will predict a higher temperature at the upwind side of the fill than would be measured experimentally. On Figure 5.2 (a) and (b), it can be seen that this is the case.

5.4. A first approximation of the water mass velocity distribution within the fill in the crossflow test facility

In crossflow, water is dragged along by air flow through the fill. The average angle of the water flow through the fill, relative to the vertical, is referred to as the *drag deflection angle* θ . Due to the fill's geometry, the water is also redistributed as it flows through the fill. The combination of the drag deflection and water redistribution leads to a non-uniform water distribution, which is at present unknown, within the fill.

Bertrand (2011) experimentally measured the migration of water through the same trickle fill that was used for tests in this study and determined that the difference between the water mass velocity at the fill's sides and its center could be as much as 40%. A sample from his measurements is shown in Figure 5.8. However, the distribution in crossflow may be different from Bertrand's for the following reasons:

- In crossflow, the water is dragged sideways by the air.
- In crossflow, the fill can be wider than the water inlet.
- The fill can be orientated in a different direction and consequently redistributes the water differently.

Since the distribution of water flow throughout the fill directly affects the cooling, and especially the measured temperature profiles in the water outlet, an analysis is done to make a first approximation of what the mass velocity profiles at the water outlet may look like.

Because the interaction between the fill, the air and the water is quite complex it is no trivial task to model the actual flow of water through the fill. Due to practical restrictions, it is also not easy to experimentally measure the water distribution

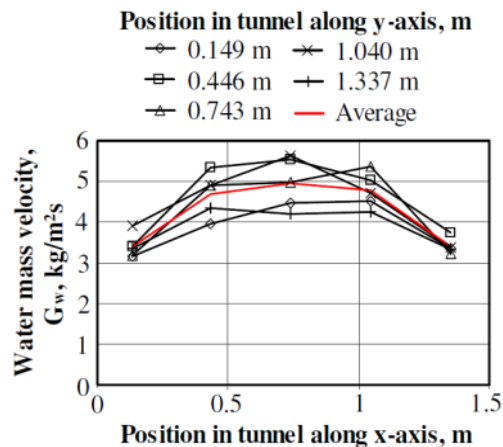


Figure 5.8: Water mass velocity distribution under 1.5 m trickle fill with $G_w = 4.423 \text{ kg/m}^2\text{s}$
(Source: Bertrand, 2010)

profiles beneath the fill in the crossflow test section. A simplified mathematical approach is therefore used to obtain a first approximation of the mass velocity profiles at the water outlet.

For this analysis, it is assumed that water entering the fill at a point is redistributed over a length that is determined by the drag deflection angle θ and the redistribution half-angle ψ , as is illustrated by the dashed lines in Figure 5.9. At the fill outlet, the water from the point is assumed to have been redistributed by the fill into a triangular profile such as is indicated by the solid line in Figure 5.9. The mass flow rate of the water entering at the point must be equal to the integral of the triangle.

When the water enters the fill at various points (or when an inlet mass velocity and spray frame length is specified rather than a point mass flow rate), the triangular outlet profiles of the various 'points' are added to one another to determine the mass velocity profile at the water outlet. These integrated mass velocity profiles are shown in Figure 5.9 for spray frames lengths of 0.45 m and 1.50 m.

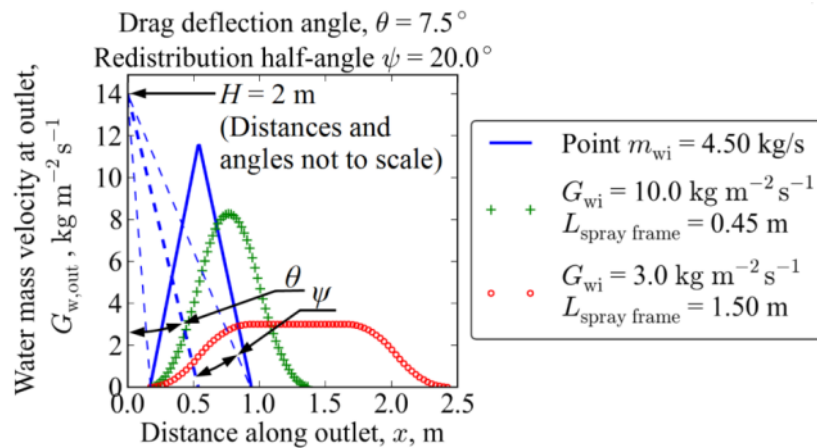
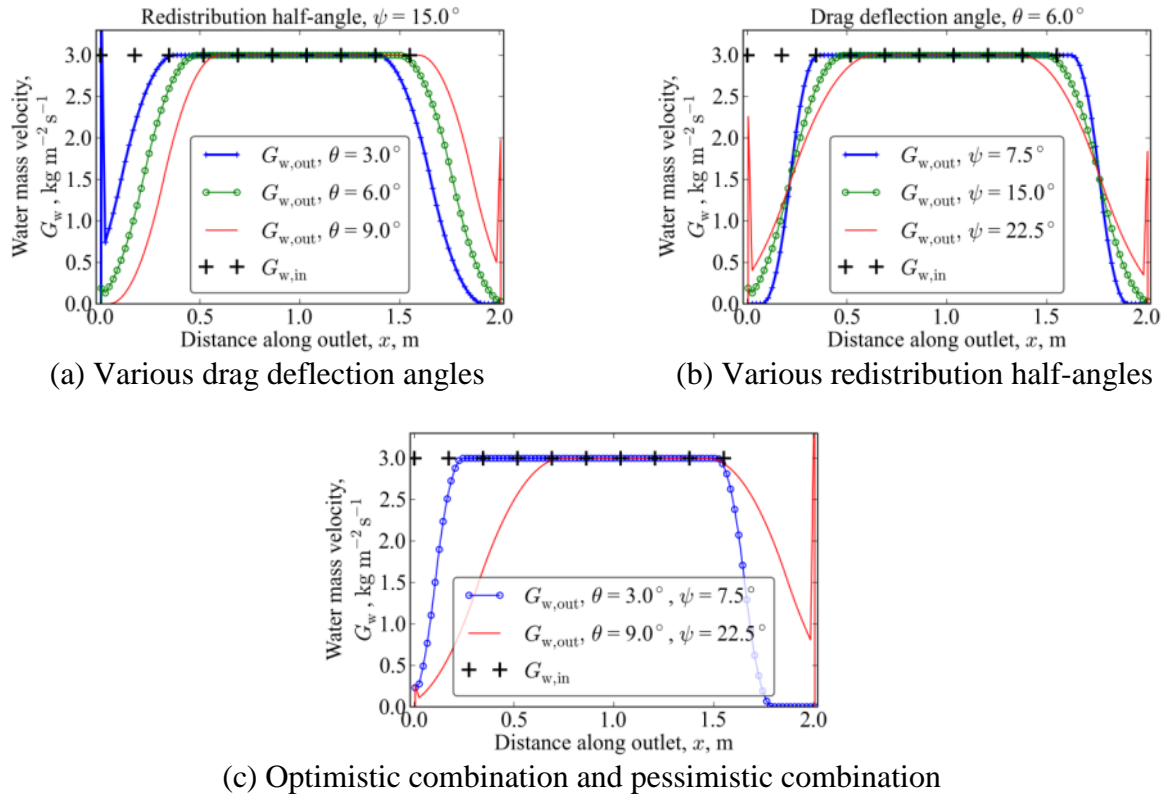


Figure 5.9: Water outlet mass velocity profiles caused by drag deflection and redistribution through an infinitely wide fill for various lengths of spray frames with $G_{w, in} = 3 \text{ kg m}^{-2} \text{ s}^{-1}$

Water outlet mass velocity profiles for the crossflow test facility that were calculated using the methodology described above, given various water drag deflection angles and redistribution half-angles, are shown in Figure 5.10. Note also that in the crossflow facility, the fill is not infinitely wide and it is therefore assumed that when water reaches the sides of the fill, it flows directly downwards from there.

Even though these mass velocity profiles shown in Figure 5.10 were determined using speculative drag deflection angles and redistribution half-angles, they demonstrate that even relatively conservative drag deflection angles and redistribution half-angles have a significant impact on the profile of the water outlet mass velocity.



(a) Various drag deflection angles (b) Various redistribution half-angles
(c) Optimistic combination and pessimistic combination
Figure 5.10: Water outlet mass velocity profiles in crossflow test section calculated for various drag deflection angles (θ) and redistribution half-angles (ψ)

This non-uniformity of the water mass velocity within the fill during experimental tests will necessarily mean that the temperature profiles in the water outlet measured during the experimental tests will not match the profiles obtained when the fill is modeled under the assumption of zero horizontal water flow. This is because zones with a lower water mass velocity will exhibit a higher temperature decrease.

A comparison between the outlet profiles that were measured in the experimental tests and the profiles that were determined using the Reuter model, shown in Figure 5.2, display the expected deviation:

The experimentally measured profile has lower temperatures on the upwind and downwind side of the fill, where lower water mass flow rates are expected. The agreement between the experimental results and the model predictions is much better towards the horizontal center, where the experimental water mass velocity is expected to be more uniform and close to the average that was used in the model.

5.5. Summary

Figure 5.1 and Figure 5.2 show fair agreement in the temperature profiles in the water outlet measured experimentally and predicted by the (basic) Reuter model. The agreement between the temperature profiles in the air outlet is poor for the

trickle fill and non-existent for the rain zone. However, when the Reuter model is used with a non-uniform Me/L_{fi} to model the rain zone, the agreement in the temperature profiles at the air outlet is much better.

However, all the most notable differences between the experimental results and the models can be clearly explained and they are mostly attributed to local variations in Me/L_{fi} that are caused by experimental edge effects.

It should also be noted that the models do very well to predict the average air temperature in all cases. On average, the difference between the air temperature that is predicted by the model and that is measured experimentally is less than 0.4 °C.

6. CONCLUSIONS AND RECOMMENDATIONS

6.1. Project outcomes

The primary goal of this project was to investigate the difference the difference between the crossflow and the counterflow fill performance characteristics of a trickle fill. The secondary goal was to test the validity of the Reuter model by comparing model predictions to experimental results.

The objectives that were set in order to reach these goals are stated in Chapter 1 and repeated below.

1. Critically evaluate the crossflow fill test facility at Stellenbosch University and make improvements where necessary.
2. Design, manufacture and install sensor rakes in the crossflow test facility so that the temperature profiles at the air and water outlets can be measured and compared to model predictions.
3. Perform crossflow tests in the upgraded test facilities with a trickle fill in two different configurations. Ensure that these tests are performance comparable to the trickle fill tests that Bertrand (2011) did. Additionally, perform rain zone tests. Measure and record the temperature profiles at the air and water outlets during all tests.
4. Investigate the differences between the performance characteristics of a trickle fill in crossflow and in counterflow by comparing the recorded test data to Bertrand's data and discuss the differences.
5. Implement the Reuter 2-dimensional evaporative cooling model and the single drop model into a computer program and verify that they are correctly implemented by comparing their outputs to published results from Reuter (2010) and Gudmundsson (2012). Report any valuable lessons that are learned during the process.
6. Compare the temperature profiles at the air and water outlets that are predicted using the Reuter model and the single drop model to those that are measured experimentally. Investigate and discuss the reasons for any differences between the experimental results and model predictions. Make a conclusion about the performance of the Reuter model.
7. Make recommendations for future researches about further improving the crossflow test facility at Stellenbosch, about performing crossflow tests and about the implementation of the Reuter model and single drop model into computer programs.

The steps taken to achieve each of these objectives are summarized and the outcomes are briefly discussed below.

Objective 1

The crossflow test facility was critically evaluated and multiple opportunities for improvement were identified and consequently improvements were made. The improvements are listed in Section 3.6.1 and briefly described in Appendix D.

The uniformity of the inlet water distribution provided by the water distribution spray frame was experimentally measured and improved (Section 3.6.3). At a low flow rate of $G_w = 1.42 \text{ kg m}^{-2} \text{ s}^{-1}$ a standard deviation of $\sigma = 0.556 \text{ kg m}^{-2} \text{ s}^{-1}$ (39%) was initially measured. After the water distribution spray frame was modified, the standard deviation that was measured at the same flow rate was only $\sigma = 0.156 \text{ kg m}^{-2} \text{ s}^{-1}$ (11%). The 11% deviation is attributed to fouling and/or the limited precision during manufacture, but due to time constraints this was not further addressed.

Correction factors were determined (Section 3.6.2) and implemented to improve the accuracy at which relative temperature measurements are made by the 53 thermocouples in the test section and, in so-doing, the maximum measured error in relative temperature was decreased from approximately 1°C to 0.4219°C , while the average error in relative temperature was brought down to 0.0631°C . This degree of accuracy is accepted as the experimental limit, but it is taken into account during the uncertainty analysis discussed below.

The average uncertainties in the Me/L_{fi} , K_{fdm}/L_{fi} and EB that are measured in the test facility were conservatively determined (Section 3.5.4) to be 5.4%, 5.2% and 3.0% respectively. These uncertainties seem quite large but it should be taken into account that they were determined under the assumption that assumes all measurement errors have a cumulative effect, which is a worst case scenario.

Objective 2

The two sensor rakes that are shown and described in Section 3.2.3 were designed, manufactured and installed in order to enable the measurement of temperature profiles at the test section air and water outlets. More detail on the work itself is reported in Appendix D.

The profiles that were measured using these rakes can be seen in Chapter 5. Some of the measured profiles did not match the trends that were initially expected, but upon closer investigation, all the deviations from the expected trends could be clearly explained. It is therefore concluded that the rakes are effective at accurately measuring the temperature profiles at the air and water outlets.

Objective 3

The performance of a trickle fill in crossflow was tested in two configurations by doing numerous trickle fill tests. These tests are performance comparable to Bertrand's tests. The results from these tests are used to determine characteristic equations for the two respective configurations in crossflow.

64 (5 series) rain zone tests were done.

During all 166 crossflow tests, the temperature profiles at air and water outlets were measured and recorded for comparison to the Reuter model's predictions.

Objective 4

Characteristic equations are fitted to crossflow experimental data recorded during this study and to counterflow experimental data from Bertrand (2010). In Sec-

tion 4.3, these equations are comparatively plotted to graphs and the trends that are revealed in this way are well understood and explained in Section 4.4.

The difference between the fill performance characteristics in crossflow and counterflow can be observed on the graphs to vary, as a function of air and water mass velocity, between 0 and 35% for Me/L_{fi} and up to almost 200% for K_{fdm}/L_{fi} .

This is further discussed in Section 6.2.

Objective 5

The Reuter model was implemented into a computer program using Python 2.7 and FORTRAN 95. The solution speed of the program was increased using a variety of methods that are described in Section 2.2.6 and 2.2.7, and on a standard office PC, the final, improved version takes about 15 seconds to determine Me/L_{fi} (of a benchmark case) from test measurements. This is approximately 326 times faster than before the improvements were made.

Through a grid dependence test using the computer program, it is determined that a cell size of 19x19 mm provide solutions that are within 0.54% of the solution with an infinitely small cell size, according to Roache's (1997) method of grid refinement.

Results from the program are compared to those published by Reuter (2010) and Gudmundsson (2012) and the largest difference in calculated results is 0.77 %. It is therefore concluded that computer program correctly implements the Reuter model and that it may be used with confidence to compare the Reuter model predictions to experimental results.

The single drop model is implemented into a computer program and the output is validated against Reuter (2010). This computer program plays an important role in the comparison between the Reuter model and the experimental results. A complete sample calculation to model a drop in cross-counterflow is presented in Appendix A.

Objective 6

A comparison between the experimental results and model results is presented and discussed in Chapter 5, and all the differences are well understood. The outcomes of the comparison are discussed in Section 6.3 (Conclusion about validity of the Reuter model).

Objective 7

Recommendations are made in Section 6.5.

6.2. Conclusion about the difference between crossflow and counterflow fill performance characteristics of a trickle fill

The project's primary goal to investigate the differences between the crossflow and counterflow performance characteristics of a trickle fill is accomplished:

The relative difference between crossflow and counterflow can be between 0 and 35% for Me/L_{fi} , but almost up to 200% for K_{fdm}/L_{fi} . The magnitude of this difference depends on the air and water mass velocities.

Reuter's proposed linear interpolation method should therefore only be used to model trickle flow under the following condition: There are characteristic equations available for the particular trickle fill that show that, for the given combination of water and air mass velocity, the difference between the fill performance characteristics in crossflow and in counterflow is small enough.

If more can be learnt about the linearity of the fill performance characteristics as a function of the relative angle between the water and the air, then the interpolation method can potentially be used more widely. Recommendations are made in Section 6.5.1 of how this linearity may be investigated. Until such an investigation is done, the improved testing facilities at Stellenbosch University and the experience that has been gained in fill tests will be useful for determining the characteristic equations of anisotropic fills in crossflow and in counterflow. These equations can be used to determine the potential interpolation error and thereby an informed decision can be made about whether or not the interpolation method is suitable for modeling a given fill.

6.3. Conclusion about validity of the Reuter model

The project's secondary goal to investigate the validity of the Reuter model by comparing its predictions to experimental results is accomplished, but calls for further investigation:

The Reuter model predicts the average temperature of the air at the outlet to within about 0.4°C. This is roughly 3% of the difference in temperature between the water at the inlet and at the outlet, and it is about 2% of the difference between the temperature of the inlet air and the inlet water.

The temperature profiles that were experimentally measured are found to be subject to significant edge effects that are not reproduced by the Reuter model if a constant and uniform Me/L_{fi} is assumed and the redistribution of the water by the fill is not brought into consideration. Recommendations are made in Section 6.5 on what can be done differently in both the experimental tests and the implementation of the Reuter model in order to obtain a better comparison between the two.

6.4. Other contributions made during this project

- The results from 220 different trickle fill and rain zone tests in the improved crossflow facility are published in Appendix B. This experimental data can be useful to other researchers in the field of cooling tower design (or in related fields).
- The three sets of characteristic equations that were determined for the trickle fill can be useful to researchers and cooling tower designers who want to model a cooling tower with such a fill installed.

- The comparison between crossflow and counterflow fill performance characteristics (discussed in Section 4.4) provides insight into anisotropic fill performance that can be of value to other researchers in the field of cooling tower design (or in related fields) and to cooling tower designers.
- The Stellenbosch University crossflow test facility was significantly improved and future researchers who use it can benefit from the work done. In particular, the facility can now be used to investigate the difference in fill performance characteristics between crossflow and counterflow for additional types and designs of fill. Carrying out such performance comparable cross- and counterflow tests is made considerably easier and better by the improvements that were made and the lessons that were learned during this project.
- The improved methods to solve the Reuter model that were developed during this project (discussed in Section 2.2.5 and 2.2.8) can be useful to future researchers who implement the Reuter model into a computer program.
- No sample calculation for the single drop model in cross-counterflow was found in literature. A complete sample equation of the single drop model in cross-counterflow is therefore provided in Appendix A and can be useful to future researchers who implement the single drop model into a computer program.
- The uncertainties in the Me/L_{fi} , K_{fdm}/L_{fi} and EB that are currently measured in the crossflow test facility have been determined. Knowledge of these uncertainties is useful because it shows the (current) confidence level of experimental measurements.

6.5. Recommendations for ongoing research

6.5.1. Investigate the linearity of fill performance characteristics of anisotropic fill as a function of the relative angle between the air and the water

Knowledge of the linearity of this function (for particular fills) will be very valuable when modeling anisotropic fill. If it can be shown that the function is close to linear, Reuter's interpolation method can be used with confidence even in cases with high differences in the crossflow and counterflow fill performance characteristics.

An investigation of the linearity could be attempted through the construction of a pioneer cross-counter flow fill test facility, or by developing a numerical model that can take the interaction between the fill material, the water and the air into account.

Since K_{fdm}/L_{fi} shows a much bigger difference between cross- and counterflow the Me/L_{fi} , priority should be given to investigating its linearity as a function of air flow angle. An interesting and feasible way to approach this could be to measure the pressure drop over (dry) fill in a small wind tunnel at various fill orientations. The K_{fdm}/L_{fi} 's that are determined from the measured pressure drops could then be compared to K_{fdm}/L_{fi} 's from normal tests in the crossflow and counterflow fill test facilities. If the relationship between the crossflow and counterflow K_{fdm}/L_{fi} is

the same for the dry and the normal tests, it stands to argue that the in-between relationships will also be the same.

6.5.2. Refine the implementation of the Reuter model

It was shown in Section 5.2 that when the local variations in Me/L_{fi} is taken into consideration for a rain zone, the Reuter model can make much more accurate predictions. The Reuter model does not require a constant, uniform Me/L_{fi} when it is numerically implemented. It is therefore recommended that in future numerical implementations of the Reuter model, instead of specifying a uniform, constant Me/L_{fi} , every cell can be assigned its own (local) Me/L_{fi} . An example of an advantage that this could provide is that the reduced interfacial area between water and air near water inlet, discussed in Section 5.3, can be taken into consideration by assigning a lower Me/L_{fi} in this region.

The inlet G_w (boundary conditions) may also be specified as a constant per cell instead of as a universal constant (this may cause complications with the forward iteration scheme, but with the backward iteration scheme in crossflow it will be straightforward). If the redistribution of water within the fill is measured experimentally, it can be incorporated into the computer program by an adapted interpolation scheme for G_w .

Adapting the numerical implementation of the Reuter model in this way would improve the comparability of the model predictions to experimental results and thereby enable a better validation of the Reuter model.

The variations in air velocity and pressure within the crossflow test section are expected to be small enough to not have a significant effect on the simulation results. Investigating the validity of this assumption by solving the air pressure and velocity fields simultaneously with the other equation in the Reuter model may also be considered.

6.5.3. More fill tests

Future researchers at Stellenbosch University can take advantage of the improvements made to the crossflow test facility during this project and use the crossflow test facility with the counterflow test facility to perform performance comparable tests on additional types and designs of fill.

Note that it is recommended that the procedure to determine correction factors for the thermocouples (Section 3.6.2) is repeated from time to time during future use of the facility in order to pick up and eliminate new inaccuracies that may develop in the thermocouple measurement system over time.

6.5.4. Investigate the testing of splash fill in the counterflow test section

Bertrand (2011) concluded that the present counterflow facility is poorly suited for measuring the performance characteristics of splash fill due to excessive migration of water to the test section walls. It would be highly advantageous if this problem could be resolved so that splash fill can also be tested in counterflow, since this would make it possible to conduct performance comparable counterflow and crossflow tests on splash fill as well.

6.5.5. Further improvement of crossflow test facility

- Investigate and implement ways to eliminate the undesirable gap between the fill and the water distribution system during trickle fill tests. This could be done by raising the water distribution spray frame while fill is being packed and to then lower it, or by designing a clamp-like mechanism, with which the fill, or a portion of the fill, can be compressed while being packed.
- Investigate and implement ways to further improve water distribution by the spray frame in the test section, particularly the zone with lower flow at the air outlet side. Opening and cleaning the water distribution spray frame may be a good first step.
- Install a bigger or a second drain pump so that higher water mass velocities can be used during fill tests (there is plenty of spare pump capacity in the water supply side).

6.5.6. Investigate the water redistribution by a trickle fill in the crossflow test section

In Chapter 5, it was concluded that the distribution of water within a trickle fill should ideally be measured when a trickle fill is tested in the crossflow test section. This is more difficult than in the counterflow test section because the space beneath the crossflow test section is very restricted. The equipment that was manufactured during this project to measure the distribution of water by the spray frame could be used to do this, but only if just the top half of the test section is packed with fill. Alternative methods should therefore also be considered.

6.5.7. Measure splashing drop sizes during a crossflow rain zone test

The polydisperse drop distribution of the drops near the bottom of the crossflow test section needs to be experimentally determined in order to accurately model the rain zone. Ways to decrease the amount of splashing should also be investigated and considered.

7. REFERENCES

- Al-Waked, R. 2010. *Crosswinds effect on the performance of natural draft wet cooling towers*. International Journal of Thermal Sciences. Vol. 49. Issue 1. p. 218-224.
- Al-Waked, R. & Behnia, M. 2006. *CFD simulation of wet cooling towers*. Applied Thermal Engineering. Vol. 26, Issue 4. p. 382-395.
- Al-Waked R. & Behnia, M. 2007. *Enhancing performance of wet cooling towers*. Energy Conversion and Management. Vol. 48, Issue 10. p. 2638-2648.
- American Society of Heating, Refrigeration and Air Conditioning (ASHRAE). 1975. *Laboratory methods of testing fans for rating*. Standard 51-75. ASHRAE. New York
- Banda, K. 2008. *Standard test procedure for measuring crossflow cooling tower fill characteristics*. M.Eng thesis. Stellenbosch University. South Africa.
- Berman, LD. 1961. *Evaporative cooling of circulating water*. Pergamon Press. New York.
- Bertrand, T.P. 2011. *Evaluation of a 1.5 x 1.5 m² counter-flow fill performance test facility with a view to contributing to a fill performance standard*. MSc Thesis. Stellenbosch University. South Africa.
- Bosnjakovic, F. 1965. *Technische Thermodynamik*. Theodor Steinkopf. Dresden.
- British Standard. 1988. *Water cooling towers, Part 2, Methods of performance testing*. BS 4485, British Standards Institution.
- Carbon-power. [S.a.]. [online], available: <http://www.fotocommunity.de/pc/pc/display/20289681>. [2011, 22 November]
- CTI (Cooling technology institute). 2000. *Acceptance test code for water cooling towers*. CTI Code ACT-105 (2000), Houston.
- De Villiers, E., 1999, *Heat, mass and momentum transfer in the rain zone of a cooling tower*, Stellenbosch University. MSc Thesis. South Africa.
- Dreyer, A.A. 1994. *Modelling of cooling tower splash pack*. Stellenbosch University. PhD Thesis. South Africa.
- Duss, A. 2009. *Critical investigation of a crossflow fill test facility*. Final year undergraduate project. Stellenbosch University. South Africa
- Eastop, T.D. & McConkey, A. 1993. *Applied Thermodynamics*. 5th Edition. Pearson Education Limited. England
- Energies renouvelables. *Worldwide electricity production from renewable energy sources: stats and figures series Twelfth Inventory - Edition 2010*. [online]. Available: <http://www.energies-renouvelables.org/observ-er/html/inventaire/pdf/12e-inventaire-Chap01-Eng.pdf>. [2011, 22 September]

- Gudmundsson, Y. 2012. *Performance evaluation of wet-cooling tower fills with CFD*. MSc Thesis. Stellenbosch University. South Africa
- Gunn, R. & Kinzer, G.D. 1948. *Terminal velocity of fall for water droplets in stagnant air*. US Weather Bureau. Washington D.C.
- Incorpera, F.P & DeWitt, D.P. 1996. *Fundamentals of heat and mass transfer*. 4th Edition. John Wiley and Sons Inc.
- Jaber, H. & Webb R.L. 1989. *Design of cooling towers by the effectiveness-NTU method*. ASME J. Heat Transfer. 111. p. 837–843.
- Klimanek, A., Ryszard, A., Bialeckia & Ziemowit Ostrowskia. 2010. *CFD two-scale model of a wet natural draft cooling tower*. Numerical Heat Transfer. Vol. 57. Issue 2.
- Klimanek, A. & Bialecki, R.A. 2009. *Solution of heat and mass transfer in counterflow wet-cooling tower fills*. Institute of Thermal Technology. Silesian University of Technology, Konarskiego 22. 44-100 Gliwice. Poland.
- Klimanek, A. & Bialecki, R.A. 2008. *On a numerical model of a natural draught wet-cooling tower*. Archives of Thermodynamics. Vol. 29. No. 4. p. 63-72.
- Kloppers, J.C. & Kröger, D.G. 2005. *Cooling tower performance evaluation: Merkel, Poppe, and e-NTU methods of analysis*. Journal for Engineering of Gas Turbines and Power. Vol. 127. Issue 1. p.1-7.
- Kröger, D.G. 2004. *Air-cooled heat exchangers and cooling towers – thermal-flow performance evaluation and design*. PennWell Corporation, Oklahoma.
- LeClair B.P., Hamielec, A.E., Pruppacher, H.R. & Hall, W.D. 1972. *A theoretical study of the internal circulation in water drops falling at terminal velocity in air*. Journal of Atmospheric Sciences, Vol. 29, p. 728-740.
- Merkel, F. 1925. *Verdunstungskühlung*. VDI-Zeitschrift. Vol. 70, p. 123–128.
- Poppe, M. & Rögener, H. 1991. *Berechnung von Rückkühlwerken*. VDIWärmeatlas. p. Mi 1–Mi 15.
- Ranz, W.E. & Marshall Jr. W.R. 1952. *Evaporation from drops*. Chemical Engineering Progress. Vol. 48. No. 3.
- Reuter, H.C.R. 2010. *Performance evaluation of natural draught cooling towers with anisotropic fills*. PhD Thesis. Stellenbosch University. South Africa.
- Roache, P. 1997. *Qualification of uncertainty in computational fluid dynamics*. Annual Review of Fluid Mechanics. Vol. 29. p. 123-160.
- Shafiee, S. & Topal, E. *When will fossil fuel reserves be diminished?* Energy Policy. Vol. 37. Issue 1. p.181-189.
- Terblanche, R. 2008. *Investigation of performance enhancing devices for the rain zones of wet cooling towers*. MSc Thesis. Stellenbosch University. South Africa.
- Turton, R. Levenspiel, O. 1986. *A short note on the drag correlation for spheres*. Powder technology. Vol. 47. p.83-86.

Williamson, N., Behnia, M. & Armfield, S.W. 2008a. *Thermal optimization of a natural draft wet cooling tower*. International Journal of Energy Research. Vol. 32. Issue 14. p. 1349–1361.

Williamson, A., Behnia, M. & Armfield, S. 2008b. *Comparison of a 2D axisymmetric CFD model of a natural draft wet cooling tower and a 1D model*. International Journal of Heat and Mass Transfer. Vol. 51. Issues 9-10. p. 2227-2236.

Williamson, N., Armfield, S. & Behnia, M. 2008c. *Numerical simulation of flow in a natural draft wet cooling tower – The effect of radial thermofluid fields*. Applied Thermal Engineering. Vol. 28. Issues 2-3. p. 178-189.

APPENDIX A: Sample calculations

A.1. Notes

The sample equations were created using Mathcad©. By performing the sample calculations directly in Mathcad©, consistency between the equations, the inputs and the outputs are guaranteed. This would not have been possible if the sample calculations were, like the equations in the main text, created using MS Word. Unfortunately Mathcad© has some formatting restrictions and it is therefore unavoidable to deviate from some of the conventions in equation format in the main text.

A.2. Movement, mass- and heat transfer from a single drop falling through an oblique air stream

A drop falling through an oblique air stream, illustrated in Figure A.1, with the parameters listed below, is considered. These particular parameters are chosen for the sample case because of their similarities with the experimental tests. An air angle of 45° is selected because no sample calculation was found in literature of a drop in cross-counterflow.

Drop diameter	$d_d = 0.0042 \text{ m}$
Initial drop velocity horizontal component	$v_{dx} = 0.1850 \text{ m/s}$
Initial drop velocity vertical component	$v_{dz} = -0.5084 \text{ m/s}$
Initial drop temperature	$T_d = 40 + 273.15 \text{ K}$
Air velocity horizontal component	$v_{ax} = 1.1597 \text{ m/s}$
Air velocity vertical component	$v_{ay} = 1.1597 \text{ m/s}$
Atmospheric pressure	$p_{am} = 101325 \text{ Pa}$
Air drybulb temperature	$T_a = 15 + 273.15 \text{ K}$
Air wetbulb temperature (relative humidity is therefore 60%)	$T_{wb} = 10.853 + 273.15 \text{ K}$
Gravitational acceleration	$g = -9.81 \text{ m}\cdot\text{s}^{-2}$

SOLUTION

Throughout this calculation, methods and correlations consistent to those provided in Section 2.3 are used.

Note that, because of technical constraints, the variable y is sometimes used to refer to the z -direction. Also, a '1' is sometimes added with variables in order to distinguish them from MathCad© functions, e.g. ρ_{av} as a property is written as ρ_{av1} , because ρ_{av} is a defined as a function in MathCad©.

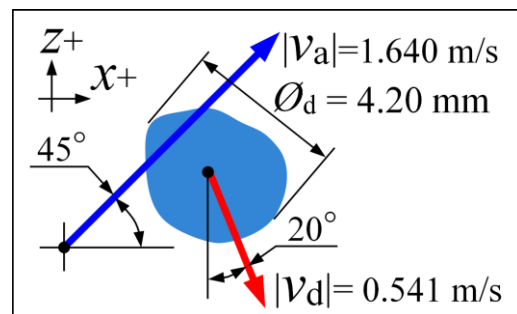


Figure A.1: Parameters of single drop case that is used in the sample calculation

Thermophysical properties

The thermophysical properties of the drop, the air and the film are calculated with the equations provided by Kröger (2004).

$$\text{Drop density: } \rho_d = \rho_w(T_d)$$

$$\rho_d = 992.33 \text{ kg}\cdot\text{m}^{-3}$$

$$\text{Drop surface tension: } \sigma_d = \sigma_w(T_d)$$

$$\sigma_d = 0.0696 \text{ N/m}$$

$$\text{Air humidity ratio: } \omega = w(T_a, T_{wb}, p_{atm}, p_v(T_{wb}))$$

$$\omega = 0.006416 \text{ kg/kg}$$

$$\text{Air density: } \rho_{avl} = \rho_{av}(\omega, p_{atm}, T_a)$$

$$\rho_{avl} = 1.2202 \text{ kg}\cdot\text{m}^{-3}$$

$$\text{Air dynamic viscosity: } \mu_{avl} = \mu_{av}(T_a, \omega)$$

$$\mu_{avl} = 17.854 \times 10^{-6} \text{ kg}\cdot\text{m}^{-1}\cdot\text{s}^{-1}$$

$$\text{Air-vapor specific heat: } c_{pavl} = c_{pav}(T_a, \omega)$$

$$c_{pavl} = 1012.13 \text{ J/kg}$$

$$\text{Saturated humidity ratio: } \omega_s = w(T_a, T_a, p_{atm}, p_v(T_a))$$

$$\omega_s = 0.01069 \text{ kg/kg}$$

The film temperature is defined as

$$\text{Film temperature: } T_f = \frac{T_a + T_d}{2}$$

$$T_f = 300.65 \text{ K}$$

Film humidity ratio is the same as the free humidity ratio:

$$\omega_f = \omega$$

$$\text{Density in film: } \rho_{av,f} = \rho_{av}(\omega_f, p_{atm}, T_f)$$

$$\rho_{av,f} = 1.169 \text{ kg}\cdot\text{m}^3$$

$$\text{Film dynamic viscosity: } \mu_{av,f} = \mu_{av}(T_f, \omega_f)$$

$$\mu_{av,f} = 18.430 \times 10^{-6} \text{ kg}\cdot\text{m}^{-1}\cdot\text{s}^{-1}$$

$$\text{Film specific heat: } c_{p.av,f} = c_{pav}(T_f, \omega_f)$$

$$c_{p.av,f} = 1012.584 \text{ J/kg}$$

$$\text{Film conduction coefficient: } k_{av,f} = k_{av}(T_f, \omega_f)$$

$$k_{av,f} = 26.206 \times 10^{-3} \text{ J}\cdot\text{m}^{-1}\cdot\text{K}^{-1}$$

$$\text{The gas constant for water vapor is defined as } R_v = \frac{8.31447}{0.018}$$

$$R_v = 461.915 \text{ J}\cdot\text{kg}^{-1}\cdot\text{K}^{-1}$$

Drop motion

The components of velocity of the drop relative to the air are calculated by vector addition.

$$x\text{- component: } v_{ad,x} = v_{ax} - v_{dx}$$

$$v_{ad,x} = 0.9740 \text{ m/s}$$

$$z\text{- component: } v_{ad,z} = v_{az} - v_{dz}$$

$$v_{ad,z} = 1.6677 \text{ m/s}$$

$$\text{Magnitude: } v_{ad,mag} = \sqrt{v_{ad,x}^2 + v_{ad,z}^2}$$

$$v_{ad,mag} = 1.9312 \text{ m/s}$$

The drop volume and mass are calculated:

$$\text{Drop volume: } V_d = \pi \cdot \frac{d_d^3}{6}$$

$$V_d = 38.792 \times 10^{-9} \text{ m}^3$$

$$\text{Drop mass: } M_d = \rho_d \cdot V_d$$

$$M_d = 38.495 \times 10^{-6} \text{ kg}$$

The terminal velocity of a drop is determined by iteratively solving the forces equilibrium equation, while using Dreyer's (1994) method with $E = E_T$ to determine the drag force. (Note that Dreyer's equation is strictly only applicable for vertically falling drops.)

The answer, as obtained through a numerical solver, is $v_T = 8.61689 \text{ m/s}$

The weight and buoyancy of the drop is given by:

Drop weight: $F_W = M_d g$ $F_W = -377.636 \times 10^{-6} \text{ N}$

Drop buoyancy: $F_B = -\rho_{avl} \cdot V_d g$ $F_B = 464.335 \times 10^{-9} \text{ N}$

The drag coefficient of a sphere of equal volume to the drop will be required in order to calculate the drag force on the drop. Therefore, the diameter of such a sphere must be calculated.

Sphere diameter: $d_S = 2 \cdot \sqrt[3]{\frac{3 \cdot V_d}{4 \cdot \pi}}$ $d_S = 0.004 \text{ m}$

The Reynolds number of the sphere in the air will then be

Sphere Reynolds number: $Re_S = \frac{\rho_{avl} \cdot d_S \cdot v_{ad.mag}}{\mu_{avl}}$ $Re_S = 554.34$

The drag coefficient of the sphere, according to Turton and Levenspiel (1986), is given by

$$C_{DS} = \frac{24}{Re_S} \cdot \left(1 + 0.173 Re_S^{0.657}\right) + \frac{0.413}{1 + 16300 Re_S^{-1.09}} \quad C_{DS} = 0.5422$$

Dreyer's (1994) method of determining the drag coefficient of a drop is now used:

Eotvos number: $Eo = \frac{(\rho_d - \rho_{avl}) \cdot |g| \cdot d_S^2}{\sigma_d}$ $Eo = 2.4637$

Drop deformation at terminal velocity: $E_T = \frac{1}{1 + 0.148 Eo^{0.85}}$ $E_T = 0.75844$

The deformation of an accelerating drop: $E = 1 - \left(\frac{v_{ad.mag}}{v_T}\right)^2 \cdot (1 - E_T)$ $E = 0.98787$

Drop drag coefficient:

$$C_D = C_{DS} \cdot \left[1.0 - 0.17185(1 - E_T) + 6.692(1 - E_T)^2 - 6.605(1 - E_T)^3\right] \quad C_D = 0.68092$$

The frontal area of the drop is calculated from the drop deformation:

Drop frontal area: $A_{fr} = \pi \cdot \left(\frac{d_S}{2} \cdot E^{\frac{-1}{3}}\right)^2$ $A_{fr} = 13.968 \times 10^{-6} \text{ m}^2$

The drag force is now found from the definition:

$$\text{Drag force on drop: } F_D = 0.5 C_D \cdot \rho_{av1} \cdot v_{ad.mag}^2 \cdot A_{fr} \quad F_D = 21.641 \times 10^{-6} \text{ N}$$

The direction of the drag force is opposite to the velocity of the drop relative to the air.

$$\text{Air direction } \theta_{ad} = \text{atan2}(v_{ad.z}, v_{ad.x}) \quad \theta_{ad} = 0.529 \text{ rads}$$

$$x\text{- component of drop drag force: } F_{Dx} = \cos(\theta_{ad}) \cdot F_D \quad F_{Dx} = 18.687 \times 10^{-6} \text{ N}$$

$$z\text{- component of drop drag force: } F_{Dy} = \sin(\theta_{ad}) \cdot F_D \quad F_{Dy} = 10.914 \times 10^{-6} \text{ N}$$

The drop lift force is assumed to be zero.

All forces have now been determined and the sum of forces is taken to determine the acceleration of the drop:

$$\text{Horizontal acceleration } a_x = \frac{(F_{Dx})}{M_d} \quad a_x = 0.4854 \text{ m} \cdot \text{s}^{-2}$$

$$\text{Vertical acceleration } a_z = \frac{(F_W + F_B + F_{Dy})}{M_d} \quad a_z = -9.5144 \text{ m} \cdot \text{s}^{-2}$$

A discrete time step of $\Delta t = 0.1$ second is now used to calculate the next position of the drop, assuming the current position is $x_0 = 0$ and $y_0 = 0$ (in the MathCad© formulas y is used instead of z , because z is defined as a function elsewhere):

$$\text{Average drop } x\text{- velocity during time step: } v_{avg.x} = v_{dx} + 0.5 a_x \cdot \Delta t \quad v_{avg.x} = 0.20937 \text{ m/s}$$

$$\text{Average drop } z\text{- velocity during time step: } v_{avg.z} = v_{dz} + 0.5 a_z \cdot \Delta t \quad v_{avg.z} = -0.98428 \text{ m/s}$$

$$\text{New } x\text{- position of drop: } x_I = x_0 + v_{avg.x} \cdot \Delta t \quad x_I = 0.02094 \text{ m}$$

$$\text{New } z\text{- position of drop: } y_I = y_0 + v_{avg.z} \cdot \Delta t \quad y_I = -0.098428 \text{ m}$$

$$\text{New } x\text{- velocity of drop: } v_{dxI} = v_{dx} + a_x \cdot \Delta t \quad v_{dxI} = 0.23364 \text{ m/s}$$

$$\text{New } z\text{- velocity of drop: } v_{dzI} = v_{dz} + a_z \cdot \Delta t \quad v_{dzI} = -1.46000 \text{ m/s}$$

This procedure may now be repeated for additional time steps. If mass transfer is taken into account the procedure below must be completed with this one at each time step.

Heat and mass transfer between the drop and the air

The following dimensionless numbers are determined from the air-, drop and film thermophysical properties.

$$\text{Film Reynolds number: } Re_f = \frac{\rho_{av.f} \cdot d_S \cdot v_{ad.mag}}{\mu_{av.f}} \quad Re_f = 514.663$$

$$\text{Film Prandtl number: } Pr_f = \frac{c_{p.av.f} \mu_{av.f}}{k_{av.f}} \quad Pr_f = 0.71214$$

Average Nusslet number according to Ranz and Marshall (1952):

$$Nu_{avg} = 2 + \left(0.6 Re_f^{\frac{1}{2}} \cdot Pr_f^{\frac{1}{3}} \right) \quad Nu_{avg} = 14.155$$

The convection coefficient may be determined from the definition of the Nusselt number.

$$\text{Convection coefficient: } h = \frac{Nu_{avg} \cdot k_{av.f}}{d_d} \quad h = 88.323 \text{ J} \cdot \text{m}^{-2} \cdot \text{K}^{-1}$$

To find the mass transfer coefficient, the diffusion coefficient is required. This is found using Fuller's (1966) correlation. In Fuller's correlation, the following values are used for the constants:

The molecular masses of air and water are and

$$M_a = 28.958 \text{ and } M_v = 18.010 \\ E\Delta_{va} = 19.7 \text{ and } E\Delta_{vb} = 13.1$$

Fuller's correlation is then

$$D = 0.0143 \frac{\left(\frac{1}{M_a} + \frac{1}{M_v} \right)^{0.5} \cdot T_a^{1.75}}{\sqrt{2} \cdot \left(E\Delta_{va}^{0.333} + E\Delta_{vb}^{0.333} \right)^2 \cdot p_{atm}} \quad D = 2.363 \times 10^{-5}$$

The Schmidt number is defined as

$$Sc = \frac{\mu_{av.f}}{\rho_{av.f} \cdot D} \quad Sc = 0.66690$$

The Sherwood number, according to Ranz and Marshall (1952), is defined as

$$Sh = 2 + 0.6 Re_f^{\frac{1}{2}} \cdot Sc^{\frac{1}{3}} \quad Sh = 13.892$$

The mass transfer coefficient h_D is calculated from the Sherwood number as

$$h_D = \frac{Sh \cdot D}{d_d} \quad h_D = 0.078168 \text{ m/s}$$

The mass convection coefficient (mass base) h_d is calculated according to the relationship between h_d and h_D in Eq. (2.52).

$$h_d = \frac{h_D \cdot p_{atm}}{R_v \cdot (\omega_{sw} - \omega)} \cdot \left[\frac{\omega_{sw}}{(\omega_{sw} + 0.622) \cdot T_d} - \frac{\omega}{(\omega + 0.622) \cdot T_a} \right] \quad h_d = 0.079621 \text{ kg} \cdot \text{m}^{-2} \cdot \text{s}^{-1}$$

where $\omega_{sw} = w(T_d, T_d, p_{atm}, p_v(T_d))$

$$\omega_{sw} = 0.0491037 \text{ kg/kg}$$

In order to deal with evaporation, some thermophysical properties must be determined through the use of Kroger's (2004) equations and the ideal gas laws.

Vapor pressure at film: $p_{vap.f} = p_v(T_d)$

$$p_{vap.f} = 7377.141 \text{ Pa}$$

Vapor density at film: $\rho_{vap.f} = \rho_v(T_d)$

$$\rho_{vap.f} = 0.051159 \text{ kg} \cdot \text{m}^{-3}$$

Specific heat of drop: $c_{p.d} = c_{pw}(T_d)$

$$c_{p.d} = 4.177 \times 10^3 \text{ J} \cdot \text{kg}^{-1} \cdot \text{K}^{-1}$$

Latent heat of evaporation from drop: $i_{fg.d} = i_{fg}(T_d)$

$$i_{fg.d} = 2.4069 \times 10^6 \text{ J/kg}$$

Free stream vapor pressure: $p_{v.fs} = p_v(T_a)$

$$p_{v.fs} = 1704.136 \text{ Pa}$$

Free stream vapor density: $\rho_{vap.fs} = \frac{p_{v.fs}}{R_v \cdot T_a}$

$$\rho_{vap.fs} = 0.012803 \text{ kg} \cdot \text{m}^{-3}$$

The outside area of the drop may be approximated with that of a sphere of equal volume as

Outside area (approximation) of drop $A_S = \pi \cdot d_S^2$

$$A_S = 55.418 \times 10^{-6} \text{ m}^2$$

The convective heat loss from the drop is calculated from the definition of the convection coefficient as

$$q_{conv} = h \cdot A_S \cdot (T_d - T_a)$$

$$q_{conv} = 0.12237 \text{ J}$$

The rate of evaporation is calculated from the definition of the mass convective coefficient:

$$m_{evap} = h_d \cdot A_S \cdot (\rho_{vap.f} - \rho_{vap.fs})$$

$$m_{evap} = 169.242 \times 10^{-9} \text{ kg/s}$$

The net mass transfer in the time step is

$$m_{lost} = m_{evap} \cdot \Delta t$$

$$m_{lost} = 16.924 \times 10^{-9} \text{ kg}$$

The net energy transferred during the time step is calculated as

Net convective energy transfer: $Q_{conv} = q_{conv} \cdot \Delta t$

$$Q_{conv} = 0.012237 \text{ J}$$

Net latent energy: $Q_{evap} = m_{lost} i_{fg.d}$

$$Q_{evap} = 0.040735 \text{ J}$$

The temperature and mass of the drop for the next time step is calculated as

$$\text{New drop temperature: } T_I = T_d - \frac{Q_{conv} + Q_{evap}}{c_{p.d} M_d}$$

$$T_I = 312.82 \text{ K}$$

$$T_I^{\circ\text{C}} = T_I - 273.1$$

$$T_I^{\circ\text{C}} = 39.671 \text{ }^{\circ}\text{C}$$

New drop mass: $M_I = M_d - m_{lost}$

$$M_I = 38.478 \times 10^{-6} \text{ kg}$$

Change in temperature: $\Delta T = T_d - T_I$

$$\Delta T = 0.32946 \text{ K}$$

Change in mass: $\Delta M = M_d - M_I$

$$\Delta M = 16.924 \times 10^{-9} \text{ kg}$$

A Merkel number for the drop is calculated from the definition of the Merkel number, which is given by $Me = h_d A/m$. The mass flow of the drop may be defined as the mass

of the drop divided by the time that it takes to "cross" the given (vertical) distance, and A is merely the surface area of the drop. Therefore

$$Me_d = \frac{h_d \cdot A_S \cdot \Delta t}{M_d} \quad Me_d = 0.011462$$

A.3. Calculation of m_{avo} from nozzle flow meters

The air volume flow rate is determined by measuring the average static pressure difference across three ASHRAE 51-75 elliptical nozzles that are installed in the wind tunnel. However, to accurately calculate the air-vapor mass flow rate through the nozzles, an iterative procedure is required. This procedure is briefly explained by means of a sample calculation.

Measured test conditions

Outlet air wetbulb temperature:	$T_{wbo_°C} = 30.868 \text{ °C}$	$T_{wbo} = 304.018 \text{ K}$
Inlet air drybulb temperature:	$T_{ai_°C} = 14.701 \text{ °C}$	$T_{ai} = 287.851 \text{ K}$
Inlet air wetbulb temperature:	$T_{wbi_°C} = 13.128 \text{ °C}$	$T_{wbi} = 286.278 \text{ K}$
Atmospheric pressure:		$p_{atm} = 100380 \text{ Pa}$
Fill pressure drop:		$dp_{fi} = 84 \text{ Pa}$
Nozzle pressure transducer voltage output:		$V_{noz} = 1.613 \text{ V}$

Geometry of tunnel and nozzle:

Nozzle diameter:	$d_n = 0.3 \text{ m}$
Duct area upstream of nozzles:	$A_{tus} = 4 \text{ m}^2$

PROCEDURE

It assumed that all the outlet air flows through the three nozzles in three equal streams. Therefore the complete outlet air-vapor mass flow rate is calculated as:

$$m_{avo} = 3 \cdot m_{avn} \quad (A1)$$

The pressure drop over one of the nozzles may be found by scaling the voltage signal from the pressure transducer with the equation that is provided by the pressure transducer's manufacturer.

$$dp_n = 2316.78787 \cdot v_{noz} - 2492.92$$

$$dp_n = 1.245 \times 10^3 \text{ Pa}$$

The equation to find the air-vapor mass flow rate through a single nozzle is taken from Kröger (2004) as

$$m_{avn} = C_n \cdot \phi_g \cdot Y \cdot A_n \cdot (2 \cdot \rho_n \cdot dp_n)^{0.5} \quad (\text{A2})$$

where the nozzle coefficient of discharge C_n is a function of the nozzle Reynolds number.

$$\text{For } 3 \cdot 10^4 < Re_n < 10^5$$

$$C_n = 0.954803 + 6.37817 \cdot 10^{-7} \cdot Re_n - 4.65394 \cdot 10^{-12} \cdot Re_n^2 \dots \\ + 1.33514 \cdot 10^{-17} \cdot Re_n^3$$

$$\text{For } 10^5 < Re_n < 3.5 \cdot 10^5$$

$$C_n = 0.9758 + 1.08 \cdot 10^{-7} \cdot Re_n - 1.6 \cdot 10^{-13} \cdot Re_n^2$$

$$\text{For } Re_n > 3.5 \cdot 10^5$$

$$C_n = 0.994$$

Kröger (2004) approximates the gas expansion factor ϕ_g as

$$\phi_g = 1 - \frac{3 \cdot dp_{noz}}{4 \cdot p_{ao} \cdot 1.4}$$

For a compressible fluid, Kröger (2004) gives the approach velocity as

$$Y = 1 + 0.5 \cdot \left(\frac{A_n}{A_{tus}} \right)^2 + 2 \cdot \left(\frac{A_n}{A_{tus}} \right)^2 \cdot \frac{dp_{noz}}{1.4 \cdot p_{ao}}$$

The air density in the nozzle ρ_n that appears in Eq. (A2) is, in this case, the outlet air density ρ_{avo} . However, the outlet air density is a (weak) function of the outlet air pressure. The outlet air pressure is calculated as

$$p_{ao} = p_{atm} - p_{dyn} - dp_{fi} \quad (\text{A3})$$

where the dynamic pressure is calculated as

$$p_{dyn} = \frac{1}{2} \cdot \rho_{avi} \cdot v_{ai}^2 \quad (\text{A4})$$

The inlet air velocity v_{ai} may be determined by assuming a constant dry air mass flow rate through the tunnel and then using the following relation:

$$v_{ai} = \frac{m_{avo} \cdot \frac{(1 + \omega_{ai})}{(1 + \omega_{ao})}}{\rho_{avi} \cdot A_{fr}} \quad (\text{A5})$$

The inlet air-vapor density ρ_{avi} and inlet air humidity ratio ω_{ai} that appear in Eq. (A5) are (weak) functions of inlet air pressure, which is calculated as

$$P_{ai} = P_{atm} - P_{dyn} \quad (A6)$$

The outlet air humidity ratio in Eq. (A5) is also a (weak) function of the outlet air pressure p_{ao} , which is defined in Eq. (A3).

Through Eq. (A1) to (A6), it becomes clear that the outlet air-vapor mass flow rate m_{avo} , the dynamic pressure p_{dyn} and the air-vapor densities and humidity ratios at both the inlet and outlet are all inter-dependent. It is therefore necessary to follow an iterative procedure with Equations (A1) to (A6) to determine these properties. Through an iterative search, the solution is determined as

$$m_{avo} = 11.10695 \text{ kg/s and } p_{dyn} = 3.06677 \text{ Pa}$$

When wall pressure taps are used, read note in Appendix B.2.

A.4. Calculation of EB , K_{fdm}/L_{fi} and Me/L_{fi} from crossflow test data

The following measurements are recorded during trickle fill test in straight crossflow configuration #101002-08 (see Table B.1).

Air inlet drybulb temperature	$T_{ai} = 14.701 + 273.15 \text{ K}$
Air inlet wetbulb temperature	$T_{wbi} = 13.128 + 273.15 \text{ K}$
Air outlet wetbulb temperature	$T_{wbo} = 30.868 + 273.15 \text{ K}$
Water inlet temperature	$T_{wi} = 44.274 + 273.15 \text{ K}$
Water outlet temperature	$T_{wo} = 30.868 + 273.15 \text{ K}$
Atmospheric pressure	$p_{atm} = 100380 \text{ Pa}$
Air-vapor mass flow rate	$m_{avo} = 11.108 \text{ kg/s}$
Water inlet mass flow rate	$m_{avo} = 8.643 \text{ kg/s}$
Pressure drop across fill	$dp_{fi} = 84 \text{ Pa}$

The dimensions of the fill volume are:

Depth along the tunnel axis:	$L_{fix} = 2.04 \text{ m}$
Tunnel vertical height:	$L_{fiz} = 2 \text{ m}$
Tunnel width:	$L_{fiy} = 2 \text{ m}$
The fill frontal area is $A_{fr} = L_{fiy} \cdot L_{fiz}$	$A_{fr} = 4 \text{ m}^2$
Gravitational acceleration is assumed to be $g = 9.81 \text{ m.s}^{-2}$	

SOLUTION

Calculating energy balance (EB)

Firstly, the thermophysical properties of the air and water at the inlet and outlet are determined. Due to inter-dependence between the air's thermophysical properties (the density in particular) and the dynamic pressure, the static air inlet pressure is determined through an iterative process.

A converged solution is reached when $p_{ai} = 100376.9$ Pa

By definition of the fill pressure drop, the static air pressure at the outlet is found:

$$p_{ao} = p_{ai} - dp_{fi} \quad p_{ao} = 100292.900 \text{ Pa}$$

With the static pressure, the dry- and wet bulb temperatures known, the other thermophysical properties of the air can be determined through the property formulae in Kroger (2004).

$$\text{Vapor pressure at air inlet: } p_{vai} = p_v(T_{wbi}) \quad p_{vai} = 1509.235 \text{ Pa}$$

$$\text{Vapor pressure at air outlet: } p_{vao} = p_v(T_{wbo}) \quad p_{vao} = 4458.610 \text{ Pa}$$

$$\text{Humidity ratio at air inlet: } \omega_i = w(T_{ai}, T_{wbi}, p_{ai}, p_{vai}) \quad \omega_i = 8.893 \times 10^{-3} \text{ kg/kg}$$

$$\text{Humidity ratio at air outlet: } \omega_o = w(T_{wbo}, T_{wbo}, p_{ao}, p_{vao}) \quad \omega_o = 29.089 \times 10^{-3} \text{ kg/kg}$$

Air-vapor enthalpies (specific per kg dry air)

$$\text{At air inlet: } i_{mai} = i_{ma}(T_{ai}, \omega_i) \quad i_{mai} = 37.287 \times 10^3 \text{ J/kg}$$

$$\text{At air outlet: } i_{mao} = i_{ma}(T_{wbo}, \omega_o) \quad i_{mao} = 105.524 \times 10^3 \text{ J/kg}$$

To determine the average specific heat of the inlet and outlet water, mean water temperatures need to be calculated:

$$T_{wim} = \frac{T_{wi}}{2} + 136.57. \quad T_{wim} = 295.287 \text{ K}$$

$$T_{wom} = \frac{T_{wo}}{2} + 136.57. \quad T_{wom} = 285.985 \text{ K}$$

The specific heats of the inlet and outlet air are evaluated at the mean temperatures:

$$c_{pwim} = c_{pw}(T_{wim}) \quad c_{pwim} = 4.183 \times 10^3 \text{ J/kg}$$

$$c_{pwom} = c_{pw}(T_{wom}) \quad c_{pwom} = 4.193 \times 10^3 \text{ J/kg}$$

An energy balance may now be calculated by constructing a control volume around the test section. The rate of evaporation can be determined through the difference in humidity ratio between the inlet and outlet air.

The mass flow rate of the dry air is calculated as

$$m_a = \frac{m_{avo}}{(1 + \omega_o)} \quad m_a = 10.7940 \text{ kg/s}$$

The evaporation rate is

$$m_{evap} = m_a \cdot (\omega_o - \omega_i) \quad m_{evap} = 0.21799 \text{ kg/s}$$

The rate of evaporation is deducted from the inlet water mass flow rate to find the outlet water mass flow rate.

$$m_{wo} = m_w - m_{evap} \quad m_{wo} = 8.42501 \text{ kg/s}$$

The rate of energy increase required to bring about the enthalpy change in the air is expressed as Q_a and is calculated as

$$Q_a = m_a \cdot (i_{mao} - i_{mai}) \quad Q_a = 736.552 \times 10^3 \text{ W}$$

The rate at which energy is extracted from the water is expressed as Q_w and is calculated as

$$Q_w = m_w \cdot c_{pwini} \cdot (T_{wi} - 273.15) - m_{wo} \cdot c_{pwom} \cdot (T_{wo} - 273.15) \quad Q_w = 693.942 \times 10^3 \text{ W}$$

The energy balance is then calculated as

$$EB = \frac{(Q_a - Q_w)}{Q_w} \cdot 100 \% \quad EB = 6.14022 \%$$

Loss coefficient per meter of fill

The air-vapor mass flow rate at for the inlet is calculated as

$$m_{avi} = m_a + \omega_i \cdot m_a \quad m_{avi} = 10.89 \text{ kg/s}$$

The outlet conditions are recalculated because the measured air outlet temperature is considered to be less reliable than the rest of the measurements taken.

The outlet enthalpy is recalculated from an energy balance:

$$i_{mao2} = \frac{Q_w}{m_a} + i_{mai} \quad i_{mao2} = 101.576 \times 10^3 \text{ J/kg}$$

Through an iterative procedure, a saturated outlet air temperature and pressure that correspond to the newly determined outlet enthalpy are found.

It is found to be $T_{ao2} = 29.752264 + 273.15 \text{ K}$ and $p_{ao2} = 100293.11 \text{ Pa}$

From the new outlet pressure, a new inlet pressure may be determined:

$$p_{ai2} = p_{ao2} + dp_{fi} \quad p_{ai2} = 100377.111 \text{ Pa}$$

Using the new pressure and temperature, the other outlet conditions are recalculated, using equations from Kröger (2004):

Vapor pressure at air outlet: $p_{vao2} = p_v(T_{ao2})$

$$p_{vao} = 4458.610 \text{ Pa}$$

Humidity ratio at air inlet: $\omega_{i2} = w(T_{ai}, T_{wbi}, p_{ai2}, p_{vai})$

$$\omega_{i2} = 0.008893 \text{ kg/kg}$$

Humidity ratio at air outlet: $\omega_{o2} = w(T_{ao2}, T_{ao2}, p_{ao2}, p_{vao2})$

$$\omega_{o2} = 0.027209 \text{ kg/kg}$$

Air-vapor density at air inlet: $\rho_{avi2} = \rho_{av}(\omega_{i2}, p_{ai2}, T_{ai})$

$$\rho_{avi2} = 1.2082 \text{ kg} \cdot \text{m}^{-3}$$

Air-vapor density at air outlet: $\rho_{avo2} = \rho_{av}(\omega_{o2}, p_{ao2}, T_{ao2})$

$$\rho_{avo2} = 1.1351 \text{ kg} \cdot \text{m}^{-3}$$

The dry air mass flow is recalculated as

$$m_{a2} = \frac{m_{avo}}{(1 + \omega_{o2})}$$

$$m_{a2} = 10.8138 \text{ kg/s}$$

The inlet air-vapor mass flow is recalculated as

$$m_{avi2} = m_{a2} \cdot (1 + \omega_{i2})$$

$$m_{avi} = 10.8900 \text{ kg/s}$$

The velocity of the outlet air-vapor is given by

$$v_{avo} = \frac{m_{avo}}{\rho_{avo2} \cdot A_{fr}}$$

$$v_{avo} = 2.4465 \text{ m/s}$$

The velocity of the inlet air-vapor is given by

$$v_{avi} = \frac{m_{avi2}}{\rho_{avi2} \cdot A_{fr}}$$

$$v_{avi} = 2.25745 \text{ m/s}$$

The mean air-vapor density is calculated as

$$\rho_{avm} = 2 \cdot \left(\frac{1}{\rho_{avi2}} + \frac{1}{\rho_{avo2}} \right)^{-1}$$

$$\rho_{avm} = 1.1705 \text{ kg} \cdot \text{m}^{-3}$$

The mean air-vapor mass flow rate is calculated as

$$m_{avm} = \frac{m_{avo} + m_{avi2}}{2}$$

$$m_{avm} = 11.009 \text{ kg/s}$$

The loss coefficient per fill length in terms of the mean air-vapor flow through the fill is then determined using Eq. (1.2):

$$K_{fdm_pLfi} = \frac{2 \cdot \left[dp_{fi} - \left(\rho_{avo2} \cdot v_{avo}^2 - \rho_{avi2} \cdot v_{avi}^2 \right) \right] \cdot \rho_{avm} \cdot \frac{A_{fr}^2}{m_{avm}}}{L_{fi}}$$

$$K_{fdm_pLfi} = 12.6292$$

Merkel number (e -NTU method) per meter of fill (Me_{e-NTU}/L_{fi})

The mean water temperature is calculated as

$$T_{wm} = \frac{T_{wi} + T_{wo}}{2}$$

$$T_{wm} = 308.122 \text{ K}$$

The mean pressure is calculated as

$$p_{a15} = \frac{(p_{ai} + p_{ao})}{2} \quad p_{a15} = 100.335 \times 10^3 \text{ Pa}$$

The humidity ratio of saturated air at the temperature of the outlet water, the inlet water and the mean water temperature is required. These are obtained by evaluating humidity ratio at the aforementioned temperatures:

$$\begin{aligned} p_{vswo} &= p_v(T_{wo}) & \omega_{swo} &= w(T_{wo}, T_{wo}, p_{a15}, p_{vswo}) & \omega_{swo} &= 0.021 \text{ kg/kg} \\ p_{vswi} &= p_v(T_{wi}) & \omega_{swi} &= w(T_{wi}, T_{wi}, p_{a15}, p_{vswi}) & \omega_{swi} &= 0.063 \text{ kg/kg} \\ p_{vswm} &= p_v(T_{wm}) & \omega_{swm} &= w(T_{wm}, T_{wm}, p_{a15}, p_{vswm}) & \omega_{swm} &= 0.037 \text{ kg/kg} \end{aligned}$$

To obtain the enthalpies at the temperature of the outlet water, the inlet water and the mean water temperature, the air-vapor enthalpy (specific per kg of dry air) is evaluated at the aforementioned temperatures, and the corresponding humidities from the previous step.

$$\begin{aligned} i_{maswo} &= i_{ma}(T_{wo}, \omega_{swo}) & i_{maswo} &= 79.971 \times 10^3 \text{ J/kg} \\ i_{maswi} &= i_{ma}(T_{wi}, \omega_{swi}) & i_{maswi} &= 208.409 \times 10^3 \text{ J/kg} \\ i_{maswm} &= i_{ma}(T_{wm}, \omega_{swm}) & i_{maswm} &= 130.354 \times 10^3 \text{ J/kg} \end{aligned}$$

The specific heat of water is calculated as

$$c_{pwm} = c_{pw}(T_{wm}) \quad c_{pwm} = 4.177 \times 10^3 \text{ J/kgK}$$

In the procedure that Kröger (2004) proposes, a correction factor, provided by Ber-
man (1961), is used to improve the approximation of i_{masw} . It is calculated as

$$\lambda = \frac{i_{maswo} + i_{maswi} - 2 \cdot i_{maswm}}{4} \quad \lambda = 6.918 \times 10^3$$

The approximate gradient of saturated air enthalpy curve over the control volume is

$$di_{dT_w} = \frac{i_{maswi} - i_{maswo}}{T_{wi} - T_{wo}} \quad di_{dT_w} = 6.904 \times 10^3$$

To determine the capacity ratio, the following comparison is made:

$$\begin{aligned} C_{min} &= \min \left(m_a, \frac{m_w \cdot c_{pwm}}{di_{dT_w}} \right) & C_{min} &= 5.229 \\ C_{max} &= \max \left(m_a, \frac{m_w \cdot c_{pwm}}{di_{dT_w}} \right) & C_{max} &= 10.794 \end{aligned}$$

The capacity ratio is then given by

$$C_e = \frac{C_{min}}{C_{max}} \quad C_e = 0.48448$$

The approximate maximum enthalpy transfer rate is expressed as

$$Q_{max} = C_{min} \cdot (i_{maswi} - \lambda - i_{mai})$$

$$Q_{max} = 858.698 \times 10^3 \text{ W}$$

The heat extracted from the water is calculated as

$$Q = c_{pwm} \cdot m_w \cdot (T_{wi} - T_{wo})$$

$$Q = 671.661 \times 10^3 \text{ W}$$

$$ef = \frac{Q}{Q_{max}}$$

$$ef = 782.185 \times 10^{-3}$$

NTU now needs to be solved as a function of ef . The function is

$$ef = 1 - \exp \left[NTU^{0.22} \frac{\left(\exp \left(-C_e \cdot NTU^{0.78} - 1 \right) \right)}{C_e} \right]$$

However, the relationship is very non-linear, and a consequently a numerical is used solve it.

The result is $NTU = 2.356$

Kröger (2004) provides the following relation between Me and NTU :

$$Me_{eNTU} = NTU \cdot \frac{C_{min}}{m_w}$$

$$Me_{eNTU} = 1.426$$

Therefore, the Merkel number per length fill is given by

$$Me_{eNTU_pLf} = \frac{Me_{eNTU}}{L_{fiz}}$$

$$Me_{eNTU_pLf} = 0.7129$$

APPENDIX B: Crossflow test results in table form

B.1. Notes

- A large volume of test results are presented rather than sample data sets because of two reasons:
 - (a) The generation of test results was an important objective in this thesis and the results themselves are therefore considered important.
 - (b) The experimental data may be useful to other researchers in the field of cooling tower improvement or related fields.
- Results from the following tests are presented:
 - (a) Trickle fill in straight crossflow configuration ($L_{fi,x} = 2$ m)
 - (b) Trickle fill orientated as if in counterflow, referred to as crossflow (counterflow config.)
 - (c) Rain zone tests
 - (d) Trickle fill in straight crossflow, but with $L_{fi,x} = 1.5$ m

The difference between the first two trickle fill configurations is illustrated in Figure B.1.

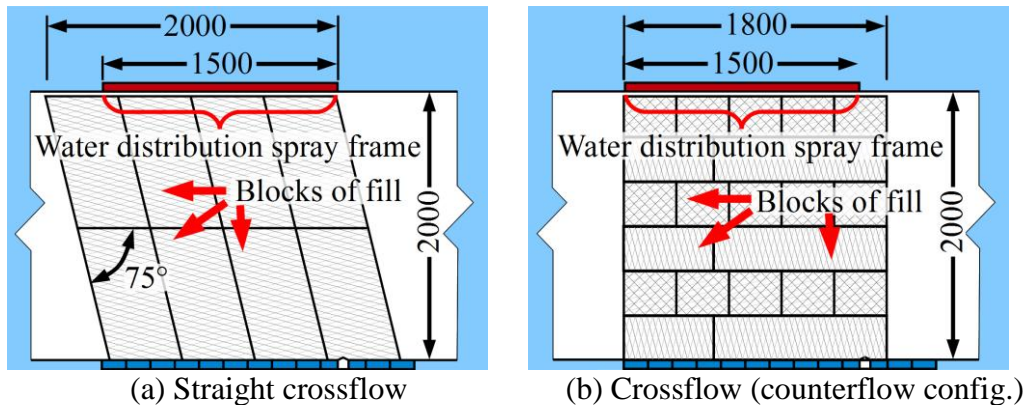


Figure B.1: Two configurations in which the trickle fill was tested

2 series of 16 tests each were done with the trickle fill configuration shown in Figure B.2. However, upon examining the test results and comparing them to those of the configuration shown in Figure B.1 (a), it was concluded that the edge effect of the “rain” that falls from the front part of the fill renders the results from those tests not performance comparable to the counterflow tests and for that reason the tests using this configuration are not mentioned in the main text.

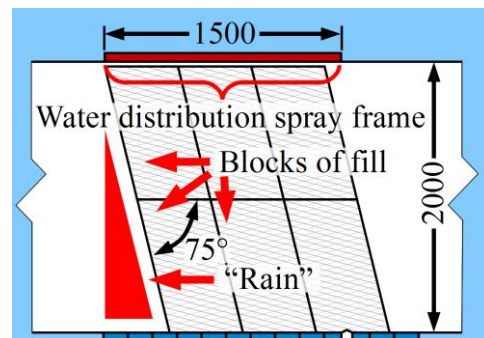


Figure B.2: Trickle fill in crossflow, $L_{fi,x} = 1.5$ m configuration

However, for the sake of enrichment, the results from one of these test series are also provided in this appendix.

- Dry tests were also conducted for the trickle fill tests. In the dry tests, there was no water flow and the objective was only to measure K_{fdm}/L_{fi} as a function of G_a for the dry fill. The results from a series of dry tests are also provided for each of the fill configurations.
- All values have been averaged from the recorded experimental data. The following quantities, calculated from the experimental data are also given:
 G_w , G_a , Me_{e-NTU}/L_{fi} , Me_R/L_{fi} , K_{fdm}/L_{fi} , EB and $T_{ao,R}$. Me_{e-NTU}/L_{fi} is the Merkel number per meter fill that is calculated using the e-NTU method of analysis (Jaber & Webb, 1989). Me_R/L_{fi} is the Merkel number per meter of fill calculated using the Reuter model as presented in Section 2.2. $T_{ao,R}$ is the mass and energy based average of the temperature at the air outlet.
- T_{wi} is repeated next to G_w and G_a for convenience when calculating Me/L_{fi} for the fill using the equations provided in Tables 4.2 and 4.3.
- If a * is reported for Δp_{fi} , it is because the pressure drop was not logged for that test.
- The crossflow test section's dimensions are $L \times H = 1.5 \times 2$ m, but the fill length L_{fi} in the air direction may be more than that. In the case of the trickle fill tests, L_{fi} in the air direction = 2 m unless otherwise stated.
- The data DVD accompanying this project contains MS Excel workbooks in which the following additional experimental data is provided for all tests (including the 3-layer crossflow tests mentioned above):
 - The non-averaged 'raw' data
 - The measured temperature profiles at the air and water outlets
 - All the statistical information discussed in Section 3.5.1
- Due to the large volume of data, tables are allowed to break across pages, but in such a case, the column headings are repeated at the top of the new page.
- For the data on the counterflow tests that are referred to during this study, see Bertrand (2011).

B.2. Important note regarding test results

Wall pressure taps were used for the air flow measurement. According to Duss (2009) a correction factor of 0.984 must be applied to the air flow rate determined from the wall mounted pressure tap measurements. Note that this correction factor was not applied in the calculation of the air-vapor mass flow rate of the results that are published below or that was used in the main text. This was only discovered after this document had already been finalized and revised. A decision needed to be made whether to apply the correction factor and re-do all the tables and graphs in this thesis and to then restart the revision process or whether to leave it as is and include this note.

The decision was made to leave the document as is, because the marginal difference in the experimentally recorded data would have no influence on the conclusions made in this thesis.

This note is therefore included for the benefit of future researchers who wish to use this test data.

B.3. Trickle fill in straight crossflow configuration

Table B.1: Trickle fill crossflow test results, Part 1

Test #	T_{ai} °C	T_{wbi} °C	T_{wi} °C	T_{wo} °C	m_{avo} kg/s	m_{wi} kg/s	Δp_{fi} Pa	T_{wbo} °C	p_a Pa
101002-01	17.053	13.782	52.161	26.619	5.376	4.451	19.0	35.524	100380
101002-02	16.921	13.560	51.592	24.095	7.031	4.340	31.0	32.663	100380
101002-03	16.669	13.368	49.713	21.155	9.768	3.993	57.0	28.413	100380
101002-04	14.683	13.270	47.694	20.948	11.233	4.496	75.0	27.193	100380
101002-05	14.886	13.443	47.304	32.458	4.878	8.498	18.5	38.823	100380
101002-06	14.579	13.194	45.976	28.735	7.232	8.581	36.5	35.269	100380
101002-07	14.501	13.096	45.031	26.831	9.768	9.052	66.0	32.785	100380
101002-08	14.701	13.128	44.274	25.670	11.108	8.643	84.0	30.868	100380
101002-09	14.909	13.359	41.898	33.222	5.109	13.264	20.0	36.395	100380
101002-10	14.855	13.282	41.733	30.801	7.132	13.181	39.0	34.763	100380
101002-11	14.894	13.192	41.668	29.156	9.596	13.159	74.5	32.600	100380
101002-12	15.921	13.576	41.598	28.335	11.110	13.159	98.5	31.659	100380
101002-13	16.398	13.988	41.612	33.748	4.847	14.198	*	37.020	100380
101002-14	15.693	13.614	41.496	31.330	7.055	14.153	*	35.133	100380
101002-15	15.427	13.473	40.374	29.090	9.946	14.160	83.5	32.066	100380
101002-16	15.185	13.339	38.274	27.487	11.069	14.212	112.0	30.232	100380
101003-01	14.641	12.784	35.827	25.860	11.007	13.135	99.0	27.774	100380
101003-02	14.224	12.550	33.673	22.578	11.175	8.789	87.5	24.507	100380
101003-03	14.223	12.393	32.847	18.350	11.311	4.457	76.0	20.768	100380
101003-04	14.154	12.345	32.768	24.922	9.475	13.241	75.0	26.364	100380
101003-05	14.338	12.618	32.114	22.587	9.592	8.767	64.5	24.440	100380
101003-06	14.277	12.539	31.628	18.528	9.737	4.384	56.0	21.016	100380
101003-07	14.012	12.526	30.974	25.344	6.907	13.404	38.5	27.004	100380
101003-08	14.128	12.492	30.214	22.828	7.148	9.017	36.0	25.044	100380
101003-09	13.330	11.891	29.445	18.344	7.279	4.205	32.0	21.284	100380
101003-10	13.390	12.000	27.944	24.227	4.892	12.877	20.0	25.633	100380
101003-11	13.199	11.963	26.466	21.859	4.916	8.957	18.0	23.677	100380
101003-12	13.115	11.967	25.912	18.676	4.956	4.349	16.0	21.225	100380
101003-13	13.386	12.052	25.792	20.585	11.271	13.983	103.0	21.349	100380
101003-14	13.345	12.133	25.119	20.826	9.652	14.094	*	21.453	100380
101003-15	13.359	12.080	24.696	21.291	7.019	14.036	40.0	22.082	100380
101003-16	13.129	12.035	24.690	22.052	5.077	14.111	22.0	22.703	100380
101003-01	14.641	12.784	35.827	25.860	11.007	13.135	99.0	27.774	100380

Test #	T_{ai} °C	T_{wbi} °C	T_{wi} °C	T_{wo} °C	m_{avo} kg/s	m_{wi} kg/s	Δp_{fi} Pa	T_{wbo} °C	p_a Pa
101003-02	14.224	12.550	33.673	22.578	11.175	8.789	87.5	24.507	100380
101003-03	14.223	12.393	32.847	18.350	11.311	4.457	76.0	20.768	100380
101003-04	14.154	12.345	32.768	24.922	9.475	13.241	75.0	26.364	100380
101003-05	14.338	12.618	32.114	22.587	9.592	8.767	64.5	24.440	100380
101003-06	14.277	12.539	31.628	18.528	9.737	4.384	56.0	21.016	100380
101003-07	14.012	12.526	30.974	25.344	6.907	13.404	38.5	27.004	100380
101003-08	14.128	12.492	30.214	22.828	7.148	9.017	36.0	25.044	100380
101003-09	13.330	11.891	29.445	18.344	7.279	4.205	32.0	21.284	100380
101003-10	13.390	12.000	27.944	24.227	4.892	12.877	20.0	25.633	100380
101003-11	13.199	11.963	26.466	21.859	4.916	8.957	18.0	23.677	100380
101003-12	13.115	11.967	25.912	18.676	4.956	4.349	16.0	21.225	100380
101003-13	13.386	12.052	25.792	20.585	11.271	13.983	103.0	21.349	100380
101003-14	13.345	12.133	25.119	20.826	9.652	14.094	*	21.453	100380
101003-15	13.359	12.080	24.696	21.291	7.019	14.036	40.0	22.082	100380
101003-16	13.129	12.035	24.690	22.052	5.077	14.111	22.0	22.703	100380
101014-01	14.136	10.937	49.740	31.264	10.788	13.831	97.0	36.729	100900
101014-02	14.173	10.926	47.468	31.259	9.896	13.882	84.0	35.995	100900
101014-03	14.236	11.044	45.630	32.748	7.141	13.864	42.0	37.795	100900
101014-04	14.296	11.014	44.475	34.848	4.902	13.872	20.5	39.478	100900
101014-05	13.421	10.695	42.882	28.210	10.947	13.134	98.0	32.190	100900
101014-06	13.264	10.541	39.945	27.794	9.748	12.947	78.0	30.987	100900
101014-07	13.443	10.713	38.566	28.741	7.080	12.880	40.5	32.270	100900
101014-08	13.468	10.601	37.639	30.177	4.913	12.872	21.0	33.431	100900
101014-09	13.411	10.710	36.979	23.312	11.150	9.025	87.0	26.082	100900
101014-10	13.348	10.558	36.275	23.809	9.414	9.015	63.5	26.711	100900
101014-11	13.470	10.568	35.531	24.927	6.989	9.019	35.0	28.289	100900
101014-12	13.424	10.568	34.527	26.154	5.087	9.042	20.0	29.540	100900
101014-13	13.099	10.461	34.040	17.375	11.365	4.325	74.0	20.063	100900
101014-14	13.428	10.687	33.175	17.878	9.360	4.313	51.0	20.815	100900
101014-15	13.374	10.695	32.678	18.731	7.212	4.320	31.5	22.314	100900
101014-16	13.354	10.676	32.200	20.159	5.171	4.272	16.5	24.204	100900

Table B.2: Test results for trickle fill in (straight) crossflow, Part 2

Test #	G_{wi} kg/m ² s	G_a kg/m ² s	T_{wi} °C	Me_{NTU}/L_{fi} m ⁻¹	Me_R/L_{fi} m ⁻¹	K_{fdm}/L_{fi} m ⁻¹	EB %	$T_{ao,avg,R}$ °C
101002-01	1.436	1.294	52.161	0.862	0.975	12.092	0.2	35.604
101002-02	1.400	1.703	51.592	1.066	1.123	11.569	2.5	32.431
101002-03	1.288	2.382	49.713	1.441	1.314	11.083	6.7	27.771
101002-04	1.450	2.744	47.694	1.304	1.292	11.062	4.8	26.771
101002-05	2.741	1.165	47.304	0.488	0.569	14.329	2.1	38.639
101002-06	2.768	1.742	45.976	0.622	0.724	12.891	3.2	30.620
101002-07	2.920	2.365	45.031	0.679	0.782	12.811	5.4	32.189

Test #	G_{wi} kg/m ² s	G_a kg/m ² s	T_{wi} °C	Me_{eNTU}/L_{fi} m ⁻¹	Me_R/L_{fi} m ⁻¹	K_{fdm}/L_{fi} m ⁻¹	EB %	$T_{ao,avg,R}$ °C
101002-08	2.788	2.699	44.274	0.713	0.814	12.629	6.1	30.223
101002-09	4.279	1.228	41.898	0.338	0.396	14.143	0.2	36.518
101002-10	4.252	1.720	41.733	0.454	0.518	14.172	0.4	34.840
101002-11	4.245	2.324	41.668	0.498	0.559	14.990	1.7	32.504
101002-12	4.245	2.695	41.598	0.531	0.598	14.774	2.1	31.520
101002-13	4.580	1.163	41.612	0.322	0.384	*	0.4	37.116
101002-14	4.565	1.700	41.496	0.424	0.488	*	1.0	35.129
101002-15	4.568	2.411	40.374	0.475	0.527	15.641	3.2	31.778
101002-16	4.585	2.692	38.274	0.512	0.566	16.983	4.3	29.834
101003-01	4.237	2.687	25.912	0.540	0.590	15.227	1.4	27.733
101003-02	2.835	2.740	29.445	0.700	0.772	13.112	2.7	24.339
101003-03	1.438	2.784	31.628	1.127	1.253	11.170	2.0	20.685
101003-04	4.271	2.317	32.847	0.514	0.567	15.608	-0.9	26.578
101003-05	2.828	2.352	26.466	0.678	0.743	13.117	1.7	24.369
101003-06	1.414	2.396	30.214	1.107	1.236	11.099	0.7	21.023
101003-07	4.324	1.688	32.114	0.416	0.472	15.076	4.2	26.667
101003-08	2.909	1.751	33.673	0.629	0.697	13.181	1.9	24.953
101003-09	1.356	1.791	27.944	1.087	1.216	11.367	2.0	20.489
101003-10	4.154	1.198	30.974	0.348	0.403	15.664	5.5	25.195
101003-11	2.889	1.206	32.768	0.537	0.619	13.985	1.7	23.622
101003-12	1.403	1.219	35.827	0.972	1.068	12.267	1.4	21.190
101003-13	4.511	2.773	24.690	0.576	0.632	15.262	0.5	21.414
101003-14	4.546	2.374	24.696	0.488	0.537	*	3.9	21.243
101003-15	4.528	1.725	25.119	0.416	0.471	15.280	3.8	21.875
101003-16	4.552	1.247	25.792	0.323	0.372	16.059	4.0	22.479
101014-01	4.462	2.591	32.200	0.478	0.554	15.524	3.0	36.415
101014-02	4.478	2.381	32.678	0.459	0.527	15.989	2.4	35.765
101014-03	4.472	1.711	33.175	0.413	0.471	15.330	3.7	37.366
101014-04	4.475	1.170	34.040	0.318	0.377	15.872	5.1	38.824
101014-05	4.237	2.654	34.527	0.524	0.591	15.306	3.8	31.791
101014-06	4.176	2.368	35.531	0.496	0.549	15.391	4.5	30.505
101014-07	4.155	1.716	36.275	0.454	0.516	15.122	2.6	32.037
101014-08	4.152	1.188	36.979	0.369	0.437	16.276	1.7	33.336
101014-09	2.911	2.728	37.639	0.681	0.758	13.176	3.8	25.758
101014-10	2.908	2.302	38.566	0.655	0.727	13.484	2.1	26.570
101014-11	2.909	1.705	39.945	0.614	0.680	13.456	1.0	28.279
101014-12	2.917	1.239	42.882	0.514	0.591	14.505	2.0	29.403
101014-13	1.395	2.800	44.475	1.165	1.292	10.871	0.1	20.117
101014-14	1.391	2.304	45.630	1.142	1.277	11.024	-3.2	21.160
101014-15	1.394	1.773	47.468	1.094	1.234	11.446	-3.5	22.730
101014-16	1.378	1.268	49.740	0.984	1.109	11.635	-2.1	24.518

Table B.3: Dry test results for trickle fill in (straight) crossflow

Test #	T_{ai} °C	T_{wbi} °C	m_{avo} kg/s	T_{wbo} °C	Δp_{fi} Pa	p_a Pa	G_a kg/m ² s	K_{fdm}/L_{fi} m ⁻¹
101015-01	13.909	10.897	3.850	10.423	8.5	100900	0.955	11.042

Test #	T_{ai} °C	T_{wbi} °C	m_{avo} kg/s	T_{wbo} °C	Δp_{fi} Pa	p_a Pa	G_a kg/m ² s	K_{fdm}/L_{fi} m ⁻¹
101015-02	14.029	10.901	4.808	10.284	13.5	100900	1.193	11.243
101015-03	13.828	10.980	5.578	10.441	16.0	100900	1.384	9.901
101015-04	13.758	10.935	6.983	10.390	24.5	100900	1.732	9.675
101015-05	14.308	10.990	7.949	10.465	31.0	100900	1.972	9.441
101015-06	14.141	10.934	9.235	10.433	40.5	100900	2.291	9.140
101015-07	14.170	10.987	11.100	10.433	57.5	100900	2.753	8.980
101015-08	14.015	10.946	11.719	10.370	63.5	100900	2.907	8.899

B.4. Trickle fill in crossflow (counterflow config)

Table B.4: Test results for trickle fill in crossflow (counterflow config.), Part 1

Test #	T_{ai} °C	T_{wbi} °C	T_{wi} °C	T_{wo} °C	m_{avo} kg/s	m_{wi} kg/s	Δp_{fi} Pa	T_{wbo} °C	p_a Pa
101209-01	15.877	13.882	48.601	28.042	4.072	4.545	26.0	37.191	100320
101209-02	15.749	13.817	47.476	23.914	6.398	4.597	60.0	32.665	100320
101209-03	15.916	13.897	46.962	21.748	8.648	4.822	108.0	30.308	100320
101209-04	16.140	14.022	46.279	19.946	10.904	4.716	169.0	28.102	100320
101209-05	15.329	13.651	45.353	32.976	4.350	9.369	32.0	39.360	100320
101209-06	15.574	13.722	44.492	29.204	6.523	9.331	68.0	36.448	100320
101209-07	15.779	13.931	43.603	26.972	8.414	9.412	110.0	34.390	100320
101209-08	15.154	13.581	42.525	24.168	10.792	9.058	178.0	31.766	100320
101209-09	27.371	19.805	33.597	30.051	4.171	13.684	31.0	31.390	100390
101209-10	27.752	19.948	37.014	30.825	6.089	13.941	63.0	33.341	100390
101209-11	27.842	19.966	34.981	28.108	8.539	13.724	122.5	30.859	100390
101209-12	27.735	19.889	34.363	26.764	10.381	13.733	181.0	29.682	100390
101210-01	19.208	17.178	52.012	29.719	4.317	4.779	27.0	39.036	100860
101210-02	19.138	17.152	51.014	26.259	6.248	4.716	55.0	35.533	100860
101210-03	19.070	17.098	49.927	23.366	8.479	4.712	95.5	32.502	100860
101210-04	19.008	17.072	49.427	22.452	10.937	4.733	163.0	30.307	100860
101210-05	19.023	17.035	48.235	34.339	4.424	9.541	31.0	42.302	100860
101210-06	19.180	17.125	47.502	30.970	6.302	9.488	60.0	39.650	100860
101210-07	18.991	17.048	46.472	28.142	8.391	9.474	106.0	37.077	100860
101210-08	18.777	16.942	45.623	25.855	10.812	9.420	174.0	34.739	100860
101210-09	19.076	17.035	43.891	35.470	4.533	13.905	36.0	40.852	100860
101210-10	18.964	16.999	42.936	32.757	6.232	13.890	66.0	38.818	100860
101210-11	18.772	16.923	41.343	29.707	8.513	13.833	121.0	36.127	100860
101210-12	18.625	16.854	40.253	27.608	10.794	13.862	192.0	34.080	100860
110412-01	18.011	16.172	32.449	28.770	4.150	13.969	28.0	29.682	100390
110412-02	18.183	16.250	32.163	27.071	6.176	13.924	62.0	29.352	100390
110412-03	17.766	16.054	31.646	25.446	8.356	13.824	114.0	28.007	100390
110412-04	17.151	15.720	30.768	23.739	10.673	13.750	186.0	26.483	100390
110412-05	18.409	16.421	27.417	24.000	4.200	9.305	27.0	25.774	100390

Test #	T_{ai} °C	T_{wbi} °C	T_{wi} °C	T_{wo} °C	m_{avo} kg/s	m_{wi} kg/s	Δp_{fi} Pa	T_{wbo} °C	p_a Pa
110412-06	18.117	16.322	27.309	22.628	6.188	9.264	57.0	24.984	100390
110412-07	18.260	16.389	27.029	21.608	8.093	9.240	98.0	24.200	100390
110412-08	17.978	16.314	26.471	20.533	10.428	9.151	159.0	23.073	100390
110412-09	18.102	16.385	26.268	20.983	4.324	4.622	26.5	23.606	100390
110412-10	17.828	16.277	25.933	19.617	6.137	4.581	51.5	22.330	100390
110412-11	17.704	16.229	25.848	18.699	8.393	4.607	95.0	21.368	100390
110412-12	17.403	16.094	25.582	18.000	10.530	4.594	149.0	20.567	100390
110413-01	18.587	16.760	38.290	26.750	10.918	13.750	196.0	32.410	100860
110413-02	18.570	16.738	37.323	28.041	8.455	13.754	118.5	32.908	100860
110413-03	18.766	16.843	36.712	29.568	6.205	13.905	65.0	33.668	100860
110413-04	18.711	16.813	36.091	30.811	4.478	13.968	35.5	34.089	100860
110413-05	18.483	16.714	35.686	23.305	10.953	9.310	177.5	29.068	100860
110413-06	18.503	16.717	35.373	24.559	8.665	9.295	112.0	29.851	100860
110413-07	18.572	16.743	34.874	26.406	6.115	9.236	56.5	31.033	100860
110413-08	18.736	16.788	34.338	27.988	4.377	9.204	30.0	31.839	100860
110413-09	18.482	16.664	33.955	20.140	10.413	4.675	145.5	24.653	100860
110413-10	18.616	16.732	33.860	20.882	8.418	4.693	96.0	25.542	100860
110413-11	18.420	16.580	33.650	22.282	6.193	4.666	53.0	26.798	100860
110413-12	18.638	16.683	33.333	23.976	4.432	4.628	27.5	28.111	100860
110414-01	18.702	16.759	32.804	22.831	4.824	4.380	32.0	27.513	101160
110414-02	18.264	16.551	32.058	19.467	9.528	4.385	*	23.916	101160
110414-03	18.264	16.551	32.058	19.467	9.522	4.385	119.5	23.916	101160
110414-04	18.288	16.575	31.724	18.861	11.157	4.385	165.5	23.033	101160
110414-05	18.150	16.464	30.967	25.264	4.849	8.767	35.0	28.409	101160
110414-06	18.131	16.471	30.469	23.410	6.948	8.741	70.0	27.092	101160
110414-07	17.970	16.412	30.094	21.772	9.542	8.729	131.5	25.757	101160
110414-08	17.902	16.386	29.749	21.001	11.140	8.727	178.0	24.928	101160
110414-09	18.066	16.472	29.400	25.889	4.807	13.062	37.0	27.787	101160
110414-10	18.000	16.460	29.040	24.371	7.099	12.988	80.0	26.844	101160
110414-11	18.001	16.479	28.769	23.154	9.450	12.958	141.5	25.942	101160
110414-12	17.789	16.395	28.401	22.299	11.070	12.991	192.5	25.249	101160
110414-13	17.819	16.400	27.932	24.801	5.195	13.860	43.5	26.517	101160
110414-14	17.765	16.404	27.657	23.816	6.982	13.831	79.0	25.807	101160
110414-15	17.568	16.312	27.389	22.591	9.579	13.816	148.5	25.001	101160
110414-16	17.610	16.332	27.073	21.996	11.104	13.813	197.5	24.365	101160

Table B.5: Test results for trickle fill in crossflow (counterflow config.), Part 2

Test #	G_{wi} kg/m ² s	G_a kg/m ² s	T_{wi} °C	Me_{eNTU}/L_{fi} m ⁻¹	Me_R/L_{fi} m ⁻¹	K_{fdm}/L_{fi} m ⁻¹	EB %	$T_{ao,avg,R}$ °C
101209-01	1.466	0.977	48.601	0.772	0.913	32.887	3.0	36.872
101209-02	1.483	1.549	47.476	1.066	1.203	30.811	2.0	32.502
101209-03	1.555	2.103	46.962	1.364	1.434	30.392	1.9	30.177
101209-04	1.521	2.660	46.279	1.852	1.673	29.954	3.3	27.843
101209-05	3.022	1.038	45.353	0.472	0.562	35.484	2.0	34.641
101209-06	3.010	1.567	44.492	0.647	0.759	33.543	3.1	36.131
101209-07	3.036	2.031	43.603	0.760	0.890	32.625	4.6	33.889
101209-08	2.922	2.618	42.525	0.941	1.094	32.173	5.5	31.197
101209-09	4.414	1.012	33.597	0.317	0.391	36.758	-22.0	31.697
101209-10	4.497	1.473	37.014	0.435	0.523	34.976	-11.7	33.728
101209-11	4.427	2.074	34.981	0.612	0.717	34.620	-9.9	31.268
101209-12	4.430	2.527	34.363	0.770	0.895	34.630	-12.8	30.369
101210-01	1.542	1.031	52.012	0.788	0.929	30.267	-1.0	39.300
101210-02	1.521	1.505	51.014	1.072	1.174	29.476	1.6	35.432
101210-03	1.520	2.054	49.927	1.726	1.532	27.835	0.9	32.491
101210-04	1.527	2.660	49.427	2.051	1.531	28.607	2.3	29.952
101210-05	3.078	1.047	48.235	0.542	0.661	33.105	1.1	42.286
101210-06	3.061	1.503	47.502	0.702	0.846	31.566	2.3	39.453
101210-07	3.056	2.014	46.472	0.873	1.040	31.486	3.2	36.779
101210-08	3.039	2.608	45.623	1.048	1.222	31.169	4.5	34.310
101210-09	4.485	1.077	43.891	0.355	0.440	36.643	6.2	40.101
101210-10	4.481	1.489	42.936	0.482	0.581	35.555	5.9	38.144
101210-11	4.462	2.047	41.343	0.651	0.763	34.967	5.3	35.574
101210-12	4.472	2.607	40.253	0.775	0.907	34.544	5.2	33.588
110412-01	4.506	1.010	26.268	0.295	0.353	34.091	-17.4	30.143
110412-02	4.492	1.504	25.933	0.454	0.539	34.089	-10.3	29.368
110412-03	4.459	2.039	25.848	0.590	0.684	34.294	-7.0	28.113
110412-04	4.435	2.610	25.582	0.746	0.851	34.366	-6.5	25.946
110412-05	3.002	1.028	27.417	0.510	0.613	32.196	1.8	25.729
110412-06	2.988	1.516	27.309	0.761	0.896	31.341	0.3	25.053
110412-07	2.981	1.985	27.029	0.943	1.086	31.516	1.0	24.216
110412-08	2.952	2.561	26.471	1.104	1.247	30.839	1.6	23.060
110412-09	1.491	1.061	32.449	1.050	1.206	29.888	1.0	23.612
110412-10	1.478	1.508	32.163	1.373	1.568	28.881	-1.1	22.323
110412-11	1.486	2.065	31.646	1.612	1.840	28.516	-0.9	21.466
110412-12	1.482	2.592	30.768	1.805	2.054	28.450	0.7	20.593
110413-01	4.435	2.645	33.333	0.801	0.932	34.503	2.8	32.213
110413-02	4.437	2.047	33.650	0.651	0.764	34.791	3.1	32.674
110413-03	4.485	1.500	33.860	0.505	0.612	35.415	2.9	33.456

Test #	G_{wi} kg/m ² s	G_a kg/m ² s	T_{wi} °C	Me_{NTU}/L_{fi} m ⁻¹	Me_R/L_{fi} m ⁻¹	K_{fdm}/L_{fi} m ⁻¹	EB %	$T_{ao,avg,R}$ °C
110413-04	4.506	1.082	33.955	0.376	0.468	37.146	3.4	33.815
110413-05	3.003	2.669	34.338	1.125	1.308	31.132	4.4	28.749
110413-06	2.998	2.109	34.874	0.971	1.126	31.372	2.2	29.728
110413-07	2.979	1.485	35.373	0.738	0.865	31.758	3.2	30.794
110413-08	2.969	1.062	35.686	0.530	0.635	32.900	5.8	31.324
110413-09	1.508	2.553	36.091	1.541	1.734	28.360	4.6	24.415
110413-10	1.514	2.061	36.712	1.432	1.637	28.597	0.7	25.556
110413-11	1.505	1.514	37.323	1.151	1.325	29.154	0.8	26.127
110413-12	1.493	1.081	38.290	0.917	1.047	29.495	1.6	27.342
110414-01	1.413	1.178	32.804	1.123	1.296	29.066	1.9	27.430
110414-02	1.415	2.338	32.058	1.776	1.999	*	1.1	23.896
110414-03	1.415	2.336	32.058	1.773	2.001	27.968	1.2	23.900
110414-04	1.415	2.740	31.724	2.005	2.215	28.232	0.2	23.081
110414-05	2.828	1.183	30.967	0.667	0.800	31.472	0.5	28.468
110414-06	2.820	1.698	30.469	0.916	1.065	30.689	1.1	27.089
110414-07	2.816	2.336	30.094	1.178	1.355	30.605	1.1	25.762
110414-08	2.815	2.730	29.749	1.291	1.488	30.416	1.0	24.943
110414-09	4.214	1.174	29.400	0.432	0.529	33.884	1.4	27.774
110414-10	4.190	1.735	29.040	0.615	0.732	33.618	2.1	26.773
110414-11	4.180	2.313	28.769	0.793	0.924	33.572	1.5	25.920
110414-12	4.191	2.712	28.401	0.931	1.075	33.306	0.7	25.295
110414-13	4.471	1.271	27.932	0.457	0.562	34.160	0.8	26.560
110414-14	4.462	1.709	27.657	0.574	0.687	34.366	1.5	25.794
110414-15	4.457	2.347	27.389	0.768	0.900	34.347	1.5	24.992
110414-16	4.456	2.723	27.073	0.838	0.967	34.006	1.7	24.351

Table B.6: Dry test results for trickle fill in crossflow (counterflow config.)

Test #	T_{ai} °C	T_{wbi} °C	m_{avo} kg/s	T_{wbo} °C	Δp_{fi} Pa	p_a Pa	G_a kg/m ² s	K_{fdm}/L_{fi} m ⁻¹
110408-01	27.911	17.767	3.987	16.707	18.5	100860	0.985	24.530
110408-02	28.738	18.132	5.037	17.449	30.5	100860	1.244	25.288
110408-03	28.436	18.170	5.972	18.015	42.5	100860	1.474	25.071
110408-04	28.179	18.034	6.899	17.870	56.5	100860	1.703	24.989
110408-05	29.679	18.459	8.250	18.082	81.0	100860	2.036	24.980
110408-06	29.117	18.497	9.470	18.352	106.5	100860	2.336	24.935
110408-07	29.949	18.766	10.898	18.613	142.0	100860	2.688	25.059
110408-08	30.026	18.761	11.190	18.600	150.0	100860	2.760	25.104

B.5. Rain zone tests**Table B.7: Test results for crossflow rain zone, Part 1**

Test #	T_{ai} °C	T_{wbi} °C	T_{wi} °C	T_{wo} °C	m_{avo} kg/s	m_{wi} kg/s	Δp_{fi} Pa	T_{wbo} °C	p_a Pa
100720-01	14.228	13.119	48.462	43.335	5.112	4.369	*	19.698	101160
100720-02	14.187	13.076	48.118	42.748	6.935	4.332	*	18.250	101160
100720-03	14.150	13.100	47.281	41.941	8.855	4.281	*	17.031	101160
100720-04	14.124	13.062	47.525	41.784	11.301	4.322	*	16.512	101160
100720-05	14.329	13.243	46.975	42.590	4.913	8.614	*	23.747	101160
100720-06	14.115	13.206	46.137	41.441	7.151	8.584	*	21.379	101160
100720-07	13.968	13.138	45.657	40.690	9.705	8.517	*	19.631	101160
100720-08	14.007	13.272	45.138	40.130	11.296	8.438	*	18.954	101160
100720-09	13.991	13.264	44.874	41.569	4.959	13.208	*	25.258	101160
100720-10	13.974	13.286	44.474	40.843	6.975	13.154	*	23.084	101160
100720-11	13.948	13.311	44.156	40.361	9.156	13.136	*	21.305	101160
100720-12	13.840	13.261	43.821	39.913	11.170	13.091	*	20.181	101160
100803-01	11.410	9.846	54.472	48.925	5.045	12.848	*	28.187	100880
100803-02	11.533	9.865	53.786	48.075	6.929	12.747	*	25.173	100880
100803-03	11.151	9.670	53.219	47.272	8.828	12.827	*	22.798	100880
100803-04	11.141	9.697	52.756	46.712	11.104	12.844	*	21.223	100880
100803-05	10.779	9.437	52.064	46.174	5.123	8.709	*	24.222	100880
100803-06	11.237	9.534	51.548	45.322	6.890	8.486	*	21.701	100880
100803-07	11.217	9.530	51.019	44.464	9.502	8.286	*	19.099	100880
100803-08	10.858	9.400	50.397	43.698	11.251	8.073	*	17.723	100880
100803-09	11.314	9.539	49.783	43.859	4.949	4.804	*	19.226	100880
100803-10	10.399	9.072	49.474	43.319	7.074	4.744	*	16.354	100880
100803-11	10.571	9.087	49.127	42.781	9.366	4.636	*	14.739	100880
100803-12	11.189	9.379	48.574	42.189	11.353	4.612	*	13.905	100880
100804-01	11.152	9.233	47.827	42.799	11.262	13.187	*	18.986	100880
100804-02	11.663	9.584	47.684	42.895	9.181	12.825	*	19.665	100880
100804-03	11.138	9.414	47.601	43.154	6.713	12.921	*	22.115	100880
100804-04	10.888	9.280	47.488	43.429	4.847	12.771	*	24.513	100880
100804-05	11.201	9.229	47.038	41.313	11.299	8.916	*	16.965	100880
100804-06	11.239	9.247	46.786	41.287	9.634	8.818	*	17.493	100880
100804-07	11.560	9.339	46.654	41.566	6.832	8.720	*	19.439	100880
100804-08	11.561	9.484	46.325	41.661	5.071	8.587	*	21.438	100880
100804-09	11.672	9.532	45.578	40.060	11.469	4.424	*	13.583	100880
100804-10	11.996	9.579	44.962	39.752	9.317	4.377	*	13.795	100880
100804-11	12.393	9.724	44.604	39.822	6.858	4.390	*	14.722	100880
100804-12	11.895	9.592	44.390	39.907	4.695	4.379	*	16.345	100880
100920-01	11.698	9.542	48.479	42.959	4.961	4.487	5.0	17.368	100510
100920-02	10.952	9.334	47.113	41.601	7.176	4.351	5.0	14.875	100510
100920-03	10.895	9.250	46.667	40.952	9.279	4.363	20.0	13.801	100510

Test #	T_{ai} °C	T_{wbi} °C	T_{wi} °C	T_{wo} °C	m_{avo} kg/s	m_{wi} kg/s	Δp_{fi} Pa	T_{wbo} °C	p_a Pa
100920-04	11.145	9.356	45.989	40.007	11.955	4.522	25.0	13.169	100510
100920-05	11.066	9.396	45.269	40.925	5.061	8.600	10.0	20.866	100510
100920-06	11.340	9.506	44.878	40.303	7.057	8.399	10.0	18.437	100510
100920-07	11.273	9.420	44.455	39.604	9.238	8.122	12.0	16.545	100510
100920-08	10.969	9.282	43.817	38.634	11.799	7.804	38.0	15.055	100510
100920-09	10.751	9.192	43.153	39.810	4.993	12.913	10.0	22.470	100510
100920-10	10.561	9.132	42.911	39.280	7.068	12.952	12.0	19.951	100510
100920-11	10.745	9.195	42.402	38.620	9.417	13.036	38.0	17.922	100510
100920-12	10.218	8.852	41.857	37.927	11.793	12.982	50.0	16.379	100510
100920-13	10.819	9.194	41.239	38.286	5.123	14.945	20.0	21.452	100510
100920-14	10.542	8.972	40.211	37.142	7.111	14.744	30.0	19.028	101160
100920-15	9.835	8.629	40.081	36.744	9.518	14.833	40.0	17.094	101160
100920-16	9.817	8.590	39.911	36.489	11.788	14.872	44.0	16.105	101160

Table B.8: Test results for crossflow rain zone, Part 2

Test #	G_{wi} kg/m ² s	G_a kg/m ² s	T_{wi} °C	Me_{eNTU}/L_{fi} m ⁻¹	Me_R/L_{fi} m ⁻¹	K_{fdm}/L_{fi} m ⁻¹	EB %	$T_{ao,avg,R}$ °C
100720-01	1.409	1.260	48.462	0.061	0.065	*	0.2	19.790
100720-02	1.397	1.711	48.118	0.065	0.069	*	0.1	18.330
100720-03	1.381	2.187	47.281	0.067	0.072	*	-3.2	17.223
100720-04	1.394	2.792	47.525	0.072	0.077	*	-1.3	16.612
100720-05	2.779	1.206	46.975	0.060	0.063	*	-0.7	20.356
100720-06	2.769	1.759	46.137	0.066	0.070	*	0.5	21.467
100720-07	2.747	2.392	45.657	0.071	0.075	*	-0.2	19.746
100720-08	2.722	2.785	45.138	0.073	0.078	*	0.7	19.008
100720-09	4.261	1.215	44.874	0.052	0.054	*	2.2	25.196
100720-10	4.243	1.713	44.474	0.057	0.059	*	2.8	22.990
100720-11	4.237	2.253	44.156	0.060	0.062	*	1.9	21.286
100720-12	4.223	2.751	43.821	0.062	0.065	*	2.5	20.128
100803-01	4.145	1.231	49.783	0.050	0.053	*	-2.7	28.817
100803-02	4.112	1.697	49.474	0.052	0.055	*	2.2	25.140
100803-03	4.138	2.169	49.127	0.055	0.058	*	1.3	22.871
100803-04	4.143	2.732	48.574	0.056	0.060	*	6.3	20.824
100803-05	2.809	1.256	52.064	0.059	0.063	*	1.1	24.309
100803-06	2.737	1.695	51.548	0.063	0.067	*	3.3	21.559
100803-07	2.673	2.343	51.019	0.068	0.072	*	3.6	18.961
100803-08	2.604	2.777	50.397	0.071	0.076	*	4.2	17.557
100803-09	1.550	1.220	54.472	0.065	0.069	*	4.5	19.008
100803-10	1.530	1.748	53.786	0.067	0.072	*	3.0	16.284
100803-11	1.495	2.317	53.219	0.070	0.075	*	1.9	14.732
100803-12	1.488	2.810	52.756	0.073	0.078	*	-2.2	14.070
100804-01	4.254	2.777	44.390	0.060	0.064	*	2.0	18.967

Test #	G_{wi} kg/m ² s	G_a kg/m ² s	T_{wi} °C	Me_{eNTU}/L_{fi} m ⁻¹	Me_R/L_{fi} m ⁻¹	K_{fdm}/L_{fi} m ⁻¹	EB %	$T_{ao,avg,R}$ °C
100804-02	4.137	2.262	44.604	0.059	0.062	*	-5.1	20.291
100804-03	4.168	1.650	44.962	0.056	0.058	*	-2.2	22.541
100804-04	4.120	1.188	45.578	0.053	0.055	*	-1.7	24.927
100804-05	2.876	2.791	46.325	0.072	0.077	*	1.5	16.975
100804-06	2.845	2.378	46.654	0.070	0.075	*	-1.7	17.746
100804-07	2.813	1.684	46.786	0.067	0.070	*	-2.9	19.848
100804-08	2.770	1.247	47.038	0.064	0.066	*	-1.5	21.755
100804-09	1.427	2.839	47.488	0.073	0.078	*	5.9	13.407
100804-10	1.412	2.306	47.601	0.071	0.076	*	-3.3	13.983
100804-11	1.416	1.697	47.684	0.067	0.071	*	-6.3	15.106
100804-12	1.413	1.160	47.827	0.064	0.068	*	-4.5	16.735
100920-01	1.447	1.225	48.479	0.064	0.068	5.210	-5.5	17.907
100920-02	1.404	1.775	47.113	0.067	0.072	2.491	-4.8	15.234
100920-03	1.407	2.297	46.667	0.071	0.076	6.020	-4.8	14.097
100920-04	1.459	2.960	45.989	0.078	0.083	4.534	-6.2	13.471
100920-05	2.774	1.246	45.269	0.062	0.065	10.005	0.2	17.367
100920-06	2.709	1.741	44.878	0.065	0.068	5.142	1.0	18.493
100920-07	2.620	2.282	44.455	0.070	0.074	3.605	-0.9	16.709
100920-08	2.517	2.918	43.817	0.077	0.081	7.058	-2.8	15.303
100920-09	4.165	1.227	43.153	0.054	0.056	10.261	2.0	22.437
100920-10	4.178	1.741	42.911	0.059	0.060	6.147	2.6	19.870
100920-11	4.205	2.324	42.402	0.061	0.064	11.050	1.3	17.949
100920-12	4.188	2.914	41.857	0.065	0.067	9.298	2.2	16.348
100920-13	4.821	1.260	41.239	0.054	0.056	19.568	-6.9	22.366
100920-14	4.756	1.753	40.211	0.058	0.060	15.392	-2.3	19.375
100920-15	4.785	2.351	40.081	0.062	0.064	11.487	-3.4	17.494
100920-16	4.797	2.913	39.911	0.063	0.066	8.245	1.1	16.144

B.6. Trickle fill in crossflow, $L_{fi,x} = 1.5$ m (Figure B.2)

Table B.9: Test results for trickle fill in straight crossflow ($L_{fi,x} = 1.5$ m), Part 1

Test #	T_{ai} °C	T_{wbi} °C	T_{wi} °C	T_{wo} °C	m_{avo} kg/s	m_{wi} kg/s	Δp_{fi} Pa	T_{wbo} °C	p_a Pa
100920-01	13.013	10.933	45.169	21.270	11.349	4.531	57.0	24.307	101320
100920-02	13.285	11.046	44.345	21.741	9.881	4.494	43.0	25.062	101320
100920-03	13.286	11.047	43.655	23.507	6.933	4.500	21.5	27.571	101320
100920-04	12.775	10.897	43.112	25.770	4.932	4.515	11.5	30.107	101320
100920-05	12.576	10.861	42.072	25.653	11.116	8.895	70.0	28.188	101320
100920-06	12.661	10.880	41.455	26.402	9.396	8.722	49.0	28.656	101320
100920-07	12.609	10.899	40.274	27.646	7.255	8.787	27.5	30.076	101320
100920-08	12.594	10.808	39.474	29.392	5.054	8.786	14.0	31.985	101320
100920-09	12.007	10.453	37.713	26.202	11.110	12.825	82.0	28.234	101320

Test #	T_{ai} °C	T_{wbi} °C	T_{wi} °C	T_{wo} °C	m_{avo} kg/s	m_{wi} kg/s	Δp_{fi} Pa	T_{wbo} °C	p_a Pa
100920-10	12.343	10.579	37.128	26.937	9.639	12.814	64.0	28.380	101320
100920-11	12.469	10.680	36.305	28.131	7.041	12.757	31.0	29.541	101320
100920-12	12.370	10.600	35.626	29.047	5.270	12.674	17.0	30.392	101320
100920-13	12.914	10.810	34.813	25.181	11.218	13.862	87.0	26.825	101320
100920-14	12.844	10.806	34.323	26.054	9.337	13.864	63.5	27.029	101320
100920-15	12.816	10.671	33.918	27.051	7.053	13.870	33.0	27.947	101320
100920-16	12.903	10.693	33.579	28.429	4.829	13.867	15.5	29.330	101320

Table B.10: Test results for trickle fill in straight crossflow ($L_{fi,x} = 1.5$ m), Part 2

Test #	G_{wi} kg/m ² s	G_a kg/m ² s	T_{wi} °C	Me_{eNTU}/L_{fi} m ⁻¹	Me_R/L_{fi} m ⁻¹	K_{fdm}/L_{fi} m ⁻¹	EB %	$T_{ao,avg,R}$ °C
100920-01	1.462	2.783	43.112	0.930	1.014	11.149	1.3	24.259
100920-02	1.450	2.421	43.655	0.896	0.992	11.077	0.2	25.126
100920-03	1.452	1.693	44.345	0.796	0.902	11.204	-2.2	27.937
100920-04	1.456	1.200	45.169	0.669	0.764	11.815	-1.4	30.415
100920-05	2.869	2.712	39.474	0.600	0.673	14.230	2.8	27.946
100920-06	2.814	2.291	40.274	0.562	0.629	13.924	0.2	28.742
100920-07	2.835	1.765	41.455	0.499	0.553	13.081	1.7	29.964
100920-08	2.834	1.226	42.072	0.418	0.466	13.700	1.9	31.846
100920-09	4.137	2.711	35.626	0.514	0.563	16.725	3.6	27.899
100920-10	4.134	2.351	36.305	0.464	0.502	17.333	2.2	28.226
100920-11	4.115	1.715	37.128	0.386	0.429	15.699	1.6	29.460
100920-12	4.088	1.282	37.713	0.323	0.368	15.352	1.5	27.219
100920-13	4.472	2.743	33.579	0.525	0.568	17.412	1.8	26.731
100920-14	4.472	2.282	33.918	0.444	0.486	18.347	0.3	27.119
100920-15	4.474	1.722	34.323	0.378	0.424	16.682	-1.2	28.245
100920-16	4.473	1.176	34.813	0.291	0.336	16.690	0.1	29.468

Table B.11: Dry test results for trickle fill in straight crossflow ($L_{fi,x} = 1.5$ m)

Test #	T_{ai} °C	T_{wbi} °C	m_{avo} kg/s	T_{wbo} °C	Δp_{fi} Pa	p_a Pa	G_a kg/m ² s	K_{fdm}/L_{fi} m ⁻¹
101110-01	15.415	13.776	3.825	13.547	5.5	100720	0.947	9.543
101110-02	15.470	13.961	4.545	13.776	7.5	100720	1.125	9.211
101110-03	15.368	13.903	5.470	13.733	11.0	100720	1.354	9.329
101110-04	15.406	13.972	6.783	13.838	16.0	100720	1.679	8.823
101110-05	15.320	14.004	7.922	13.896	22.0	100720	1.961	8.893
101110-06	15.101	13.811	8.980	13.646	28.0	100720	2.223	8.815
101110-07	15.189	13.766	10.993	13.588	41.5	100720	2.722	8.718
101110-08	15.237	13.773	11.527	13.604	45.5	100720	2.854	8.692

APPENDIX C: Detailed information about thermocouples in the crossflow test facility

In this appendix, the name, installed location, channel number and correction factor is reported for each of the 53 thermocouples. This information is intended for future users of the crossflow test facility.

For additional information about thermocouple locations, refer to Section 3.1.1.

C.1. Thermocouple locations

C.1.1. Aspirated psychrometers at air inlet

The thermocouples that measure drybulb air temperature at the air inlet are named $T_{ai,1}$, $T_{ai,2}$, $T_{ai,3}$ and $T_{ai,4}$ and they are physically located inside the aspirated psychrometers at respectively (1), (2), (3) and (4) in Figure C.1.

The thermocouples that measure wetbulb air temperature at the air inlet are named $T_{wbi,1}$, $T_{wbi,2}$, $T_{wbi,3}$ and $T_{wbi,4}$ and they are physically located inside the aspirated psychrometers at respectively (1), (2), (3) and (4) in Figure C.1.

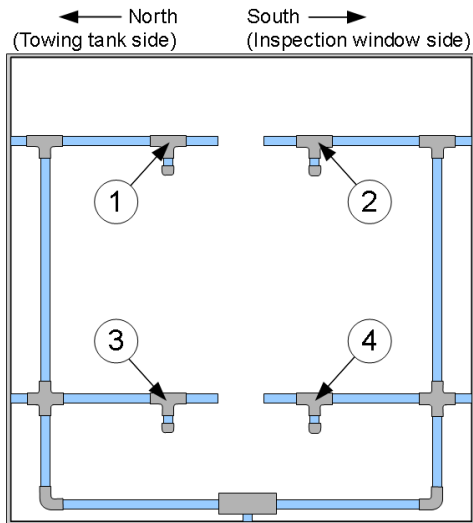


Figure C.1: Location of thermocouples inside aspirated thermocouples at the air inlet

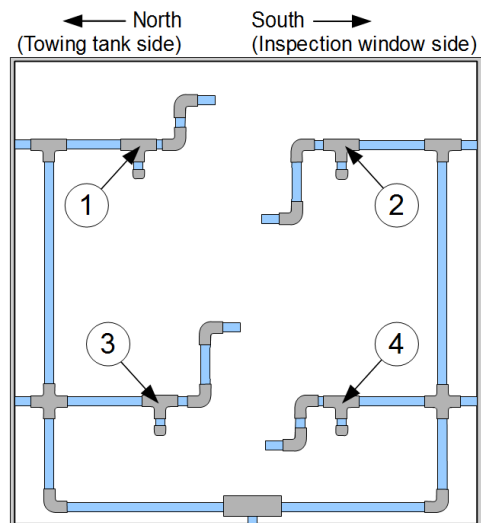


Figure C.2: Location of the thermocouples inside the aspirated psychrometers downwind of the air mixing vanes

C.1.2. Aspirated psychrometers downwind of the air mixing vanes

The thermocouples that measure drybulb air temperature downwind of the air mixing vanes are named $T_{ao,1}$, $T_{ao,2}$, and $T_{ao,3}$ and they are physically located inside the aspirated psychrometers at respectively (1), (2) and (4) in Figure C.2.

The thermocouples that measure wetbulb air temperature downwind of the air mixing vanes are named $T_{wbo,1}$, $T_{wbo,2}$, $T_{wbo,3}$ and $T_{wbo,4}$ and they are physically located at respectively (1), (2), (3) and (4) in Figure C.2.

C.1.3. Rake of aspirated psychrometers immediately downwind of test section

The thermocouples that measure the drybulb air temperature profile downwind of the drift eliminators are named, from top to bottom, $T_{\text{dbo}, r1}$, $T_{\text{dbo}, r2}$, $T_{\text{dbo}, r3}$ and so on up until $T_{\text{dbo}, r8}$.

The thermocouples that measure the wetbulb air temperature profile downwind of the drift eliminators are named, from top to bottom, $T_{\text{wbo}, r1}$, $T_{\text{wbo}, r2}$, $T_{\text{wbo}, r3}$ and so on up until $T_{\text{wbo}, r8}$.

These thermocouples are installed inside the aspirated psychrometer rake that is shown in Figure 3.5. The heights from the tunnel floor at which the 8 aspirated psychrometers are located are respectively 1.942, 1.840, 1.713, 1.518, 1.331, 1.181, 0.946 and 0.393 meters.

C.1.4. Various thermocouples that measure water temperature at the outlet

The rake that measures water temperature immediately below the fill consists of 13 sensors that are named $T_{\text{wo}, r1}$, $T_{\text{wo}, r2}$, $T_{\text{wo}, r3}$ and so on up to $T_{\text{wo}, r13}$. These are arranged in the direction of airflow just below the fill zone, with $T_{\text{wo}, r1}$ being on the most upwind side and $T_{\text{wo}, r13}$ on the most downwind side, as is shown in Figure C.3.

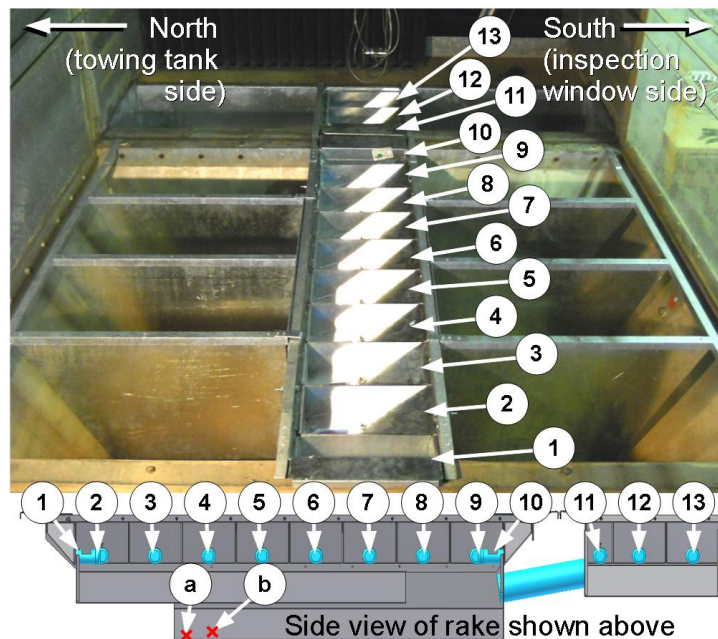


Figure C.3: Locations of thermocouples within the rake at the water outlet

Figure C.3 also shows the location of the two thermocouples located in the mixing duct under the outlet water rake. The one that is labeled (a) on the figure is slightly lower and closer to the outlet and is named $T_{\text{wo}, \text{md}, a}$. The other one, labeled (b) on the figure, is unsurprisingly named $T_{\text{wo}, \text{md}, b}$.

C.1.5. Other sensors

The locations of the rest of the sensors are shown in sufficient detail in Section 3.1.1. The names of the remaining sensors are:

- The water temperature is measured in the water supply pipe immediately upstream of the filter by three thermocouples named $T_{wi,1}$, $T_{wi,2}$ and $T_{wi,3}$.
- The water temperature inside of the water catchment basin is measured by two thermocouples named $T_{wo,b1}$ and $T_{wo,b2}$ ('b' denotes 'basin').
- The water temperature in the pipe that drains the water catchment basin is measured by two thermocouples named $T_{wo,d1}$ and $T_{wo,d2}$ ('d' denotes drain).

C.2. Thermocouple channel numbers and correction factors

The thermocouple measurements from the data logger are corrected using the following formula.

$$T_{\text{true}} = T_{\text{meas}} + c_1 (T_{\text{meas}} - 24.995 \text{ } ^\circ\text{C}) + c_2 \quad (\text{C1})$$

The way that the correction factors, c_1 and c_2 were determined is explained in Section 3.6.2. The equation is not the same as Eq. (3.1), but equivalent. Eq. (C1) takes the form that it does because the measurement that was taken at 24.995 °C, which was room temperature was the most stable and therefore the most reliable of the temperatures. It is therefore used as a reference temperature.

The channel number and correction factors, are given in Table C.1 and Table C.2.

Table C.1: Thermocouple channel numbers and correction factors, Part 1

Name	Channel number	c_1	c_2	Name	Channel number	c_1	c_2
$T_{ai,1}$	101	-0.00719	0.417	$T_{wi,1}$	204	0	0.080
$T_{ai,2}$	102	-0.00714	0.389	$T_{wi,2}$	205	0	-0.067
$T_{ai,3}$	103	-0.00788	0.411	$T_{wi,3}$	206	0	-0.241
$T_{ai,4}$	104	-0.00729	0.285	$T_{wo,d1}$	211	-0.168	0.012
$T_{wbi,1}$	105	-0.00759	0.316	$T_{wo,d2}$	212	-0.308	0.005
$T_{wbi,2}$	106	-0.00782	0.247	$T_{wo,md,a}$	209	0	-0.202
$T_{wbi,3}$	107	-0.00764	0.216	$T_{wo,md,b}$	210	0	-0.149
$T_{wbi,4}$	108	-0.00756	0.283	$T_{wo,b1}$	207	0	-0.180
$T_{ao,1}$	314	0	-0.217	$T_{wo,b2}$	312	0.008544	-0.586
$T_{ao,2}$	315	0	-0.144				
$T_{ao,3}$	316	0	-0.125				
$T_{wbo,1}$	317	0	-0.199				
$T_{wbo,2}$	318	0	-0.012				
$T_{wbo,3}$	320	0	0.047				
$T_{wbo,4}$	319	0	0.069				

Table C.2: Thermocouple channel numbers and correction factors, Part 2

Name	Channel number	c_1	c_2	Name	Channel number	c_1	c_2
$T_{\text{dbo, r1}}$	301	0	0.392	$T_{\text{wo, r1}}$	208	0	-0.198
$T_{\text{dbo, r2}}$	304	0	-0.051	$T_{\text{wo, r3}}$	214	0	-0.054
$T_{\text{dbo, r3}}$	109	0	0.273	$T_{\text{wo, r4}}$	213	0.009036	-0.423
$T_{\text{dbo, 4}}$	111	0	0.363	$T_{\text{wo, r5}}$	311	0	-0.132
$T_{\text{dbo, r5}}$	201	-0.00361	0.457	$T_{\text{wo, r6}}$	310	-0.00812	-0.346
$T_{\text{dbo, r6}}$	305	0	-0.288	$T_{\text{wo, r7}}$	309	0	-0.442
$T_{\text{dbo, 7}}$	110	0	0.302	$T_{\text{wo, r8}}$	313	0	-0.423
$T_{\text{dbo, r8}}$	112	0	0.384	$T_{\text{wo, r9}}$	307	0	-0.422
$T_{\text{wbo, r1}}$	202	0	0.212	$T_{\text{wo, r10}}$	306	0	-0.475
$T_{\text{wbo, r2}}$	303	0	0.123	$T_{\text{wo, r11}}$	215	0	-0.453
$T_{\text{wbo, r3}}$	113	0	0.510	$T_{\text{wo, r12}}$	216	0	0.016
$T_{\text{wbo, r4}}$	115	0	0.416	$T_{\text{wo, r13}}$	217	0	0.145
$T_{\text{wbo, r5}}$	302	0	0.218				
$T_{\text{wbo, r6}}$	203	0	0.223				
$T_{\text{wbo, r7}}$	114	-0.00897	0.391				
$T_{\text{wbo, 8}}$	116	0	0.588				

APPENDIX D: Report on improvements made to the crossflow test facility

During the critical evaluation of the crossflow test facility, multiple opportunities for improvement were identified and consequently addressed. Note that the description of the facility that is given in Sections 3.1 and 3.2, is of the facility the after improvements had been made.

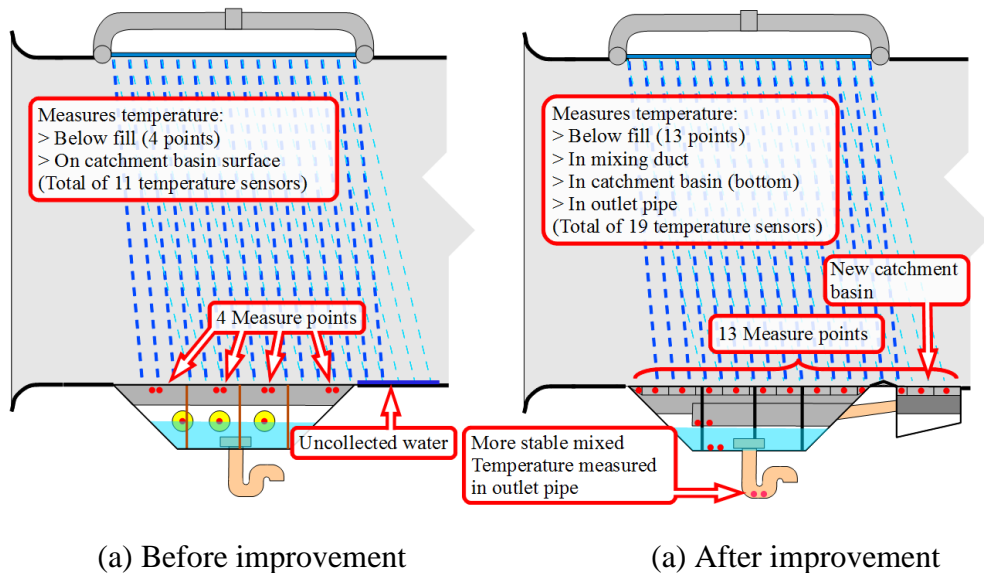
The purpose of this appendix is to describe to the examiner of this project the extent of the work that went into improving the crossflow test facility during the course of this project. To this end, the work is not described in detail, but instead the end results are briefly described and illustrated with the intention to give a reader that has some knowledge of experimental and/or technical work a fair impression of what the work entailed.

D.1. Improved equipment to measure the temperature of the water at the outlet

New equipment was designed, manufactured and installed to measure the temperature of the water, replacing the old equipment. This equipment is briefly described in Section 3.2.3.

Additionally, the warped wooden sheets that prevent air to flow through the water catchment basin were replaced by galvanized plate sheets and an extra water catchment basin was designed, manufactured and installed. The difference between the old and new equipment is shown in Figures D.1 and D.2.

A design view of the rake, mixing duct and extra catchment basin in Inventor© is shown in Figure D.3.



(a) Before improvement (a) After improvement
Figure D.1: The difference between the previous and the improved equipment to measure the temperature at the water outlet

A section of the tunnel floor immediately downstream of the fill zone was cut away and an additional water catchment basin was designed, manufactured and installed in order to collect and drain water that is dragged along by the air.

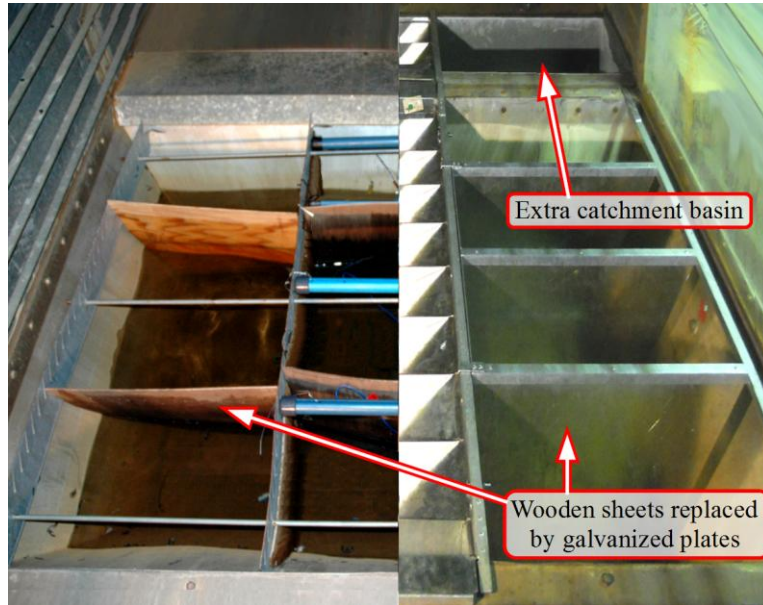


Figure D.2: Comparison between the previous and the improved equipment to measure the temperature at the water outlet

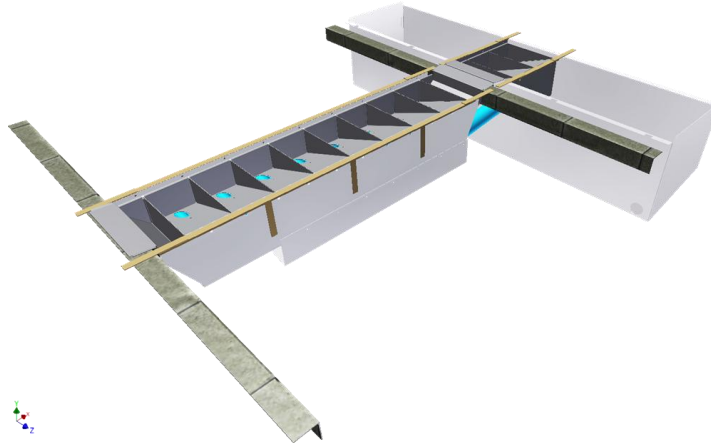
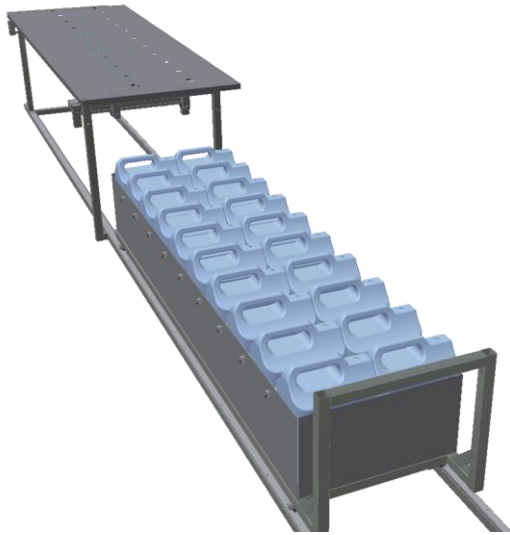


Figure D.3: Design view of equipment to measure the temperature of the water at the outlet in Inventor©

D.2. Work done to improve the uniformity of water distribution

The equipment that was designed and manufactured to measure the uniformity of the water distribution in the crossflow test section is shown in Figure D.4.

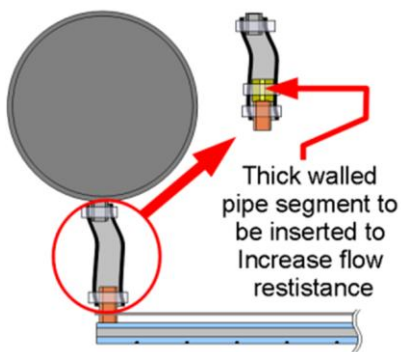
In order to improve the uniformity of the water distribution, pipe segments were designed, manufactured and inserted into the spray frame, as is shown in Figure D.5. This was a laborious task because 264 very tightly fitted hose clamps had to be removed and 396 had to be clamped back on.



(a) Design view in Inventor©

(b) Photo during use

Figure D.4: Equipment that was designed and manufactured to measure the uniformity of the water distribution in the crossflow test facility



(a) Concept

(b) Photo of insertion procedure

Figure D.5: Modifications done to the spray fram

D.3. Installation of 4 additional psychrometers into rake at air outlet

In order to improve the resolution with which the temperature profile at the air outlet can be measured, 4 new aspirated psychrometers were installed in addition

to the four that were already installed. Both the previous and the improved rake of aspirated psychrometers are shown in Figure D.6.

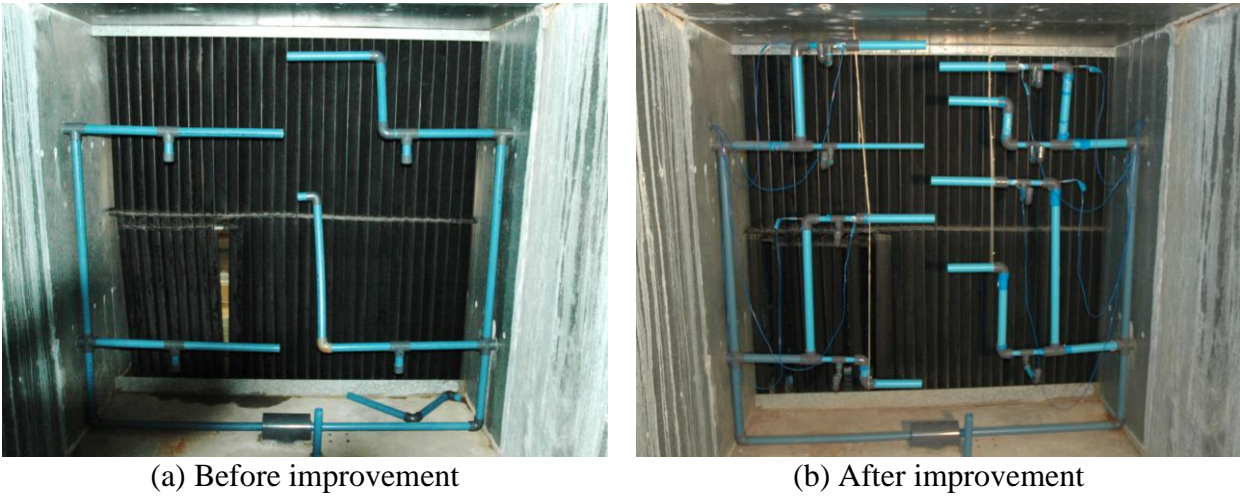


Figure D.6: The aspirated psychrometers downwind of the drift eliminators before and after improvement

D.4. Installation of 8 additional thermocouples downwind of mixing vanes

In order to measure the temperature of the mixed air downwind of the air outlet, four aspirated psychrometers were installed downwind of the air mixing vanes (see Figure 3.2). There used to be 4 aspirated downwind of the mixing vanes, but their thermocouples had been removed.

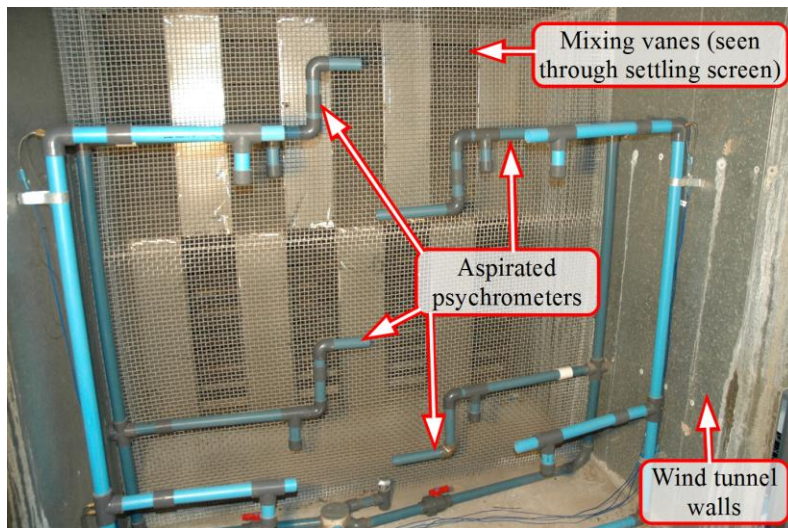


Figure D.7: Aspirated psychrometers that were installed to measure the temperature of the mixed air downwind of the mixing vanes

All that was therefore necessary was to acquire 8 thermocouples and install them in the pipes that were already there. A blower fan was also already installed to drag air through the pipes. The 4 aspirated psychrometers are shown in Figure D.7

D.5. Installation of a higher capacity drain pump

In order to be able to do tests at higher water mass velocities in the crossflow test section, a higher capacity pump was installed. An investigation was done to determine the required specifications for the pump and an appropriate pump was acquired. The pump was installed, but the installation was made very difficult because of the extremely constrained and inaccessible space under the wind tunnel into which the pump had to be fitted.

D.6. Other work and improvements

- Bleed valves were installed on the top of the water distribution spray frame manifolds in order to bleed out any trapped air.
- The LabView program was expanded to show measurements from the 31 thermocouples that were installed during the course of the project. The following other improvements were made to the LabView program: a functionality to increase the frequency with which certain sensors are scanned was added, various graphical displays were added, the functionality to add test date and time to the output file was added and both the program code and the output file was tidied up.
- A strainer for the pipe that drains the water catchment basins was manufactured and installed in order to prevent solids from entering the pipe and damaging the pump.
- The pressure probes that are visible on Figure 3.3 were mounted in the center of the tunnel both upwind and downwind of the fill zone.
- 40 angle irons that were permanently mounted on the insides of the tunnel walls in the fill zone were removed in order to eliminate air gaps between the fill and the tunnel walls during trickle fill tests.
- The water catchment basins were insulated using packaging foam in order to reduce the unmeasured heat loss from the basins.
- During the water distribution tests, the blower fan of the aspirated psychrometers at the air inlet was damaged because water got into the motor. It was repaired and re-mounted in a different way to prevent the problem from re-occurring.

APPENDIX E: Content of DVD submitted with thesis

A data DVD is submitted with this thesis. In order to obtain the DVD or copies of its content, contact Prof. Hanno C.R. Reuter at

Department of Mechanical and Mechatronic Engineering,
Stellenbosch University,
Private Bag X1, Matieland 7602, South Africa.
Tel: +27 (0) 21 808 4376
Fax: +27 (0) 21 808 4958
Email: hreuter@sun.ac.za

The content of DVD is described in Sections E.1 and E.2.

E.1. Code and demos of how to use it

Everything that is required to run and use the programs that were written during this project is included on the DVD. Several thoroughly commented demo files are also included to help users who are unfamiliar with the code to use it.

These demo files will help the user

- to process experimental data from the crossflow test facility (`Demo_ProcessExpData.py`).
- to use the 2D fill simulation program that implements the Reuter model (`Demo_ReuterModel.py`).
- to use the single drop simulation program (`Demo_SingleDrop.py`).
- to generate graphs that compare experimental results and (automatically generated) model predictions (`Demo_ExpModComparison.py`).

All code is written in Python 2.7 and can be run on any (Windows) computer with Python 2.7, and its site packages NumPy 1.6, Matplotlib 1.0 and SciPy 0.9, PyWin32-216 installed (or newer versions).

The exception is the FORTRAN library that is used by the fill simulation program. No additional framework is required to call the FORTRAN library from Python, since that is handled by ctypes, which is a standard Python 2.7 extension. The source file (`ThermoFuncs.f95`) for the FORTRAN library is included on the DVD, and it can be edited with any text editor such as NotePad++ . Before the edited source file will be used by the Python program, the edited source file must be compiled to a .dll file (`libThermoFuncs.dll`), replacing the previous one. During this project C-make and MinGw32 was used for compiling the FORTRAN library.

All of the software mentioned above is freeware and the binaries (install files) for these programs are included on the data DVD. Install files for Eric4, a useful freeware IDE for Python, as well as for PyQt4 (a prerequisite GUI toolkit for Eric4) are also included. Instructions on how to install them are provided in text files in their directories. Instructions are also provided about how to edit and compile the FORTRAN library using CMake and MinGw32.

The code that was written for this project is commented so that a user with a basic understanding of programming will be able to make sense of the code.

Note that when experimental data from an entire crossflow test series is processed using Demo_ProcessData.py, it writes a file “CrossFlowTestResults_ALL.txt” to (default) “C:\Temp”, provided that C:\Temp exists or the program is allowed to create it. This data can be copied into an Excel template named “Crossflow results template.xls” that is included on the DVD in the “Template” folder. This template automatically displays the processed experimental results on fancy charts and tables. More instructions on where and how to copy-paste the data is provided on the “Help” tab in the “Crossflow results template.xls”.

E.2. Additional test data and graphical displays

All test results published in Appendix B are included.

Some test results that are not published in Appendix B are included: one rain zone test series, one trickle fill in straight crossflow $L = 1.5\text{m}$ test series, one or more extra dry test series for each of the trickle fill configurations.

All test results from Bertrand that were used are included.

For every single crossflow test done in this project, the following is also included:

- The raw data, still in the form that it came in from the crossflow test facility.
- The raw data, on a sheet with headings, averages and some macro’s that help to automate data processing.
- A DataArray file, which is the raw data in a format that can be imported by the Python code and automatically processed.
- A comparison between the measured temperature profiles at the air and water outlets and the Reuter model prediction for that case. Such a graph is shown in Figure E.1. These graphs are in the directory “Temperature profile comparisons”.

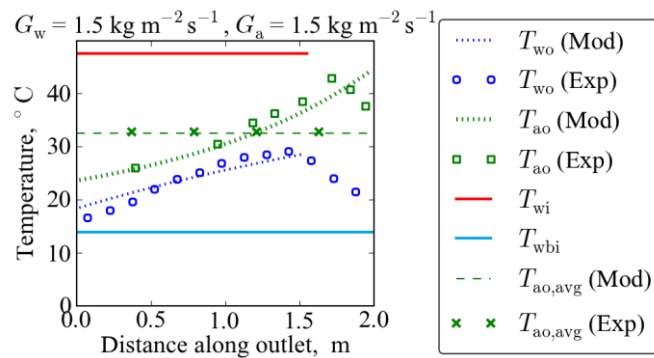


Figure E.1: Comparison of temperature profiles at the outlet predicted by the model and experimentally measured (included on DVD for every crossflow test)

- Complete graphical results, shown for one test in Figure E.2, from the Reuter model fill simulations are also provided for every crossflow test.

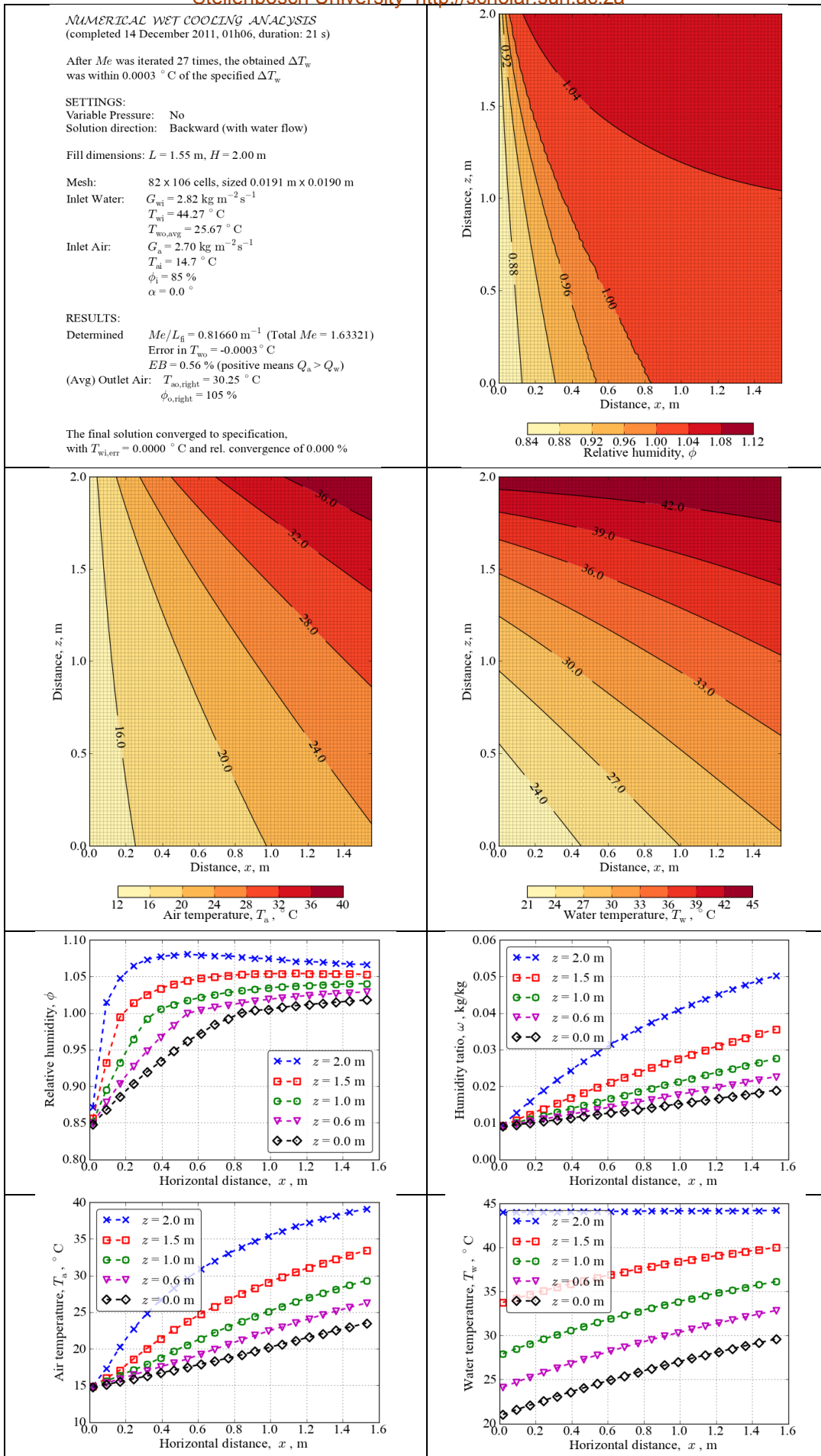


Figure E.2: Graphical results from fill simulation program that are included on the DVD for every crossflow test

For every test series, a Summary Excel file with several graphics, of which samples are shown in Figure E.3 and Figure E.4, is included.

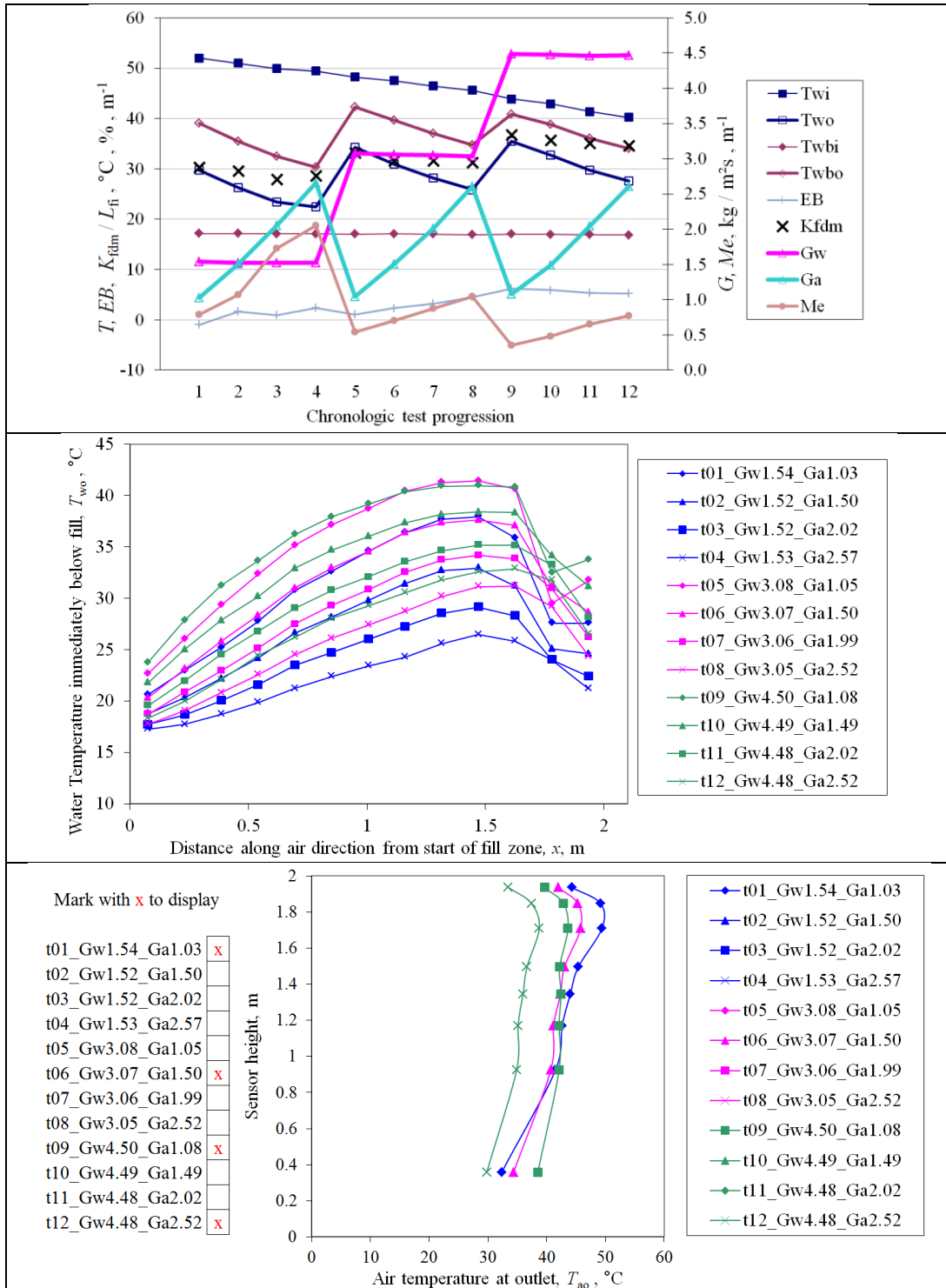


Figure E.3: Charts in Excel Summary file that are included on DVD for every series of crossflow tests, Part 1

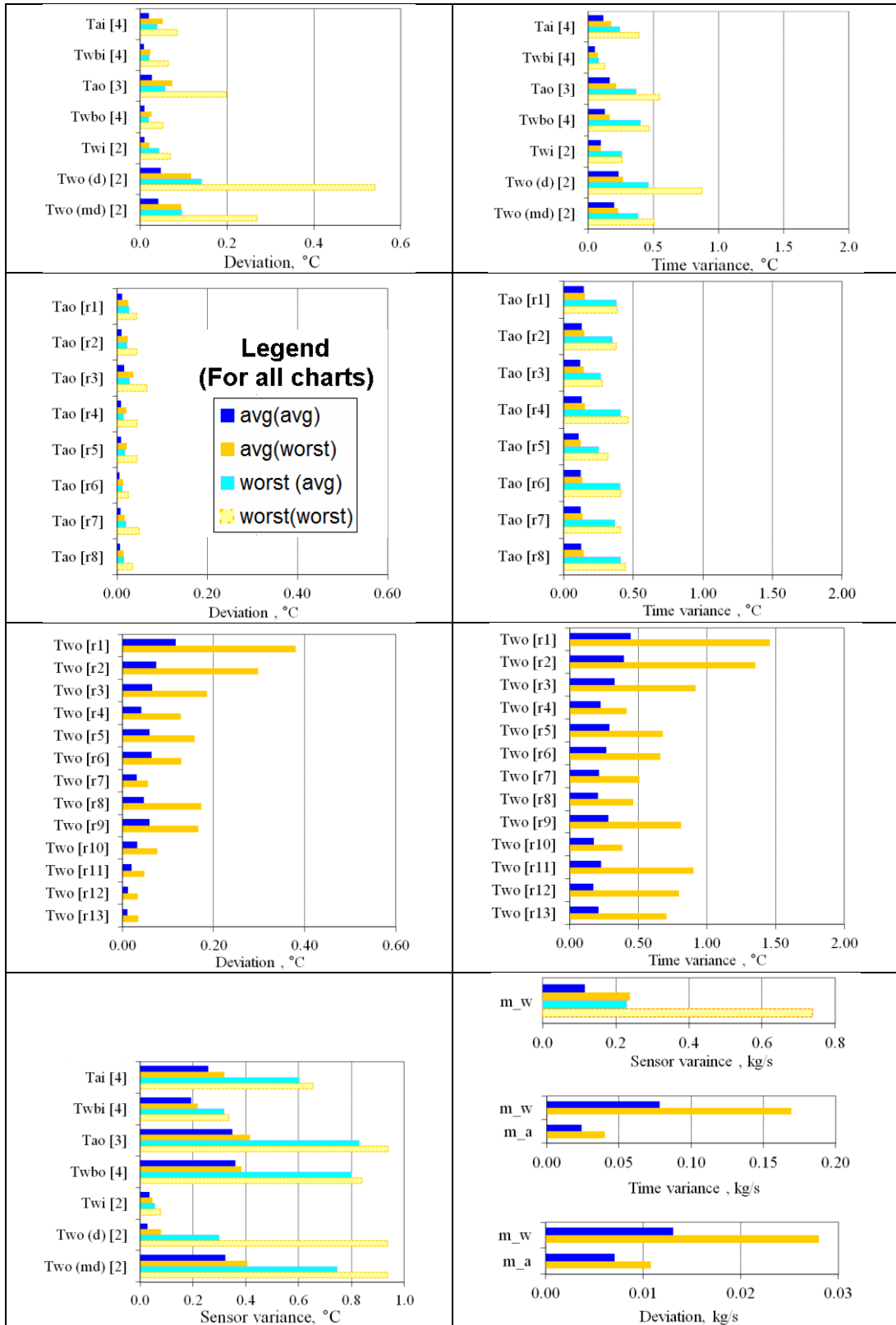


Figure E.4: Statistical charts in Excel Summary file that are included on DVD for every series of crossflow tests